NTNU – Trondheim
Norwegian University of
Science and Technology

Validating the algorithms AAA and Acuros for calculation of dose from flattening filter free beams in heterogenous tissue

Application to stereotactic radiotherapy of
lung tumors

Kristine Perander

MSc in Physics
Submission date: May 2015
Supervisor: Catharina de Lange Davies, IFY
Co-supervisor: Veronika Tømmerås, Universitetssykehuset Nord-Norge

Norwegian University of Science and Technology
Department of Physics

Abstract

In radiation therapy of cancer, modeling the dose to the patient is very important. Several computational algorithms are available, where some model dose in heterogeneous tissue better than others. After implementation of stereotactic radiotherapy of lung cancer at the University Hospital of North Norway, where high dose are given with high precision, it is desirable to look at the difference in the calculated dose for the established algorithm AAA, and newcomer Acuros, in heterogeneous tissue. Dose measurements were made using radiochromic film and ionization chambers in a lung phantom, and compared with calculated dose distributions for different energies which can be used in the treatment of lung tumors. In addition, patients previously treated stereotactically to the lung was replanned using Acuros and volume doses were compared. Results from the lung phantom show that Acuros calculates lower dose in light lung tissue compared to AAA but it is difficult to make measurements the dose in low density media for absolute comparisons. Patient plans calculated by Acuros show correspondingly a much lower dose to lung tissue surrounding a tumor and an overall lower dose given to heterogeneous tissue relative to AAA calculations. To acquire better estimations of actual doses given during radiotherapy of lung tumors, the implementation of Acuros should be considered.

Sammendrag

I strålebehandling av kreft er modellering av dose svært viktig for å gi en trygg behandling. Der finnes forskjellige typer beregningsalgoritmer hvor enkelte modellerer bedre enn andre i heterogent vev. Etter implementeringen av stereotaktisk strålebehandling av lungekreft ved UNN, der høy dose gis med høy presisjon er det ønskelig å se på forskjellen i beregnet dose for den etablerte algoritmen AAA, og nykommeren Acuros i heterogent vev. Målinger ble gjort med radiokrom film og ionisasjonskammer i lungefantom og sammenlignet med beregnede dosefordelinger for ulike energier som kan brukes i behandling av lungetumor. Pasienter som tidligere er behandlet for lungekreft med stereotaktisk stråleteknikk ble replanlagt med Acuros og volumdoser ble sammenlignet for de to algoritmene. Resultater fra lungefantomet viser at Acuros beregner lavere dose i lett lungevev i forhold til AAA men det er vanskelig å gjøre målinger av dose i lett vev for absolutte sammenligninger. Pasientplaner beregnet med Acuros viser tilsvarende en mye lavere dose gitt til lungevev rundt tumor og en generell lavere dose gitt til heterogent vev i forhold til AAA-beregninger. For å oppnå bedre beregninger av faktiske doser gitt ved strålebehandling av lunge bør implementering av Acuros vurderes.

Table of Contents

List of Tables

List of Figures

Glossary of terms

AAA	=	Anisotropic Analytical Algorithm
3D-CRT	=	3-dimensional conventional radiation therapy
HU	=	Hounsfield Unit
CT	=	Computed tomography
DVH	=	Dose volume histogram
FFF	=	Flattening filter free
GTV	=	Gross tumor volume
IAEA	=	Internation Atomic Energy Agency
ICRU	=	International Commission on Radiation Units and protection
IMRT	=	Intensity modulated radiation therapy
kV	=	Kilovolt = 1000 volt. Diagnostic x-ray energies
LBTE	=	Linear Boltzmann Transport Equation
MLC	=	Multi-leaf collimator
MRI	=	Magnetic resonance imaging
MU	=	Monitor Unit
MV	=	Mega volt = 10 000 volt. Radiotherapy energies
NSCLC	=	Non-small cell lung chancer
OAR	=	Organs at risk
PTV	=	Planning target volume
QA	=	Quality assurance
SBRT	=	Stereotactic body radiation therapy
SSD	=	Source-surface distance, or source-skin distance
SSDL	=	Secondary standards dosimetry laboratory
TIFF	=	Tagged image file format
TLD	=	Thermo luminescent diode
TPS	=	Treatment planning system
UNN	=	University hospital of North Norway
VMAT	=	Volumetric modulated arc therapy

Acknowledgement

This thesis work was carried out at the department of radiotherapy at the University Hospital of North Norway, Tromsø. I would like to send a big thank you to my advisor, medical physicist Veronika Tømmerås, for all of you guidance, help and support. I would also like to thank the other medical physicists at the department - Rune, Jorunn, Turid, Øyvind, Gosia and Brede for hosting me, teaching me, and irradiating phantoms with me long after working hours. I have learned a lot and I am excited to learn more. To the radiation therapists at the department - thank you for welcoming me, for help with the CT scanner, and for the glorious thing that is friday cake!

To my Trondheim advisor, Professor Catharina Davies - thank you for your guidance and feedback on the writing process.

Last but not least, I would like to thank my husband Stephen for all of your love and support as I left home for one year to pursue my dream.

May 2015
Kristine Perander

Chapter 1

Introduction

Second to heart and lung diseases, cancer is one of the leading causes of death world wide. In Norway, there were more than 30 000 new cancer cases and close to 11 000 cancer deaths reported in 2013 (1). Many cancer types have high survival rates after huge advancement in the treatment methods available in the past decades. Lung cancer is one of the three most common cancers in both genders but has one of the lowest survival rates. Median survival after diagnosis is less than one year and the 5 year local control rate is only 13 and 19% in males and females, respectively. The survival rate has not increased significantly in the past 60 years.

Tumors are treated by surgery, chemotherapy, radiation or some combination of these methods. If the cancer is thought to be curable, surgery is the first choice treatment method, sometimes with post-op radiation to lower the risk of relapse. If surgery is not possible due to risk of complications, or refusal by the patient, radiation therapy can be given as an alternative. For palliative treatments radiotherapy plays a larger role, and accounts for a large portion of treatment courses given by Norwegian radiotherapy departments. About 50 % of cancer patients receive radiation therapy at some point during their treatment.

X-ray beams have been used in the treatment of tumors since their discovery in 1895. Commercial equipment providing high energy radiation became available in the 1950s. Technology advances have provided continuous improvement of beam delivery and planning, particularly with the introduction of CT imaging in the 1970s. As oncologists and radiation therapists have more accurate information about tumor size and position, tougher treatments can be prescribed which have a higher chance for cure without increasing the risk of severe side effects.

Tolerance of healthy tissue surrounding the tumor is the limiting factor in how much radiation one can prescribe. To protect the surrounding tissue the normal course of action is to give the treatment in small fractions of 2 Gy daily for up to seven weeks allowing healthy tissue to repair between fractions. Unfortunately this does not provide acceptable tumor control for all cancers. Hypofractionation, larger doses in fewer fractions using the stereotactic technique has recently returned as a solution to tumors which are harder to treat using the traditional approach. Small inoperable lung tumors are of interest as they often have no successful curative treatment options using conventional radiation therapy.

Stereotactic body radiation therapy using flattening filter free, intensity modulated beams are of interest in the treatment of inoperable non-small cell lung cancers. The prescribed fraction dose is up to ten times larger than conventional treatment and studies show this method provides local control rates up to 90 % (2). The Norwegian Lung Cancer Group recommends stereotactic radiotherapy as the first choice treatment for inoperable stage 1 non-small cell lung cancer (2) and more hospitals in Norway are now implementing the technique. The University Hospital of North Norway (UNN) started treating lung cancers stereotactically i 2014.

In addition to knowledge about the tumor position relative to healthy organs, knowledge about where and how much radiation will be absorbed is needed. This is where accurate treatment planning comes in. The human body consists of different biological materials with varying densities. Some planning algorithms handle density variations better than others. The Acuros algorithm for the Eclipse treatment planning system promise a more accurate estimation of dose in heterogeneous tissue (11). The thorax is one such region as it consists of dense bone as well as air filled lung. The algorithm also requires less computing power for planning advanced techniques. It would therefore be advantageous to use the Acuros algorithm in the treatment planning of lung cancers using the stereotactic technique.

The treatment planning system at UNN has the Acuros algorithm available but it has not yet been implemented for routine use. Before this is done a validation of the properties of Acuros is needed for heterogeneous tissue. In this study, an investigation of the behavior of Acuros in low density media is conducted. Comparisons are made to the currently used Anisotropic Analytical Algorithm for different energies relevant to lung treatments including flattening filter free beams. The estimated dose from the two algorithms are then compared to measurements of absolute dose in a lung phantom using radiochromic film and ionization chambers. To test the performance of Acuros in clinical dose planning, 10 patients treated stereotactically to the lung is replanned using Acuros and the plans are compared to the original AAA calculation. In the light of published experimental findings it is expected to see Acuros performing better in low density tissue compared to AAA, and at the same time have the accuracy to pass quality assurance tests for clinical use.

Chapter 2

Background theory

2.1 The Linear Accelerator

The linear accelerator (referred to as linac from now on) is a device used to deliver radiation treatment to patients for energies in the megavolt (MV) range. The linac accelerates a beam of electrons, and can deliver them to the patient or convert them to photons (high energy x-rays) and deliver these instead. The choice of radiation type is based on the depth of the target in the body as electrons have a limited range compared to photons. The linac has the ability to rotate around the patient and deliver a beam from any angle. The point in space which the linac rotates around is called the isocenter and is located 100 cm from the target position in most linacs. The construction of the TrueBeam linear accelerator with emphasis on the delivery of photons will now be explained.

2.1.1 Construction

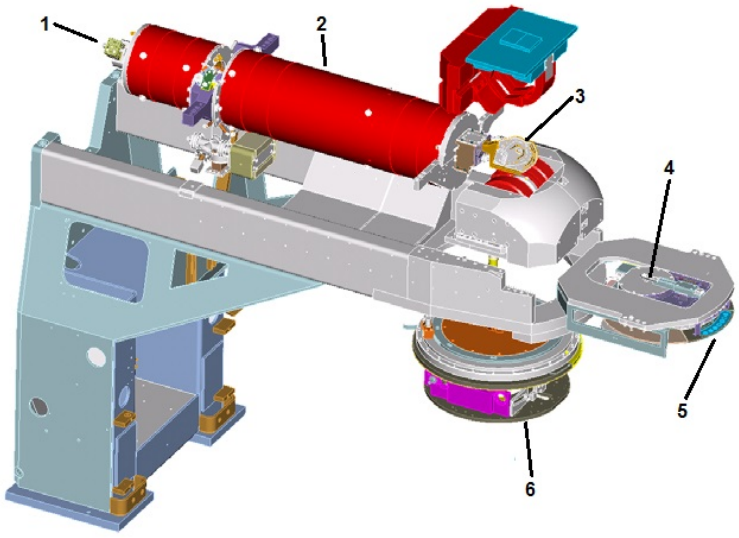

Figure 2.1: TrueBeam accelerator construction. 1: Electron gun. 2: Accelerator tube. 3: Bending magnet. 4: Target. 5: Carousel with filter selection. 6: MLC. The beam exits from below the purple colored MLC. The entire structure seen here rotate as the gantry rotates.

A schematic of the main linac components is shown in figure 2.1 with number 1 to 6 showing the location of some important components explained below. Electrons originate in pulses from what is called the electron gun (figure 2.1-1). As in the diagnostic x-ray tube, they are released from a cathode by thermoionic emission. A strong electric field force the electrons to enter the accelerating waveguide (figure 2.1-2); a sectioned copper tube containing vacuum cavities. The beam of electrons enter with a velocity of about 0.4c (where c is the speed of light) and are accelerated to 0.998c by the end. This is achieved by the help of a set of microwave frequency electromagnetic waves produced in the klystron, synchronized to fit the pulsed electrons and accelerate them when their phases match. Magnetic coils maintain the extent of the beam and as it exits the accelerating wave guide the cross section is no more than a few millimeters.

The radiation beam exits the waveguide parallel to the floor and its direction must be altered before entering the patient. This is done using a magnetic field (bending magnet) and the beam is bent 270 degrees (figure 2.1-3). After traversing through the bending magnet the beam interacts with the target (figure 2.1-4); a piece of tungsten (atomic number $Z = 74$) positioned in a vacuum seal. A fan beam of bremsstrahlung photons are produced from the electron beam interacting with the tungsten nuclei. For clinical electron beams the target is retracted. The photon beam could now be delivered to the patient, but undergoes several stages of field shaping as shown in figure 2.2.

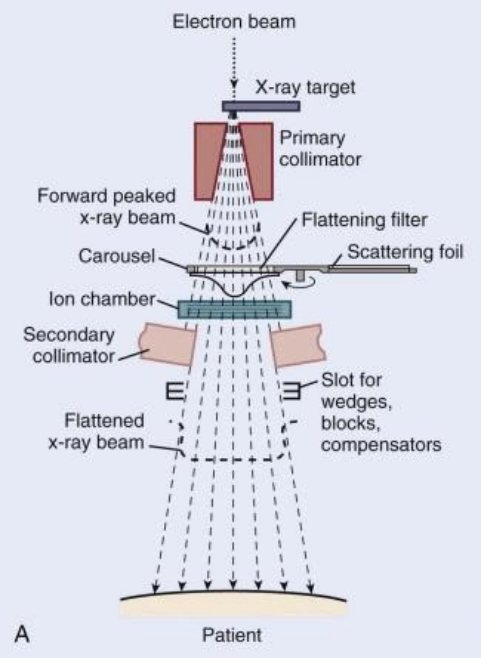

Figure 2.2: Schematic of field shaping steps in the gantry head. An electron beam enters from the top and becomes a shaped photon field before reaching the patient. Profiles for the unflattened and flattened beam is shown as thick dashed lines.

The tungsten target sits directly on top of the primary collimator; a 10 cm thick piece of lead with a conical opening which shapes the bremsstrahlung into a fan beam. The flattening filter (see section 2.1.2) is placed following the primary collimator. It is mounted on a carousel (figure 2.1-5) along with filters used for electron and unflattened photon

beams. Below the carousel sits the ionization chamber which is used to control the linac output, measure the dose and terminate the beam when the planned dose is given. The secondary collimators, or jaws, are located below the ionization chambers (figure 2.1-6). The jaws form the field into a square or rectangular shape with a side length of 3 to 40 cm.

It is possible to produce a non-rectangular field using the Multi-Leaf Collimators (MLC). The MLC has 120 leaflets with a width of 5 and 10 mm. They are organized in two rows facing each other with the thinner leaves in the center of the rows. Each leaf is able to move independently to form a field to a specific tumor shape. The MLC is placed below the secondary collimators. An example of an MLC shaped field is shown in figure 2.3. A visual representation of the final field shape is made possible from a light source inside the gantry head. The ionization chamber is then retracted and a mirror inserted to projecting the field limits down onto the patient surface.

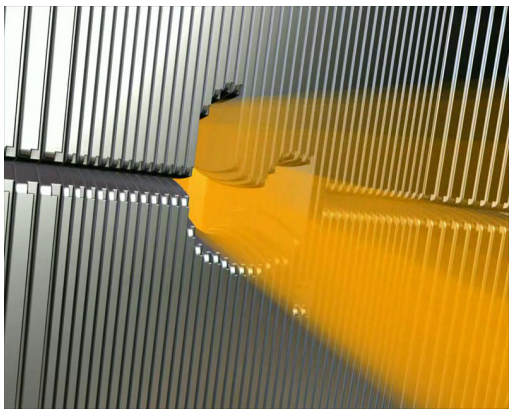

Figure 2.3: Multi leaf collimator producing a conform (fitted to target volume) field. In the figure the 10 mm leaves are seen to the left and right and the 5 mm leaves in the center are involved in the field shaping.

Equipment for x-ray imaging is mounted on the gantry perpendicular to the beam exit. A kilovoltage (kV) imager allows 2D projection x-ray images to be acquired on the accompanying screen. As the gantry is capable of rotation, a simple cone beam CT can be taken with this system as well. Using x-ray images to verify patient positioning before treatment is standard protocol today. The gantry also has a detector screen for MV imaging. This screen is mainly used for periodic quality assurance of the linac.

2.1.2 The Flattening Filter

The beam profile after the target interaction is forward peaked due to the high energy of the incoming beam. This means that the intensity is much higher in the center of the beam compared to the edge. Traditionally one wants to give a uniform field to the tumor so the cone shaped flattening filter is inserted to attenuate away much of the high intensity center. This also has a beam hardening effect. The general profile of the forward peaked beam and the flattened beam can be seen i figure 2.2 and in figure 2.6. A consequence of inserting the filter is that the maximum dose rate (MU/min) from the machine will be reduced significantly, to a maximum of about 600.

It is possible to remove the flattening filter to make Flattening Filter Free (FFF) beams. The clinical use of these beams is relatively new. An FFF beam is capable of providing a dose rate up to 2400 MU/minute at 10 MV. A thin brass foil is used instead for beam hardening but the energy spectrum will still be softer than for a flattened beam. The relative dose contributions (see section 2.2.2) will also be different from a flattened beam.

2.2 Dose and energy absorption in tissue

ICRU defines absorbed dose D as the mean energy $\bar{\epsilon}$ imparted on a mass m (3)

$$D = \frac{d\bar{\epsilon}}{dm}. \tag{2.1}$$

The unit for dose is Gray (Gy) where 1 Gy is equal to 1 Joule per kilogram. X-ray photons deliver their energy to the media they penetrate mainly via the photoelectric effect, compton interactions and pair production. The energy spectrum from the emitted bremsstrahlung radiation is continuous up to the maximum energy determined by the initial acceleration potential. The mean energy is approximately 1/3 of E_{max} after filtration and beam hardening. All three interaction processes are therefore present in clinical radiation beams.

2.2.1 Interaction processes

In the photoelectric effect, the incident photon is absorbed by a bound electron allowing it to escape the atom with a kinetic energy equal to the photon energy $h\nu$ minus the electron's binding energy. The probability σ of an incident photon interacting this way depends on the photon energy and atomic number of the medium through

$$\sigma \propto E^{1/3}$$

$$\sigma \propto Z^3.$$

Soft tissue consists of mostly low atomic numbers (hydrogen, carbon, nitrogen, oxygen all have $Z \leq 8$) and the photoelectric effect is dominant only for energies up to 100 keV, much lower than typical radiotherapy energies.

Pair production happens when the incident photon interacts with the electric field surrounding atomic nuclei in the medium and spontaneously decay into an electron-positron pair. This effect is only possible for energies exceeding 1.022 MeV (rest mass of the electron and positron). The probability σ of pair production then depends on the photon energy and atomic number through

$$\sigma \propto E$$

$$\sigma \propto Z^2.$$

At the highest energies used in radiotherapy pair production will still only account for a small portion of the initial tissue interactions.

The Compton effect is the dominating photon interaction for energies between 100 keV and 10 MeV. The incident photon interacts with a free electron at rest, or outer orbital electron giving away part of its energy as kinetic energy to the electron. Both these particles can then take part in new interactions later. Compton interactions are nearly independent of the atomic number in the media, the probability σ decreases with increasing energy

$$\sigma \propto \frac{1}{E}$$

and the probability os dependent on electron density in the media. The direction of the scattered photon depends on the energy of the initial photon. At higher energies the scattering will be mostly in the forward direction.

2.2.2 Dose contributions in phantom

For a high energy photon beam delivered by the linac, absorbed dose in a patient or phantom has four contributions: primary dose, phantom scatter dose, head scatter dose and contaminant charged particle dose (4). Figure 2.4 illustrates the various contributions. The treatment planning system models the different dose contributions separately (see section 2.4). The primary dose and phantom scatter dose result from incident photons which have not undergone interactions in the treatment head before entering the body or phantom. Primary dose results from an incident ray which deposits its energy directly without being scattered. Phantom scatter dose results from an incident photon which is scattered after entering the phantom and deposits its dose at a different point than the primary photon. Photons undergoing interactions in the gantry head components, mostly

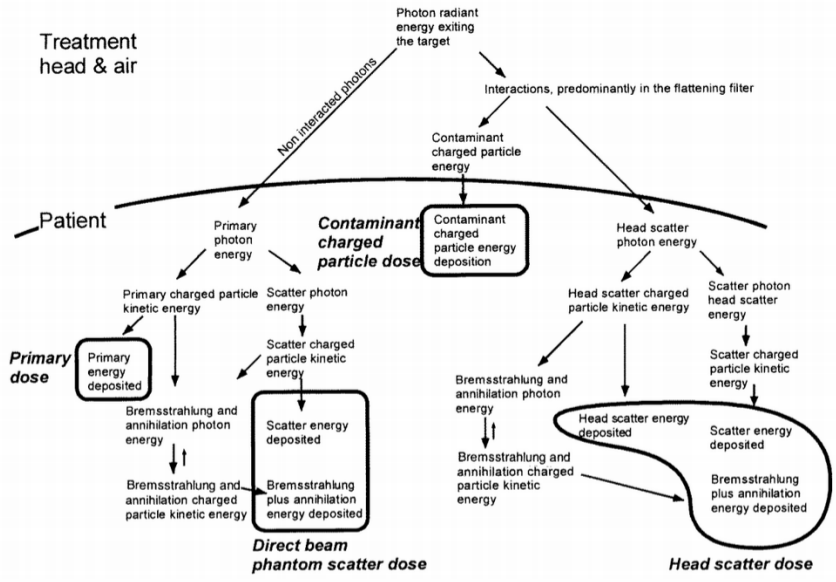

Figure 2.4: Contributions to patient or phantom dose from a radiotherapy beam.

in the flattening filter, are split in the two remaining categories. Contaminant charged particle dose includes charged particles entering the phantom, created either in the gantry head or by interacting with air particles near the phantom. These charged particles have a short range and they are called contaminant because they only contribute to increased

skin dose and dose in the build-up area. Head scatter dose includes the remaining photons entering the phantom after treatment head interactions which may or may not be scattered or undergo further interactions in the phantom. Depending on the beam energy, the head scatter component may be responsible for up to 15% of the total absorbed dose (4). As the majority of the head scatter is due to the flattening filter, FFF beams will not produce most of this dose contribution.

2.2.3 Properties of the radiation field

Along the central axis joining the target and isocenter, the contributions described in section 2.2.2 along with attenuation of the primary beam result in a depth dose curve as shown in figure 2.5. The figure shows three photon energies of field size 10 x 10 cm and a fourth curve shows the highest energy combined with a smaller field size. Lower beam energy will lead to a shallower Dose_{max} while lowering the field size will result in a sharper rise and drop due to less scatter contribution. The distance to D_{max} is typically 1-5 cm for clinical beams in water. The build-up region to the left of dose maximum D_{max}

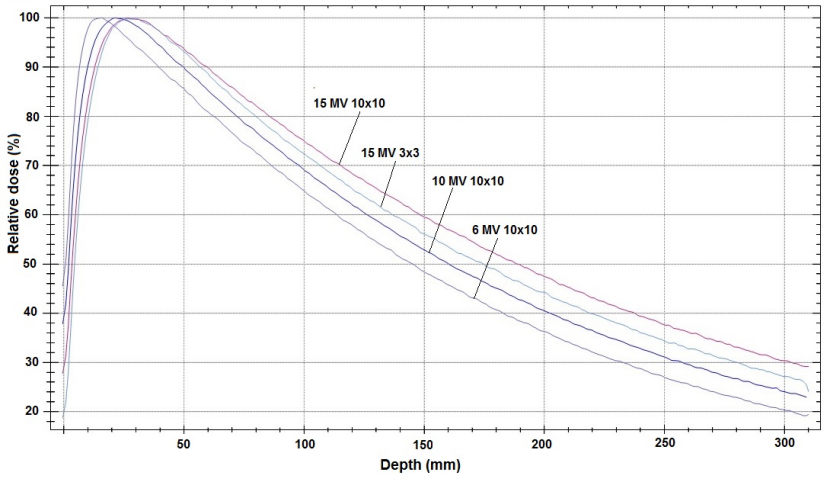

Figure 2.5: Depth dose in a water phantom measured at SB5. The top curve shows energy 15x field size 10x10 cm, below shows energy 15x field size 3x3 cm, energy 10x field size 10x10 cm and energy 6x field size 10x10 cm respectively.

is due to a lack of charged particle equilibrium in this area. A single photon interaction will lead to a cascade of electrons traveling a short distance in tissue. Equilibrium is achieved when the number of electrons created in a unit volume is equal to the number of electrons ending their travel the same volume, which will happen around the depth of electron travel in tissue. Beyond D_{max} the reduced photon fluence will reduce the number of electron cascades and dose deposition. The percent depth dose (PDD) is used to quantify absorbed dose at a depth z normalized to D_{max}.

$$PDD = 100 \cdot \frac{D_z}{D_{max}}. \tag{2.2}$$

The dose profile perpendicular to the central axis is show in figure 2.6 for a flattened beam and and an unflattened (FFF) beam. This figure illustrates the intensity difference in flattening filter free beams. From the dose profile one can define the penumbra as

the the distance where the dose falls at the field edge, often from 80% to 20%. When specifying a field size for the linear accelerator, this size defines the field as it appears in the isocenter plane.

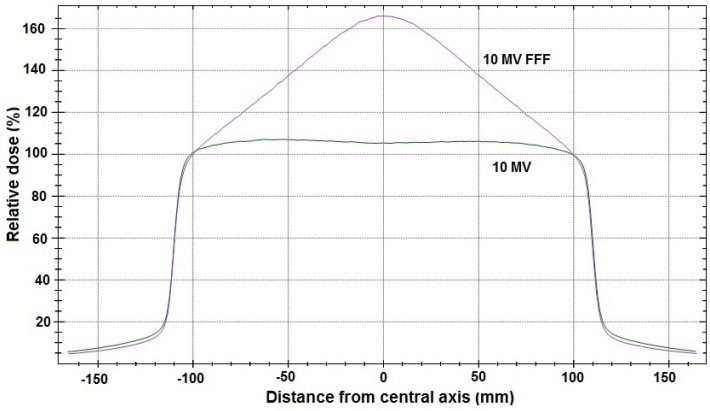

Figure 2.6: Profiles for a 10MV flattened beam (green, bottom) and 10 MV FFF unflattened beam (purple, top).

2.2.4 Monitor Units

Treatment prescriptions from the oncologists are given in Gy, but the linear accelerator output is specified in Monitor Units (MU). This unit relates the power given by this specific machine to produce a certain dose at one point in a patient or phantom. At installation the linac is calibrated for a set MU-to-Gy relationship. A widely used choice is to have 100 MU give 1 Gy at 10cm depth in water for a source-(water)surface distance (SSD) of 90 cm and a field size of 10x10cm in the isocenter plane. The dose per MU depends on machine specific data through the formula

$$\text{Dose per MU} = D_{ref} \cdot S_c \cdot S_p \cdot TPR \tag{2.3}$$

where D_{ref} is the calibration reference dose 1 Gy, S_c is the head scatter correction factor, S_p is the phantom scatter correction factor and TPR is the tissue phantom ratio which is related to the beam quality (5). The reference measurement used for the calibration is done in a large water phantom. When reproducing this condition using water-equivalent plastic (RW3 plates) adequate backscatter must be added beyond the measurement point to compensate for the backscatter done by the large water phantom. 10 cm of backscatter plates is sufficient.

2.3 Treatment planning

When a patient is referred for radiation treatment a new planning CT study is done. The radiation department has a dedicated scanner for this purpose with the same fixation equipment available as will be used by the treatment machine. These new images will better describe the tumor position as it will appear during treatment. The oncologist then delineates (draws contours containing) the different volumes to be irradiated from the CT images and also any other organs which risk being exposed to dose (see section

2.3.1 for volume definitions). This leads to a patient specific set of 3D volumes which is then used by the Treatment Planning System (TPS) to create a treatment plan.

Prescribed dose and risk organ dose constraints for a specific cancer type and tumor position are taken from established national or local guidelines which are based on large clinical studies (2). Some of these dose constraints are given as maximum dose D a volume should receive (D_{cc} = Gy), and others are given as the maximum relative volume V to receive a certain dose Gy (V_{Gy} = % or cm^3). A Dose Volume Histogram (DVH) collects

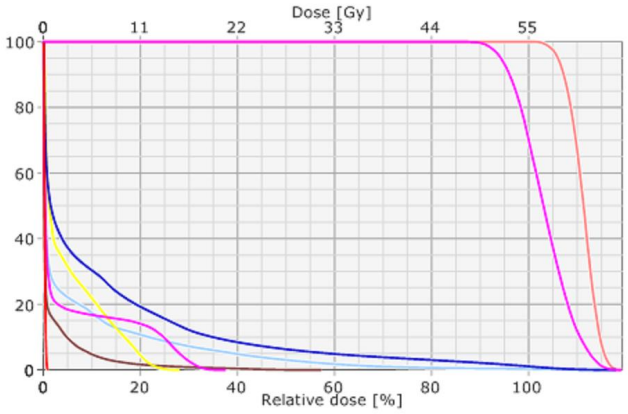

Figure 2.7: A dose volume histogram for a lung SBRT plan. The vertical axis show relative volume in percent. The target volumes are seen to the upper left (100% of the volumes are receiving a large dose) while the risk organs are seen to the lower left (dose drops sharply as one looks at larger parts of the volume). Upper pink curve shows the target volume, blue shows total lung, turqoise shows thoracic wall, yellow shows liver, lower pink shows the medulla and red shows the heart.

the data of absorbed dose in each voxel of the calculated plan and present the data in a differential or cumulative (summation over a dose range) histogram. Figure 2.7 shows an example of a cumulative DVH where one can see the percentage of a volume receiving a dose D or higher. The horizontal axis shows dose (absolute, and percentage of prescribed dose) while the vertical axis shows volume in percent. Absolute volume in cm^3 can also be displayed. The functions for target volumes GTV and PTV can be seen in the upper and right area while the OAR functions can be seen to the left and along the lower side of the histogram. Values for maximum, minimum and mean dose for as well as volumes can be extracted by the TPS which is helpful when analyzing a plan for approval.

2.3.1 Target volume definitions

ICRU report 62 (6) specifies volume definitions to be used in radiotherapy. The hierarchy is shown in figure 2.8. The reason for this standardization is to simplify comparison of plans and treatment techniques and make them more reproducible. Starting at the core, GTV or Gross Tumor Volume, is defined as the palpable or CT-visible tumor and any surrounding positive lymph nodes (GTV-N). Suspected malignant cells in the neighborhood of GTV (sub clinical disease) is included along with the GTV in the Clinical Target Volume CTV. The Internal Target Volume ITV consists of CTV with the Internal Margin (IM) added. This margin accounts for uncertainties in the size, shape and position of the

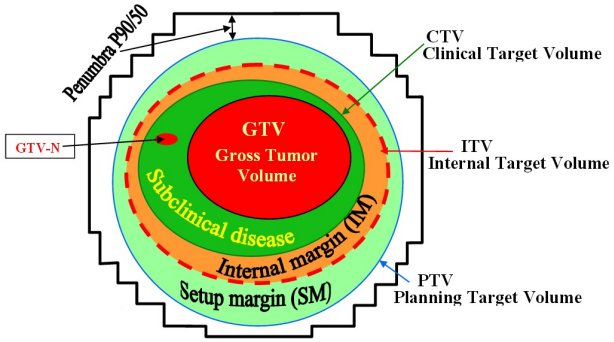

Figure 2.8: Volume definitions in radiotherapy for the tumor and surrounding area. The treatment dose is prescribed to one of these volumes. The margins are used to account for uncertainties.

CTV during the treatment period due to anatomical changes in the patient, and also differences in delineation of the CTV between physicians.

To account for uncertainties in patient movement, positioning or field setup, the Setup Margin (SM) is defined. It is to account for errors both between fractions and also movement within one fraction. The total margin TM cannot be found by a summation of IM and SM, but if they are assumed to be independent of each other the total margin may be found from

$$TM = \sqrt{IM^2 + SM^2}. \tag{2.4}$$

Finally the Planning Target Volume PTV takes the CTV and the Total Margin into account. Dose prescription is often done to the PTV.

Healthy organs in the vicinity of the tumor risk being exposed to radiation during treatment and they are known as Organs At Risk (OAR) or risk volumes. For treatment planning purposes the OAR can be treated as a CTV which is to be avoided or have an upper dose limit. Adding margins to account for organ movement one ends up with a Planning Risk Volume PRV, which is analogous to the PTV. These volumes are helpful for treatment planning to help avoid severe side effects from the treatment. The specific OARs are defined by the oncologist during image delineation.

The relevant OARs for lung treatments include ipsilateral, contralateral and total lung, heart, liver, small intestine, thoracic wall (bones and soft tissue), skin, main bronchi, esophagus, brachial plexus nerves and the medulla, depending on where the tumor is positioned.

2.3.2 Treatment techniques

The advancement of technology has lead to many new techniques in radiotherapy. Normal tissue can be spared to a much higher degree, which has increased the limit of how much dose one can give the tumor without severe side effects. Historically radiation therapy was given as static rectangular fields large enough to cover the tumor and margins with the prescribed dose. Wedges and blocks could be attached to the linac to modify the

field, and using many modifiers meant more time to deliver the plan. Introduction of the MLC allowed for fields conforming to the actual tumor shape to be given, and provided a simpler and quicker way to shield surrounding tissue.

The Intensity Modulated Radiation Therapy (IMRT) technique made it possible to spare surrounding tissue while treating more complex volumes. With the use of several fields from different directions one could shape the dose even in deeper seated oddly shaped tumors. For IMRT treatments the MLC positions can be static (step and shoot) or dynamic (sliding window) where the MLCs move while the radiation beam is on. IMRT typically uses at least twice the number of fields compared to conventional treatment meaning that each session takes up more time on the treatment machine. Today many centers are also using IMRT's time saving, rotational variant VMAT (see section 2.3.4) .

The difference in dose distributions for conventional treatment and VMAT can be seen in figure 2.9 for two lung tumors. The left dose map shows a conventional plan given as three main fields plus two small support fields. The right dose map shows a stereotactic VMAT plan.

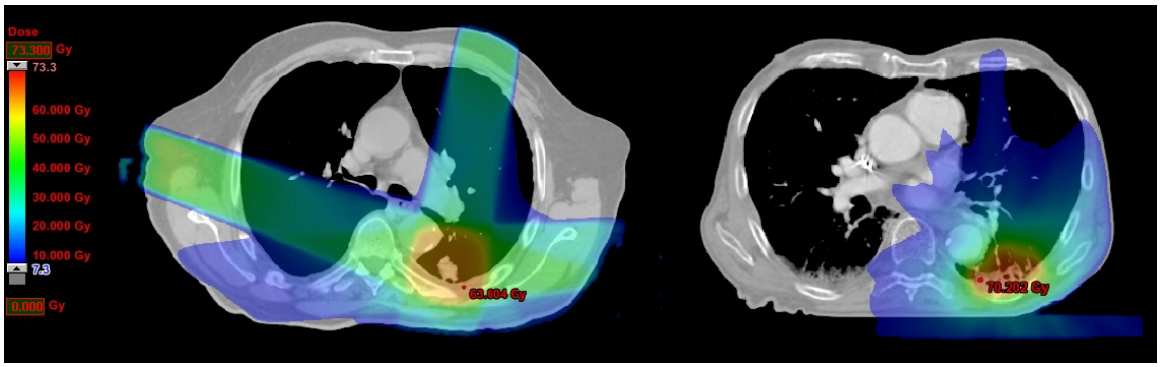

Figure 2.9: Difference in dose distributions for two lung tumors. The dose color scale runs from 7.3 Gy (blue) to 73 Gy (red). It is seen that the left plan (5-field 3D-CRT) results in a dose of 30-40 Gy to a much larger portion of the lung compared to the right plan (stereotactic VMAT). Although central areas in the VMAT plan receive more low dose (less than 10 Gy) this is not as toxic to the tissue and the tumor can receive a higher dose from the VMAT plan (70 Gy vs 63 Gy).

2.3.3 4DCT for breath motion compensation

Respiration changes lung volume and affect the localization of thoracic tumors and surrounding organs which has to be accounted for during treatment planning. This is particularly important for high dose, high precision treatments such as stereotaxia for lung where small margins are wanted. In a 4D-CT series, a sensor is attached to the patient's chest and monitors the frequency of their breath cycle. CT scans are labeled according to which phase of the breath cycle they correspond to. From these CT sets one can find the estimated position of the tumor at all times and the margins can be adjusted to fit with actual movement, which may be different in axial and lateral directions. A maximum intensity projection (MIP) is created which shows the extent of tumor movement and is

used during delineation to define the target margins. A classic CT series is often acquired in addition to be used for patient planning together with the 4DCT data.

2.3.4 Volumetric Modulated Arc Therapy (VMAT)

The VMAT technique is an extension of IMRT. Instead of using a number of static fields one lets the gantry rotate during beam on time. The gantry rotation speed, dose rate and the position of the MLC leaflets change continuously during the treatment. A treatment fraction may consist of one or more full or partial revolution of the gantry. Compared to conventional radiotherapy and IMRT plans, a VMAT plan will spread the non-target dose to a larger volume therefore exposing less normal tissue to high doses. One additional clinical benefit is that the rotational treatment often takes less time overall compared to giving many static fields as one needs less total MUs in the plan. In the clinic, VMAT is beneficial in treating head and neck as well as pelvic tumors due to a reduction in OAR toxicity compared to conventional plans.

The setup of an IMRT or VMAT plan in the treatment planning system is called inverse planning. With conventional plans (forward planning) one would add the desired fields, specify the dose in a reference point and make adjustments adjustment in case some constraints are not fulfilled. With inverse planning dose constrains for maximum and minimum dose as well as a Dose Volume Histogram (DVH) are specified and the TPS optimizes the fields or arc to fit these criteria by running an iterative minimizing algorithm. A full dose calculation is done after. When calculating a VMAT plan the arc is split into discrete arc segments which functions as fields for the dose calculation. Although taking less time to treat, VMAT plans take more time to calculate in the treatment planning process.

2.3.5 Stereotactic Body Radiation Therapy (SBRT)

SBRT refers to extra-cranial irradiation in contrast to Stereotactic Radiosurgery (SRS) which refers to cranial irradiations. Radiosurgery of the brain was the first use of stereotactic radiation techniques (from the 1950s) and extra-cranial use began in the 1990s. The word stereotactic can be translated to high precision and in radiotherapy it refers to delivering a large fraction of radiation to a small fixed target. This can be achieved in different ways, one of which is flattening filter free, VMAT beams.

SBRT requires stricter knowledge of planning and delivery compared to conventional treatments and is not the best choice for all cancers. Clinical studies have been investigating SBRT's role in treating lung, liver, spine, pancreas, adrenal gland and prostate tumors. These tumors are often small, situated near critical organs and may be difficult to treat by surgery. Curation by conventional radiation therapy may not be possible due to risk organ toxicity, or provide adequate local control rates even for small, early stage tumors. Using SBRT to treat inoperable stage T1-2 lung tumors have shown local control rates much higher than conventional radiotherapy and compatible with surgery (2) (8) (9). In addition, radiotherapy is much less invasive than surgery, and is overall a less expensive and time consuming treatment option, offering benefits to both patients and hospitals.

Stereotactic treatments are often planned with little or no margins on the target volumes as the tumor is believed to be either fixed or the location at all times is known from the 4DCT series. The conditions for prescribing stereotactic radiotherapy include a highly reproducible target and patient position, a tumor which is well defined and a certain distance from critical organs, ability to reduce organ movement, and having fixation equipment which is compatible with the planning image modalities (CT, MRI, PET etc). Introduction of integrated imaging systems on the treatment machine was very beneficial to SBRT as imaging could be done without moving the patient.

The ROSEL study on SBRT for stage 1 lung cancers (7) provides recommendations for implementing SBRT in the clinic. It suggests a treatment regime of 20 Gy x 3, alternatively 12 Gy x 5 for tumors near critical organs. Procedures for lung SBRT at UNN are adapted from ROSEL. Indication for treatment is a primary NSCLC tumor less than 6cm across without any nodal infiltration. Periphery T1 tumors with distance to critical organs are given 18 Gy x 3 while periphery T1 tumors close to critical organs and all T2 tumors are given 11 Gy x 5. A tumor less than 2cm from the main bronchi and esophagus is given 7 Gy x 8. The reason for this is the increased risk of a bronchus/esophagus fistula with higher fraction doses in central tumors. Treatment is given every other day as two half arcs to the tumor side using energy 10xFFF. The target dose is prescribed to cover 95% of the PTV making the maximum dose in the GTV up to 140% of prescribed dose. Planning is done by a 4DCT study to detect breath motion and a regular CT study done while the patient holds his breath. As immobility during treatment is more critical, a cone beam CT is used to verify patient and tumor position at each fraction.

2.4 Calculation algorithms

The TPS uses measured beam data together with a mathematical algorithm when estimating the dose to the patient or phantom. There are three types of algorithms; correction based, model based and LBTE (Linear Boltzmann Transport Equation) solvers. Speed and accuracy varies between the different calculation types. Correction based methods models the patient simply as a volume of water with density corrections for heterogeneites. This provides a quick dose estimate in the patient for simple geometries. As treatment techniques have become more advanced it is difficult to achieve the wanted accuracy this way. The increase in available computer power has allowed other calculation types to be used instead.

Model based methods make use of photon fluence and calculation kernels to model how energy is deposited in tissue by performing a convolution. A kernel can be defined as the distribution of energy imparted on a volume element in a medium due to a photon beam incident at the origin of coordinates of the kernel (4). Mainly two types of kernels have been used; the point kernel, and the pencil kernel. In general, point kernels models lateral scatter and inhomogeneities better than pencil kernels and therefore provide better accuracy in heterogeneous media. The benefit to using the pencil kernel is reduced computer processing time as the convolution is done in one less dimension.

The highest accuracy between measurements and dose calculations are acquired from Monte Carlo simulations for solving the LBTE. This is the equation describing radiation transport in a media and its estimations are regarded to be identical to reality for the purpose of radiotherapy dose calculations. The physical interaction processes for radiation transport are known, and simulating these for a large number of photon histories provides excellent compliance. More simulations increase the accuracy, which requires a certain amount of computing power which is often not available in clinical settings. For this reason direct Monte Carlo simulations are not used for routine therapy planning in clinics.

In homogeneous media many algorithms compute very similar dose. The differences between them appear in heterogeneous media with density differences. The algorithms popular in the clinic today, such as AAA and the Collapsed Cone, outperforms the correction based algorithms but show differences compared to Monte Carlo for very low density medium and small field sizes (29). A new algorithm, Acuros, has become available which promise the accuracy of Monte Carlo with reasonable computation times (11).

2.4.1 Anisotropic Analytical Algorithm (AAA)

AAA is a 3D-pencil beam convolution/superposition algorithm available with the Eclipse TPS. It uses pre-computed Monte Carlo simulated beam data and scatter kernels K to calculate absorbed dose in a medium. The pre-computed beam data are simulated for photons in water from a reference linac. When configuring the algorithm for use beam data parameters for photons in water are measured for the clinic linacs and the algorithm beam data is adjusted to fit the properties of each local treatment unit. These new beam data parameters are saved in the TPS database and retrieved during calculation of plans.

The phase space (fluence) of the clinical beam is represented using a multiple-source model. Splitting the beam this way allows more accurate modeling of the total beam. The beam source components are: primary photon energy fluence (primary source), extra-focal photon energy fluence (extra-focal source), contaminating electron fluence (electron contamination) and wedge scatter if applicable. The primary source is modeled from a simulation of the bremsstrahlung photons which do not interact with the gantry head components. Beam hardening from the flattening filter is included in this term. The extra-focal source is modeled as a gaussian plane source located at the bottom of the flattening filter. It models scatter photons originating in the flattening filter and the collimators. This beam will diverge more than the primary beam as this virtual target position is lower than the physical target leading to a larger contribution further from the central axis of the primary beam. When calculating FFF beams AAA will not include this source. Electron contamination is modeled with a depth-dependent curve which describes the amount of electron contamination to be added along the field central axis. It also includes photon contributions not accounted for by the photon sources, such as scatter from air electrons.

The total beam entering the patient is divided into finite-sized beamlets β whose cross sectional area matches the calculation voxel resolution. AAA allows a voxel resolution of 1-5mm. Fluence is assumed to be uniform across the beamlet which simplifies cal-

culations. Each beamlet is modeled using many monoenergetic scatter kernels. The pencil beam kernels describe the energy deposited in a semi-infinite medium from a point monodirectional beam. A polyenergetic scatter kernel K is constructed as a weighted sum of the monoenergetic scatter kernels.

The patient volume is divided into a 3D matrix with the calculation voxels aligned to the beamlet axis. Each voxel is characterized by the mean electron density found from the HU to electron density conversion curve specified in the TPS for the clinic's specific CT. During the calculation beam data parameters from water measurements are scaled according to the densities of the actual patient tissues determined from the CT images. The energy absorption from each beamlet β is found from

$$E_\beta = I_\beta \Phi_\beta \int K_\beta d\Omega \tag{2.5}$$

for a set of coordinates Ω where I is the energy deposition density function modeling attenuation, Φ is the fluence and K is the scatter kernel. The kernel is modeled by the sum of six exponential functions for primary and extra-focal source photons, and as a gaussian function for the contaminant electrons. Separate convolutions are done for each beam contribution and the final energy absorption is found from a superposition of these three terms. Energy absorption in a calculation voxel a is converted to dose via

$$D_a = E_a \cdot \frac{\rho_{water}}{\rho_a}. \tag{2.6}$$

The name anisotropic refers to the way AAA handles tissue heterogeneities. The density scaling of each kernel in the patient volume based on pixel HU value is done separately for sixteen lateral directions depending on the average density between the kernel origin and the calculation point. The algorithm is analytical as most of the function expressions involved enables analytical convolution for dose computation. This reduces the calculation time of treatment plans.

2.4.2 Acuros

Acuros XB (external beam) was developed to provide the accuracy of Monte Carlo calculations while reducing the calculation time to an acceptable level. As an alternative to the statistical analysis done by Monte Carlo, Acuros solves the LBTE numerically. This removes errors from statistical noise common with Monte Carlo but instead introduces systematic errors. These errors are due to Acuros discretizing in space, angle and energy in the iteration process to reduce the calculation time.

Acuros uses the same multiple source model as AAA for primary beam, extra-focal beam and contaminant electron contributions. Calculation of dose to the patient is done in four steps: Transport of source fluence into the patient, calculation of scattered photon fluence in the patient, calculation of scattered electron fluence in the patient, before the final dose calculation is done for the entire volume. Step one is done by ray tracing each beamlet. Step two and three introduce the discretization while solving the LBTE for each voxel. Acuros allows a voxel size of 1-3mm. Step four converts the fluence found in the previous steps to dose using an energy dependent response function.

Contrary to AAA which calculates each field separately, Acuros offers the choice of one calculation for the entire plan regardless of number of fields (plan sum). The drawback to this is that the dose is related to the whole plan and making changes to one field in a conventional plan, such as adjusting the field weight, cannot be done. For a plan sum calculation the ray tracing step is the only step repeated for each field or beam angle while the time consuming scatter calculations are done just once. This significantly reduces the time required for plans with a number of fields, such as VMAT plans. Single fields however require longer calculation times than identical AAA calculations.

Acuros allows the reporting of both Dose to medium and Dose to water, while AAA is limited to dose to water. As it models the physical interactions Acuros is dependent on knowing the chemical composition of the patient tissue to calculate dose. The algorithm gathers data from a database of materials integrated into the TPS which relates the mass density found in each pixel from the CT study to a material composition. The biological tissues included are lung, adipose tissue, muscle, cartilage and bone, in addition there exists a list of relevant non-biologicals. Acuros supports a maximum density of 8 g/cc (stainless steel). Densities higher than 3 g/cc must be assigned a material manually for each CT study.

In step one through three of the calculation AxB solves two time independent coupled particle transport equations for photons and electrons respectively:

$$\Omega\nabla\Psi^{\gamma} + \sigma_t^{\gamma}\Psi^{\gamma} = q^{\gamma\gamma} + q^{\gamma} \tag{2.7}$$

$$\Omega\nabla\Psi^{e} + \sigma_t^{e}\Psi^{e} - \frac{\partial}{\partial E}(S_R\Psi^{e}) = q^{ee} + q^{\gamma e} + q^{e} \tag{2.8}$$

Here Ψ is the angular fluence, Ω the direction of angular fluence, σ_t is the total macroscopic cross section, S_R is the radiative and collision stopping power, q^{ii} the scatter sources and q^{i} the particle sources for photons γ and electrons e and energy E. After the fluence for all energy groups is calculated, dose D in a voxel a is found from

$$D_a = \int dE \int d\Omega \frac{\sigma^e(r,E)}{\rho(r)}\Psi^e(r,E,\Omega) \tag{2.9}$$

where σ^e is the macroscopic electron energy deposition cross section, ρ is material density and Ψ^e is electron fluence. When Dose to water is chosen σ^e and ρ are dependent on water instead of material properties of voxel a.

2.5 Dosimetry and verification of treatment

Quality assurance in radiotherapy is important and both equipment and treatment plans have their own individual QA protocols. The linear accelerator undergoes periodic calibration checks and patient position is verified before each treatment via the on board imagers (see section 2.1). Many types of dosimetry equipment exist for use in radiotherapy. For absolute dose determination of linac output an ionization chamber is used. This is considered to be the most accurate method of dose determination as the ionization chamber has been calibrated against the SSDL standard. Readings from the chamber

measurements and its relation to absolute dose is based on cavity theory (see section 2.5.1). In the clinic ionization chambers are mainly used to measure point doses in water phantoms. Figure 3.10 show examples of ionization chambers.

The advanced treatment techniques have their own plan verification which require more than point dose measurements. Radiochromic film has been used extensively in IMRT verification. The film consist of a thin sheet which changes color upon exposure to radiation. The color change can be directly related to absorbed dose for each pixel. The film's advantage over other methods is very high spatial resolution, no post-exposure chemical processing, near tissue equivalence, no energy dependence and a dynamic range which covers all relevant doses in radiotherapy. The response in the film is collected using a densitometer which will be explained in detail i chapter 3.2. To stabilize the color change it is recommended to wait about 24 hours before reading off the film.

Semiconductor diodes can also be used to measure point doses. As diodes can be made very small a large number of them can be placed together to form an array detector. The spatial resolution of such an array is lower than radiochromic film but the advantage is immediate readout of results. Results from film or diode arrays can be compared to calculated plans using the gamma analysis tool (see section 2.5.2).

2.5.1 Bragg-Gray cavity theory

Cavity theory provides the conditions for measuring absolute dose in a media by inserting a detector (cavity) and relating its signal to what would be the dose in this point without the detector in place. The Bragg-Gray conditions assume the thickness of the cavity to be small compared to the path length of the charged particles crossing it, so that the cavity does not perturb the charged particle field (create or absorb electrons). This can be fulfilled using a cavity material which has similar mean path length as the surrounding media. For electrons the cavity material needs to be close in atomic number to the media surrounding it. In addition the absorbed dose in the cavity is assumed to be deposited entirely by charged particles crossing the cavity walls, meaning that no charge is produced or ends its path in the cavity, only in the surrounding medium.

Under these conditions, and assuming the fluence of particles is equal in the cavity and medium (fulfilled for charged particle equilibrium), the ratio of absorbed doses in the surrounding media and the cavity can be found from the average mass collision stopping power ratios. For a gas ionization chamber cavity the dose in the D_{cavity} can be found from the charge produced in the chamber gas Q, mass of the gas m and the mean energy W spent to produce a unit charge in the gas $\frac{W}{e}$. The dose in the nearby surrounding media can be found using D_{cavity} multiplied with the ratio of mass stopping powers S/ρ of the media and cavity

$$D_{media} = \frac{Q}{m}\left(\frac{W}{e}\right)_{gas} \cdot \frac{(S/\rho)_{medium}}{(S/\rho)_{gas}}. \tag{2.10}$$

The stopping power S is defined as energy loss per unit path length averaged over all energies due to collision and radiative energy losses and differs between materials.

2.5.2 The Gamma Analysis method

Comparing the dose differences of the two distributions directly will not always give information beneficial for verifying the plan. In areas with low dose gradients a dose difference comparison will be useful as a large differences are due to a large spatial error. For high dose gradient areas one might see a large dose difference for a small spatial error. This is expected and does not mean the plan should be rejected. The concept of Distance To Agreement (DTA) was proposed for use in high dose gradient areas instead. This criterion looks for the smallest distance between a reference point and one point in the evaluated dose map which exhibits the same dose. DTA cannot be used as the deciding criterion in low dose gradient areas as it might report a large spatial error between very small dose differences. As the two criteria compliment each other the they are used together when testing one dose plan against a reference.

Low et al (14) proposed a technique using these two criteria and presenting the results quantitatively. Known as gamma analysis, it generates a value γ for all points in a distribution. This γ value contains information about the magnitude of any disagreement in the dose difference and DTA test. The maximum allowed dose difference ΔD and DTA value Δd (acceptance criteria) are chosen and the γ is normalized relative to these values. In the clinic these criteria are often 2% / 2mm. A geometric representation of these conditions for a reference point D_m and evaluated point D_c is shown in figure 2.10. The points and distances with subscript m refers to the reference point while subscript c refers to the evaluation point. For gamma analysis of a VMAT plan the reference points are those measured in the phantom and are considered to represent the true dose which will be absorbed in the patient, while the evaluated points are the corresponding points in the calculated Eclipse distribution. In figure 2.10 the xy-plane represent distance to

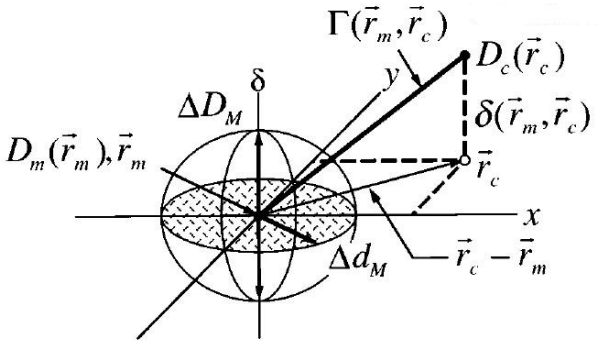

Figure 2.10: Evaluation criteria for combined ellipsoid dose difference and DTA tests. The xy-plane represent distance to agreement (DTA) while the δ axis represent absolute dose difference.

agreement while the δ axis represent dose difference. The disk in the xy-plane centered at r_m with radius Δd_M shows the maximum allowed DTA. The vectors pointing along the δ axis shows the maximum allowed dose difference. An ellipsoid can be constructed from this disk and these vectors. The equation for this surface seen in figure 2.10 is

$$1 = \sqrt{\frac{(|r - r_m|)^2}{\Delta d^2} + \frac{(D(r) - D_m(r_m))^2}{\Delta D^2}}. \tag{2.11}$$

The distance Γ representing the distance between the reference point and a point in the evaluated distribution is

$$\Gamma(r_m, r_c) = \sqrt{\frac{(|r_c - r_m|)^2}{\Delta d^2} + \frac{(D_c(r_c) - D_m(r_m))^2}{\Delta D^2}}. \tag{2.12}$$

While performing the gamma analysis for a point measured by the phantom, each point in the evaluated distribution is searched until the closest agreement to the reference point is found. From this one can define the gamma value

$$\gamma(r_m) = min\{\Gamma(r_m, r_c)\}\forall\{r_c\} \tag{2.13}$$

as the closest agreement between the reference and evaluated point. If the evaluated point falls within the ellipsoid defined in equation 2.3 the point at r_m passes the gamma evaluation. This leads to the gamma criteria

$$\gamma(r_m) \leq 1 = \text{Gamma approved}$$

$$\gamma(r_m) > 1 = \text{Gamma failed} \tag{2.14}$$

The gamma analysis is a versatile tool which can be applied to both continuous and discrete data gathering methods such as radiochromic film, gel, ion chamber and diode point measurements. The method as described above provides a quantitative tool where the γ value gives information about the amount of which a point passed or failed the gamma criterion. Software for gamma analysis is usually equipped to display these data as both gamma maps and histograms where one can investigate single points of interest and see the proportion of gamma values in the distribution. A common clinical condition for verifying a plan is if 95% or more points in the distribution passes the gamma criterion.

Chapter 3

Materials and methods

3.1 The linear accelerator

The TrueBeam accelerator from Varian Medical Systems (Palo Alto, CA, USA) was used for all irradiations in this study. The University Hospital of North Norway, Tromsø (UNN) operates two TrueBeam accelerators. As they collect their beam configuration data from the same database and therefore are considered to provide identical output, both the accelerators (referred to as SB4 and SB5) were used at different times depending on which was available. SB4 and SB5 can provide the following photon energies: 6MV, 10MV and 15MV (from now referred to as 6x, 10x and 15x) as well as the flattening filter free energies 6MV and 10MV (referred to as 6xFFF and 10xFFF). Figure 3.1 shows SB4.

Figure 3.1: Varian TrueBeam linear accelerator at the department of radiotherapy, UNN.

3.1.1 Treatment planning system

The Eclipse treatment planning system (Varian, CA, USA) was used for all plan calculations. UNN has the AAA and Acuros algorithms version 10.0.28 available (see section 2.4). Unless specified otherwise, the AAA algorithm was used for dose planning.

3.2 Film dosimetry in a lung phantom

The two algorithms investigated are expected for perform differently in heterogeneous media. To say that one algorithm is more accurate than the other require knowledge about the actual absorbed dose. An attempt at measuring absolute dose in a lung phantom was done using radiochromic film. The response in the film was digitalized using a flatbed scanner before being related to absorbed dose using the film analysis software VerA. UNN's procedure for verification of IMRT treatments using film was followed for the digitalization process. This procedure was based on recommendations from the Norwegian Radiation Protection Authority (21) and was established for the film type EBT in 2008. As film dosimetry was conducted using the film type EBT3 for the first time, characterization of the film was done to investigate any differences in response from the previous model.

3.2.1 GafChromic EBT3 film

GafChromic EBT3 dosimetry film produced by Ashland, Inc (Covington, KY, USA) is a self-processing radiochromic film usable for dosimetry in high energy radiotherapy. EBT3 is their latest version and promises improvements over its popular precursors EBT and EBT2 (17). The film consists of one active layer, approximately 30 μm incorporated between two 125 μm layers of polyester as seen in figure 3.2. The active layer contains

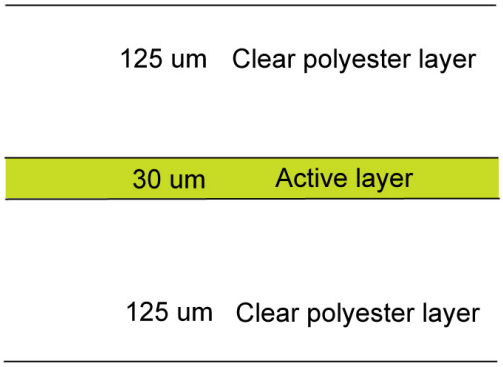

Figure 3.2: Composition of GafChromic EBT3 film.

the active component; needle-shaped polymers, along with a yellow marker dye. When exposed to radiation the active component polymerizes reducing the optical density in the film and turning it blue. The effect can be seen within seconds and can be quantized and converted to absorbed dose using a densitometer or a flatbed scanner with transmission mode capability. The latter method is often used in radiotherapy settings.

The yellow dye is incorporated in the active layer to allow the use of multi-channel dosimetry when calibrating the film. The polyester coating contains silica particles which maintains a small air gap between the film and the scanner surface preventing interference patterns during scanning. EBT3 film is near tissue equivalent, has low energy dependence and is usable for doses between 0.01 Gy and 40 Gy. For dosimetry it provides one of the best resolutions possible among simple dosimetry equipment at 25 μm. The film is insensitive to visible light but reacts to UV light and should be stored in a light-shielded place.

The polymers created in the film has higher absorption of wavelengths of 500-650 nm compared to unexposed film. This explains why the film appears blue upon irradiation. The highest absorption peak is at 636 nm (corresponds to red color) and therefore the red color channel is used when extracting information from the film during image processing. The producer of the film recommends the red color channel for doses up to 10 Gy (19).

3.2.2 The lung phantom

A phantom was constructed to view the dose distribution around a tumor in lung tissue using the radiochromic film. The phantom was created using the I'mRT phantom cube (Scanditronix Wellhofer, Schwarzenbruck, Germany) filled with material corresponding to lung tissue and a large solid tumor as shown in figure 3.3. The I'mRT phantom cube measures 16x16x16 cm internally and 18x18x18 cm externally with 1 cm walls of water-equivalent RW3 material on all six sides.

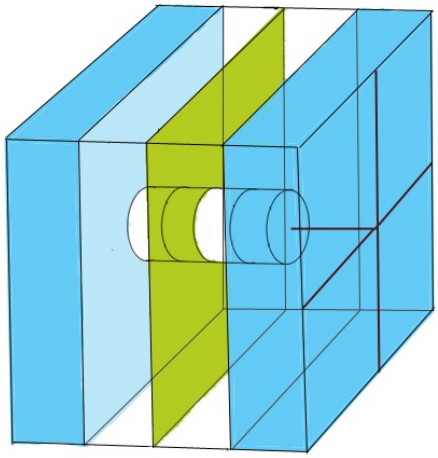

Figure 3.3: Construction of the lung phantom for film irradiations. Four blue styrofoam blocks are used as lung material. The blue color of the two center blocks in this figure is omitted for clarity. A segmented cylindrical tumor is visible in the center of the cuboid. The tumor passes through the two center blocks while the outer two blocks are left intact. The film sheet, shown in yellow, can be inserted between the two center blocks and through the center of the tumor to measure the dose in this plane. The red lines on the right outer side show the positioning of the tumor cylinder.

The tumor was constructed from water-equivalent plastic using circular disks of RW3 with density 1.1g/cm^3. The full tumor was cylindrical with diameter 4cm and length 8cm. For simple lung phantoms cork is often used as the low density material (13), but the material was not available. Instead, styrofoam with density 0.04g/cm^3 was chosen to represent lung tissue. This density corresponded to 'very light lung', normal lung density is used as 0.2 g/cm^3 (29) (27) (26). The low density material was chosen to better view the differences between the two algorithms when calculating in heterogeneous media.

The styrofoam was cut into four cuboids measuring 16x16x4cm each, and would fill the phantom cube with minimal air pockets between the lung and phantom walls. A circular

hole was cut from the two center blocks to fit the cylindrical tumor in the center of the lung. Thin medical tape was used to hold the tumor disks in place inside the styrofoam blocks. A sheet of radiochromic film measuring 16x16cm could then be placed between the two center styrofoam blocks and measure the dose in a plane through the tumor.

3.2.3 Epson V750 Pro scanner

Epson V750 Pro is a flatbed scanner with the ability to scan A4 sized films in transmission mode. The light source is a cold cathode fluorescent lamp and the detector is a CCD crystal array. In transmission mode the scanner detects light intensity transmitted through the film. High transmission correspond to a high pixel value and a low measured dose. The scanner software provides several methods of image improvement but all of these were disabled during scanning of the film. Films were scanned in professional mode, positive film, 48 bit RGB color, 127 dpi to a TIFF file of 800 x 800 pixels. A custom made cardboard frame of size 16x16 cm previously used in IMRT film verification was used to place the film on the scanner glass surface. Figure 3.4 shows this setup. In addition, a second frame was cut from GafChromic EBT film to place the smaller calibration films inside the cardboard frame. Three scans were taken of each film after an initial ten minute scanner lamp warm-up as specified in the IMRT verification procedure. There was a 20-22 hour wait between irradiation and scanning of the film.

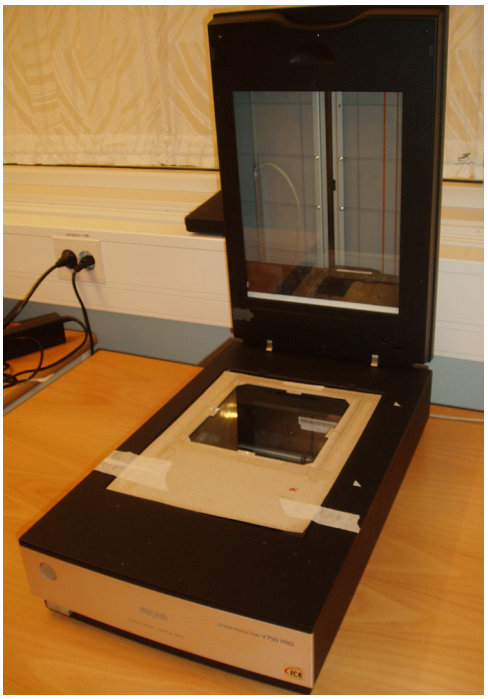

Figure 3.4: Epson V750 Pro scanner used for film digitalization.

The film will scatter some of the light emitted from the scanner lamp. When scanning film pieces covering the majority of the scanner area more light will be scattered towards the center of the film than the edges. Quantifying this difference has shown a parabolic shape of the measured pixel value for a given dose. This has been referred to as the lateral effect (25) and can cause errors in measured dose. Film orientation relative to the scanner lamp is also important as light scatter is affected by the direction of the polymers in the

film. Per film manufacturer suggestion all films were scanned in landscape orientation as to minimize this effect (19).

3.2.4 VerA analysis software

The IDL based software VerA has been used by many radiotherapy departments in Norway to compare film measurements to calculated dose plans. An extension was made by Kuttner (22) and was used by UNN for film IMRT verification. VerA allows import of a scanned RGB TIFF image, extraction of data in the red color channel, creation of a calibration curve, conversion to absolute dose from this calibration curve and comparison of this scanned image to a dose map exported from Eclipse TPS. When selecting a pixel in the scanned image VerA reports the pixel value and standard deviation as the pixel value is averaged for the 9 x 9 pixels surrounding the selected point. An example of this is shown in figure 3.5 for collecting the response in the film for creating the calibration curve.

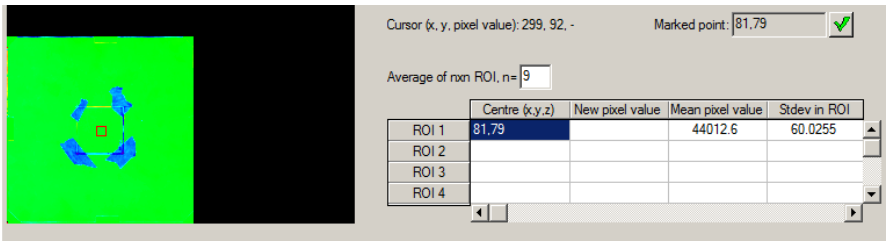

Figure 3.5: Selection of a pixel in VerA for creation of a calibration curve. Pixel position on the 161 x 161 pixel grid is shown to the upper right. The green section to the left is the scanned film. Dose (in Gy) or MUs is put in the nee pixel value column when creating the calibration curve.

Comparison tools include continuous and discrete gamma analysis, and isodose curve comparison. Kuttner's extension included a module for noise reduction in the film image using background correction and pixel averaging filters. This module was used in the processing of the film. The 800 x 800 pixel raw image was then reduced by a factor of five to a 161 x 161 pixel image with a resolution of 1 mm before being compared to the dose distribution from Eclipse. VerA displays the TIFF image and the Eclipse dose distribution as color intensity maps of absolute dose. A visual comparison of the two distributions is possible to do. A map of gamma values is displayed the same way. Examples of these maps are shown in section 4.1.3.

3.2.5 FilmQA Pro analysis software

FilmQA Pro (Ashland Inc, Covington, KY, USA) is made by the manufacturer of Gaf-Chromic films specifically to process and analyze dosimetric film. Similarly to VerA it allows comparisons between imported dose maps to scanned film images after performing an absolute dose calibration based on pixel value. Its advantage over VerA is that FilmQA Pro uses multi channel dosimetry which has shown to reduce noise and scanner artifacts in the processed image (45). A calibration curve is created for each color channel based on optical density (OD) as opposed to pixel value in VerA. An example of this calibration curve is seen in figure 3.6. The calibration curve function is then rational linear instead

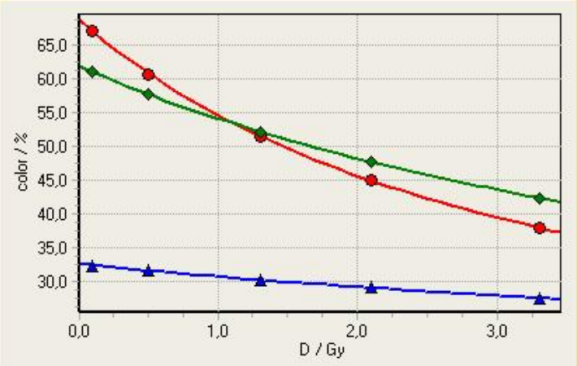

Figure 3.6: Calibration curve for multi channel dosimetry in FilmQA Pro. One curve is set up for each color channel.

of fourth degree polynomial. Optical density is found through the relationship

$$OD = log_{10}(\frac{\text{maximum pixel value}}{\text{pixel value}}) \tag{3.1}$$

Maximum pixel value is given by the image bit value and is $2^{16} - 1 = 65535$ for the red channel of a 48 bit image. FilmQA displays the TIFF image of the scanned film in true colors and the dose distributions imported from Eclipse as a grayscale image. A visual comparison will not show the same details as shown in VerA. After gamma analysis is performed a color map of gamma values is displayed with a color intensity map similarly to VerA.

3.2.6 Film measurement setup

Prior to the film irradiations a CT scan of the lung phantom with film in place was done for treatment planning purposes. One plan was created for each energy investigated; 6x, 6xFFF, 10x and 10xFFF. The plan contained a single 10x10 cm open field and the dose prescription was 2 Gy to isocenter. The number of MU given for these plans were 169 MU for energy 6x, 163 MU for energy 6xFFF, 178 MU for energy 10x and 171 MU for energy 10xFFF. Isocenter in the treatment plan was chosen to be the center of the tumor in the plane of the film, which is also the geometric center of the phantom.

In this setup the styrofoam blocks and the film were standing upright in the phantom cube when placed on the treatment couch and the beam would hit the film parallel to the film surface when gantry was set to 0°. Dose map matrices for film comparison was exported in DICOM format from Eclipse with image size 161x161 pixels and a resolution of 1 pixel per mm to fit the properties of the scanned films. The phantom as irradiated can be seen in figure 3.7.

Two sets of data were collected on separate days, the last set to check for reproducibility. On each day one 16x16 cm film in the lung phantom was irradiated for each of the four energies. At the same time a set of 4x4 cm calibration films were irradiated with specific MU values for energy 6x only. The range for these values were decided from the estimated maximum dose of 2.53 Gy in the treatment plans.The MU values for film calibration were

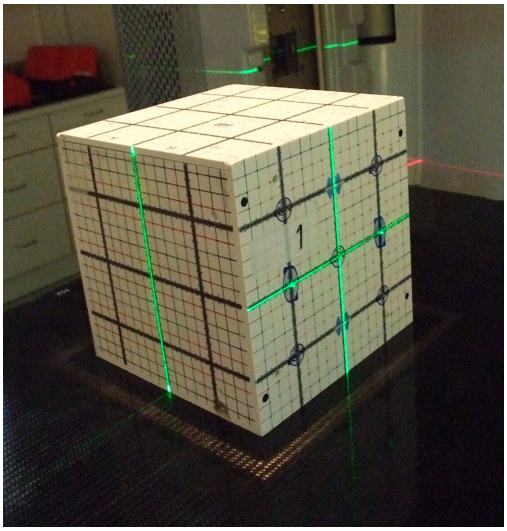

Figure 3.7: Lung phantom positioned for irradiation.

chosen to cover 10 MU to 330 MU corresponding to $D_{max} + 20\%$ per suggestion from the film manufacturer. The calibration films were irradiated in a water equivalent phantom (RW3 phantom) simulating the reference conditions of the linac (see section 2.2.4). This was done using RW3 plates positioning the film at 10cm depth with 15cm backscatter material and the films were exposed to a single 10x10cm open field with the gantry position set to 0°. The geometric center of the film was positioned in the isocenter as shown in figure 3.8. In this setup 100 MU should correspond to 1 Gy and absolute dose could be deduced from the other MU values from a linear MU-to-Gy relationship.

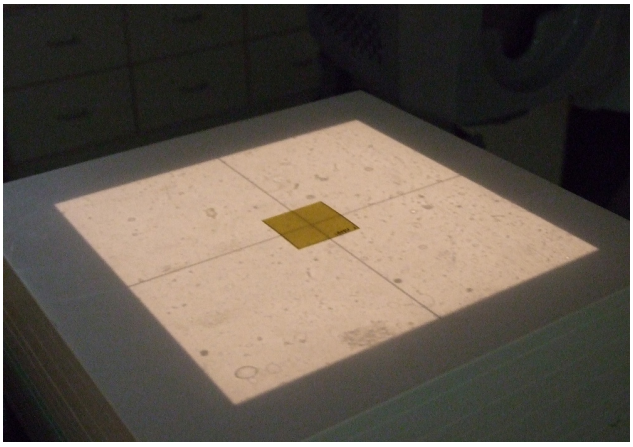

Figure 3.8: Positioning of the calibration film in the RW3 phantom. Figure shows the film positioned in the isocenter plane on top of 15 cm RW3 plates. 10 cm of plates were then placed on top of the film.

The calibration films were exposed to a beam perpendicular to the film surface while the lung phantom films were exposed parallel to the film. The film manufacturer claims the film has no angular or energy dependence and a test was done to show this. Film sheets of 4x4 cm were used to measure angular dependence and energy dependence in the film. The sheets were exposed to 100 MU from a single energy 6x, 10x10cm open field at a depth of 10cm in the RW3 phantom with 15cm backscatter plates. The angular depen-

Table 3.1: Film measurement setup. Four phantom films and one set of small calibration films were irradiated on each of the two days.

Day	Irradiation	Calibration
1	4 films in lung phantom	30, 50, 90, 130, 170, 210, 250, 290, 330MU
2	4 films in lung phantom	10, 30, 50, 90, 130, 170, 210, 250, 290, 330MU

dence was measured for beams parallel (gantry 270°) and perpendicular (gantry 0°) to the film. Six angles surrounding each reference angle were chosen as described in table 3.2.

The center of the 4x4cm films were positioned in the isocenter to produce 1 Gy in the film in the two reference angles. To measure the same dose for the seven parallel angles the phantom and film was shifted to position the isocenter at 10 cm depth from the side of the phantom as shown in figure 3.9. For the energy dependence five films were placed in the same setup as for the perpendicular angle films and irradiated with 100 MU. Energy 15x was included in addition to the four investigation energies as this was a general film characterization.

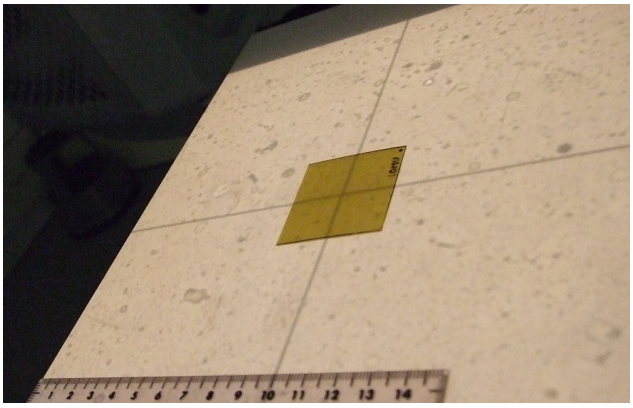

Figure 3.9: Positioning of the parallel angle films for gantry angle 260-280. Treatment couch was shifted so the isocenter was positioned 10 cm from the left side of the RW3 phantom.10 cm of RW3 plates were then added to the top.

Table 3.2: Film dependence setup. One film was irradiated for each measurement point.

Dependence check	Measurement points	Used as reference
Parallel angles	260, 265, 268, 270, 272, 275, 280	270
Perpendicular angles	350, 355, 358, 0, 2, 5, 10	0
Energy	6x, 10x, 15x, 6xFFF, 10xFFF	6x

Ionization chamber measurements were used to confirm doses measured in the film for the calibration and angular dependence setups. A Farmer ionization chamber type FC65-G was placed at 10cm depth in the RW3 phantom using the dedicated chamber insertion

plate and irradiated with the same MU values and gantry angles as the film. A Dose1 electrometer (IBA Dosimetry, Schwarzenbruck, Germany) collected the charge which was then converted to absolute dose using the work sheet for high energy photon beams provided by IAEA with the TRS398 report (42). For the angular dependency tests around the parallel angles the setup differed slightly between the film and the chamber. As the RW3 plate for the Farmer chamber could only support insertion of the chamber in the center one could not measure 1 Gy in for the parallel angles without changing the treatment plan and give more MUs. Farmer chamber measurements were then taken at 15cm depth (SSD=85cm) for the parallel angles. Figure 3.10 show the Farmer and CC01 (see section 3.4) ionization chambers.

Figure 3.10: Top: Farmer ionization chamber FC65-G. Bottom: CC01 ionization chamber.

3.2.7 Additional measurements in a homogeneous phantom

To investigate whether the lung phantom construction and density affected the film measurements, sheets of radiochromic film was irradiated in the homogeneous RW3 phantom. To produce a simple but non-uniform field wedges were used to create a dose gradient in one direction. The filter free energies did not have wedges configured on the linac, therefore only energy 6x and 15x was used in the test.

A CT scan of the phantom was done and a dose calculation was performed with AAA in Eclipse. For energy 6x a 10 x 10 cm field with the EDW60IN wedge in place was irradiated with 200 MU. The film was placed flat in the phantom, perpendicular to the beam at 10 cm depth in the RW3 phantom with 15 cm backscatter plates. The film center was located in the isocenter. For energy 15x the same field was given 183 MU. This should produce 2 Gy in the center of both films. Film calibration was done for MU values 10-330 given to 4 x 4 cm film sheets like in the earlier tests. In addition, point dose measurements were done in the RW3 phantom using the Farmer FC65-G ionization chamber to verify the calibration values. Gamma analysis was then performed in VerA.

3.3 Ionization chamber dosimetry in a lung phantom

In addition to comparing dose distributions surrounding a tumor the general behavior of AAA and Acuros in low density media was investigated. Fogliata et al compared the be-

havior of various dose calculation algorithms in a water-lung phantom (29). Particularly low density lung showed large difference in calculated dose between various calculation algorithms and Monte Carlo. A dose calculation difference in low density media between AAA and Acuros has been found by Bush et al (26) and Hoffmann et al (32).

A phantom similar to that used by Fogliata and Bush was constructed to be used with a CC01 ionization chamber (Scanditronix Wellhofer, Schwarzenbruck, Germany) and measure point doses. The CC01 chamber was chosen for its small volume of $0.01cm^3$ which allowed better resolution point measurements to be done in the media with as little influence as possible. Figure 3.10 shows the CC01 ionization chamber below the Farmer ionization chamber. The thin tip to the right is the active detector volume, the rest of the construction is the connection wires.

3.3.1 Lung phantom for point dose measurements

A lung phantom was constructed to perform point dose measurements using the CC01 chamber detector. The same styrofoam material as used in the film phantom were used to simulate lung tissue. A bed for the detector was made by carving a 5 mm deep slot in a 30x30x2 cm styrofoam plate as seen in figure 3.11. An additional styrofoam plate with a carved slot for the top of the detector laid on top and these two plates were bound tightly together using medical tape. The detector chamber was now effectively positioned in the geometric center of the two bound plates.

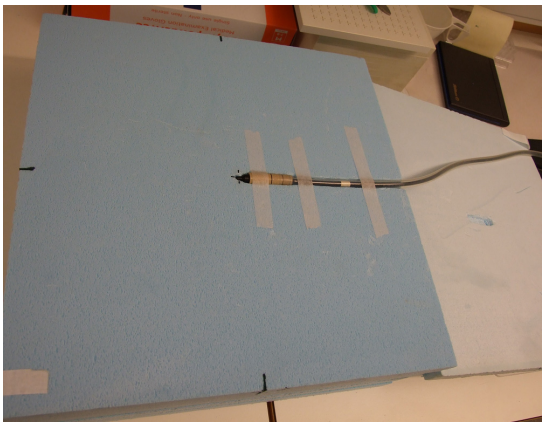

Figure 3.11: CC01 ionization chamber placed in the styrofoam plate slot. The right plate (lighter blue) is laid on top before binding them together.

A total of eight styrofoam plates were used to create a lung volume which measured 30 x 30 x 16 cm. The two plates containing the detector could be moved up and down relative to the other six plates for a total of seven depth measurement points along the beam central axis. 5 cm of RW3 water plates were added to the top and bottom to create buildup and backscatter areas. The weight of the top RW3 plates was thought to keep the styrofoam plates pressed close together to avoid air gaps. The different measurement points were then located at 7, 9, 11, 13, 15, 17 and 19 cm depth in the phantom (phantom depth), corresponding to 2, 4, 6, 8, 10, 12 and 14 cm depth in lung material (lung depth).

3.3.2 Measurement setup

The phantom positioned on the linac treatment couch can be seen in figure 3.12. A CT study of the phantom was done for treatment planning purposes. Separate scans were done with the detector positioned in each depth. The images indicated no air gaps between the styrofoam plates. The isocenter was chosen to be the center of the phantom, creating an SSD of 87 cm and placing the detector in the isocenter at measurement point 4. The chamber volume was delineated in the CT images and defined as PMMA material with a density of 1.19 g/cm^3. As the CC01 chamber consists mainly of near water equivalent materials, a small gas volume and a steel electrode a material with density slightly higher than water (1.0 g/cm^3) was thought to be the most correct for this situation.

For each of the four energies two field sizes were irradiated, 3 x 3 cm and 10 x 10 cm, to see the effect for small fields which is relevant to stereotactic treatments. The prescribed dose was 1 Gy to isocenter for each plan given as a single beam from a gantry positioned in 0°. The MU per plan can be seen in table 3.3.

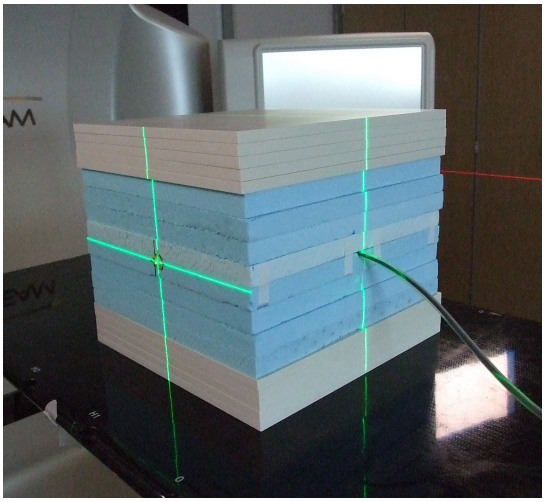

Figure 3.12: Lung phantom for CC01 measurements. Detector is placed in the isocenter plane, measurement position 4 of 7.

Table 3.3: Plan specifics for CC01 irradiations in lung phantom. A constant SSD of 87 cm was used and the gantry position was 0°.

Energy	Field size (cm^2)	MU given
6x	3 x 3	169
6x	10 x 10	119
6xFFF	3 x 3	160
6xFFF	10 x 10	117
10x	3 x 3	158
10x	10 x 10	120
10xFFF	3 x 3	151
10xFFF	10 x 10	122

Dose in each measurement point would be found from equation 2.10 as the Bragg-Gray criterion was assumed fulfilled by using the small ionization chamber. However, the mass stopping power S/ρ was unknown for the lung material. To relate measured charge to absorbed dose in media, the data was compared to measurements made in water using the equivalent depth comparison where the measured depths in water is scaled relative to the density difference between the media. Normally one would measure in water first and then find water-equivalent depths in the lung, but in this experiment the lung phantom construction decided the measurement depths, and the water depths were calculated from these.

For the water measurements the CC01 ionization chamber was placed in the BluePhantom water phantom (Scanditronix Wellhofer, Schwarzenbruck, Germany). Four of the seven depths measured in the lung phantom were chosen for comparisons. These were the points corresponding to lung phantom depth 7, 13, 17 and 19 cm. The focus was on the deeper positions to reduce interface perturbation effects which would occur in the lung but not the water phantom. As the density of the lung was 2.5% to that of water, Equivalent Water Depths were used as a substitute for lung depth in the BluePhantom. They were found from the relationship

$$EWD = \text{lung depth} \cdot \frac{\rho_{\text{lung}}}{\rho_{\text{water}}} \tag{3.2}$$

where ρ is the density of the materials, which was 0.04 g/cm^3 for lung and 1.0 g/cm^3 for water. Because 5 cm of RW3 plates were added to the lung depths for measurements the actual measurement depth in the BluePhantom was EWD + 5 cm. The measurement depth plus SSD had to be equal for both data sets an effective SSD for the water phantom was found from

$$\text{Effective SSD} = 87cm + \text{lung depth} - EWD. \tag{3.3}$$

Positioning of the ionization chamber in the water phantom supported a resolution of 0.1mm, while the resolution for setting the SSD on the TrueBeam accelerator made it necessary to specify the effective SSD in the nearest half centimeter. Table 3.4 shows the depths and effective SSDs used. The MU given was identical to the lung phantom plans shown in table 3.3. By performing the equivalent depth comparisons, and at the same

Table 3.4: Measurement points in the lung phantom and water equivalent depths and measurement points in water phantom

In lung phantom		In water phantom		
Phantom depth	Lung depth	Phantom depth	EWD	Effective SSD
7 cm	2 cm	50.8 mm	0.8 mm	89 cm
13 cm	8 cm	53.2 mm	3.2 mm	94.5 cm
17 cm	12 cm	54.8 mm	4.8 mm	98.5 cm
19 cm	14 cm	55.6 mm	5.6 mm	100.5 cm

time assuming that the relationship between the scattering factors of the lung material and water is constant with depth, the measured dose in the lung should differ from the

measured dose in water by a constant C which is thought to be close to unity. This constant can be extracted when comparing the two sets of measurements and used to adjust the dose detected in the lung phantom.

3.4 Replanning of patients with Acuros

A comparison of lung SBRT plans calculated by AAA and Acuros was done to investigate the difference between the calculations in the presence of low density media. Ten SBRT patients previously planned and treated at UNN using AAA were replanned using Acuros. The patient volumes, beam data and VMAT optimalization constraints were identical to the original AAA plan. This ensured the same number of MU for the AAA and Acuros plans and a comparison of estimated volume doses from this MU could be done. Table 3.5 lists the patients and their plan details. PTV_{lung} refers to the the PTV excluding the tumor, or PTV_{lung} = PTV - GTV.

Table 3.5: Details for the patient plans used for Acuros replanning.

Patient	Tumor location	Fractionation	PTV (cm^3)	PTV_{lung} (cm^3)
1	Right lung	11 Gy x 5	86.1	44.6
2	Right superior lung	18 Gy x 3	10.5	9.50
3	Right inferior lung	11 Gy x 5	64.8	35.3
4	Left lung	18 Gy x 3	11.5	10.3
5	Right lung	11 Gy x 5	35.6	24.8
6	Left lung	18 Gy x 3	12.2	11.3
7	Left lung	11 Gy x 5	88.9	63.6
8	Left superior lung	11 Gy x 5	15.9	12.9
9	Right superior lung	11 Gy x 5	40.2	34.0
10	Left superior lung	18 Gy x 3	13.1	10.6

A new patient volume was added to compensate for high density pixels in the CT images which fall outside Acuros automatic material assignment. This volume was defined using the CT ranger and collecting all points with a CT number higher than 2800 HU before adding a 1 mm margin to include forgotten neighborhood pixels. This volume contained different objects for the different patients including: the 4DCT sensor and wire, part of the thorax fixation equipment, pacemaker and wires, small areas of bone in the shoulder and sternum and vascular contrast material. The volume was assigned a CT value corresponding with nearby soft tissue; 50 HU for two patients and 150 HU for the remaining eight patients. This volume was located far away from the treatment field in all patients and was assumed to not affect the calculation.

Previous patient plans were exported from Eclipse and anonymized using Oncentra MasterPlan (Nucletron, Columbia, MD, USA) before being reimported to Eclipse for replanning. The AAA plans were recalculated to ensure that none of the parameters had changed in the export process compared to the original plan. The Acuros plans were calculated

using a 2.5 mm grid size, the same as the original AAA plan.

Plans were compared by extracting absolute doses for various volumes from the DVH and calculating the difference between AAA and Acuros in percent. The volumes investigated were: GTV, PTV, left, right and total lung, thoracic wall and medulla PRV (medulla + 3 mm margin). In addition, average calculation times were noted for comparison.

3.4.1 Delta4 verification

The Delta4 (ScandiDos AB, Uppsala, Sweden) phantom is a diode array detector designed for 3D verification of VMAT plans. The phantom body is cylindrical with a diameter of 22 cm, length 40 cm and the detectors are surrounded by polymethyl methacrylate (PMMA) blocks acting as a tissue equivalent media (16). The diodes are of p-type silicon and are arranged in two perpendicular planes inside the phantom along the cylinder axis. A total of 1069 diodes provide two detector areas of 20 x 20 cm. The diodes are spaced closer together in the center of these two planes to increase the resolution in the area where the tumor is often located.

The phantom is calibrated against an ionization chamber and is capable of measuring absolute doses. The idea is that the measurements in these two planes are representative of the dose measured in the entire 3D volume. The accompanying software for the phantom is capable of performing gamma analysis against a calculated patient plan. As the phantom is made from homogeneous PMMA the measurements cannot be compared with calculations done on a patient CT image. Instead the proposed patient plan is projected onto the CT image of the Delta4 phantom and calculated as dose to phantom. PMMA has the density 1.19 g/cm^3 and ScandiDos estimates the CT number to be 217 HU. This is regarded as water-equivalent for the sake of patient verification.

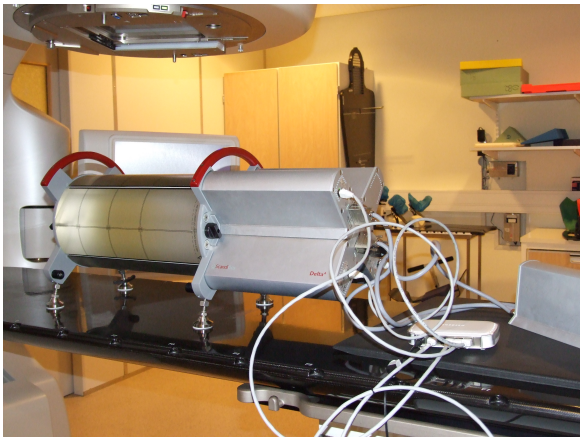

Figure 3.13: The Delta4 phantom used for verification of patient VMAT plans. The cylinder section to the left contains the detector arrays, the grey X-shape to the right contains the on-board electrometer and data processing units for relating charge to absorbed dose.

Figure 3.13 shows the Delta4 phantom positioned on the treatment couch ready for patient verification. The phantom cylinder has markings to easily position the phantom center in the machine isocenter using the lasers. Verification plans were created and calculated

using Acuros for three of the patients. This was patient number 4, 6 and 9. Their AAA plans had been verified prior to the original patient treatment, but was verified again for reference as the phantom had undergone a calibration since the original verification. Comparison of the two verification plans to find which plan fit the best with measurements was considered unimportant as the phantom was water equivalent. The focus was to see if the Acuros verification plans would pass the gamma analysis using the same criteria as for AAA plans. This criteria was ΔD = 2%, Δd = 2 mm and more than 95% of points must pass to verify the plan.

Chapter 4

Results

4.1 Film dosimetry in a lung phantom

4.1.1 Angular dependence of the film

To investigate whether the beam direction onto the film affected the measured dose, a total of twenty-one small films were irradiated from from directions perpendicular to and parallel to the film plane. Two sets of seven films were done for the parallel angles as the first set exhibited unreasonable deviations and only the second data set is presented here. The mean pixel value in the center of the film was collected in VerA and used to create adjusted pixel values for gantry angles near the perpendicular reference 0°and parallel reference 270°. Adjusted pixel value was found from

$$\text{adjusted pixel value} = \text{mean pixel value} \cdot \frac{D_{\text{chamber}}}{D_{\text{chamber ref}}} \tag{4.1}$$

where the dose D is the absolute dose as measured by the ionization chamber. Equation 4.1 should effectively remove the difference in pixel value resulting from a longer path through the phantom compared to the reference angle and produce a pixel value corrected for a small dose difference. Non-adjusted pixel values covered a range of 800 for the parallel angles and 250 for the perpendicular angles. Results for the adjusted pixel values are shown in figure 4.1. It is observed that the range of the pixel values for the perpendicular angles are less than the range of the individual parallel angles. The standard deviation of the mean pixel value found in VerA was almost twice as high parallel to the film (range 104-184) compared to perpendicular to the film (range 57-105). When matching one perpendicular and one parallel angle for the same position relative to the reference angles the difference in adjusted pixel value was less than 200 (of about 35 000) for all but two relative positions tested. A change in pixel value of 200 corresponds to a change in absorbed dose of about 2.5% for a dose of 1 Gy (given to these films).

4.1.2 Energy dependence of the film

Energy dependence was investigated similarly to angular dependence by collecting the mean pixel value at the film center from VerA and adjusting the pixel value relative to ionization chamber doses using equation 4.1. $D_{\text{chamber ref}}$ was chosen to be energy 6x as the calibration curve was done for this energy. Results can be found in figure 4.2. No energy dependence was observed in the film, in accordance with manufacturers specification.

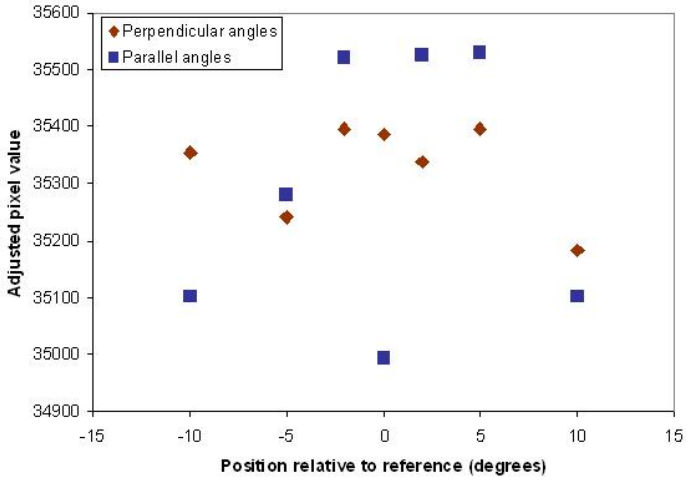

Figure 4.1: Results from a test of angular dependence in the film. Seven angles each for a beam parallel and perpendicular to the film were investigated. Mean pixel value was adjusted relative to the given dose measured by the ionization chamber which should result in equal response (pixel value) in the film.

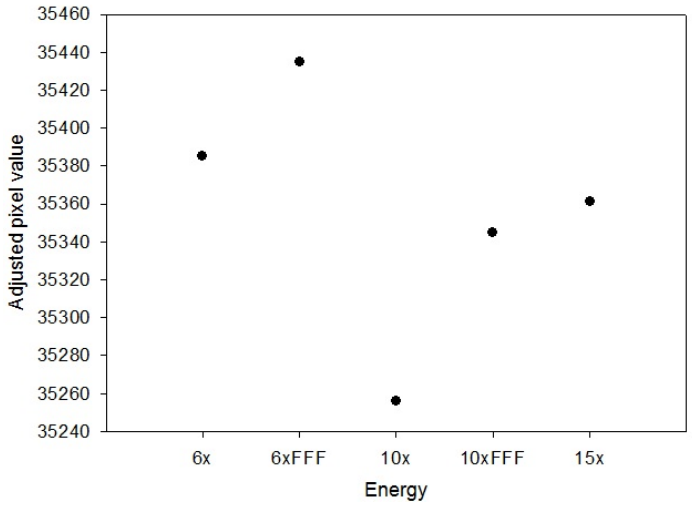

Figure 4.2: Results from a test of energy dependence in the film. 6x was used as reference. Mean pixel value was adjusted relative to the given dose measured by the ionization chamber which should result in equal response (pixel value) in the film.

4.1.3 Film analysis in VerA

Data for film calibration can be seen in figure 4.3. When calibrating the film it was assumed that 100 MU correspond to 1 Gy and absolute dose can be found for the full dose range from the same linear MU-to-Gray relationship. Fitted curve function details are shown in table 4.1 for absolute dose D.

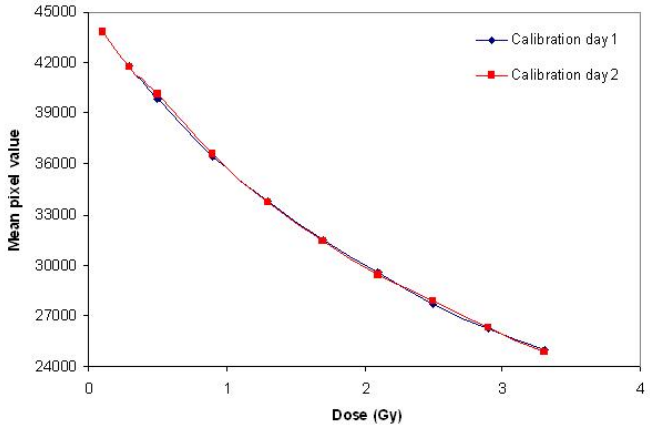

Figure 4.3: Calibration curves used for film measurements. Monitor units are converted to absolute dose which is then related to mean pixel value in the film pixels.

Table 4.1: Fitted functions used for the calibration curve setup.

Calibration	Fitted polynomial function	R^2 value
Day 1	$114.49D^4 - 1028.5D^3 + 4126.6D^2 - 12683D + 45246$	1
Day 2	$-91.73D^4 + 403.76D^3 + 909.58D^2 - 10143D + 44790$	0.999

An example of response in the film after background correction and median filtering in VerA is shown in figure 4.4 for a film irradiated on day 2. The figure show the calculated and measured dose distribution used for gamma analysis for energy 10xFFF. Calculated dose maps and film measurements are put side by side for a visual comparison. The top row shows AAA (left) and the film (right) and the bottom row shows Acuros (left) and the film (right). The film is identical in both rows. For this energy it looks like AAA calculates higher dose in the lung near the beam entrance compared to Acuros. The film measures less dose in the tumor and beam entrance area compared to the calculations. Additional dose maps can be found in appendix A1.

After processing each film in VerA a continuous gamma analysis was done comparing each film to the corresponding calculated plan. The measured and calculated dose maps were matched in position according to the best visual overlay of the circular tumor. $\Delta D = 2\%$ and Δ d = 2mm conditions were used for gamma analysis. A comparison of absolute dose in the center of the tumor (pixel position 80,80) was also done by extracting the point dose from VerA. Gamma maps produced by VerA are separated based on energy and shown in figures 4.5, 4.6, 4.7 and 4.8 for the four energies 6x, 6xFFF, 10x and 10xFFF.

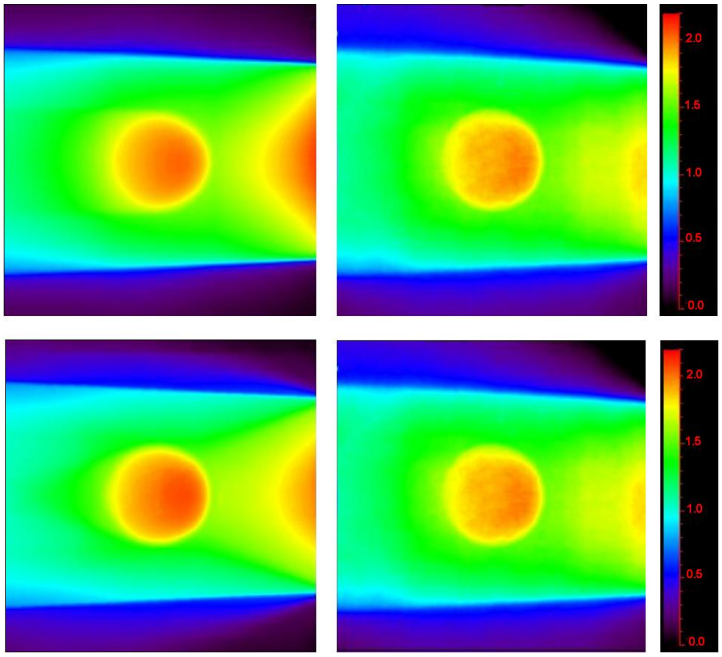

Figure 4.4: Dose distributions day 2 for energy 10xFFF. Top shows comparison between AAA (left) and film (right). Bottom shows comparison between Acuros (left) and film (right). The two film distributions are the same. The color scale shows absolute dose in Gy up to a maximum dose of 2.2 Gy.

The color scale runs from $\gamma = 0$ (black) to $\gamma \geq 3$ (red). Pixels of dark blue, purple or black colors passes the gamma criterion $\gamma \leq 1$. Doses of less than 0.3 Gy are set to be automatically approved (black). In the figures the beam has entered horizontally from the right to the left and the location of the circular tumor is visible in the center. The top row in each figure show AAA-film analysis (left) and Acuros-fim analysis (right) for day 1 irradiations, the bottom row show the same for day 2 irradiations. The phantom is given the same number of Monitor Units and beam settings for both irradiation days.

In the figures it is seen that there are large areas of pixels which does not pass the gamma criterion (green, yellow and red) for all energies, particularly in the lung region. Day 1 and day 2 irradiations are expected to produce identical results for a given energy but none of the energies show this. Films irradiated on day 2 provided better compliance at some energies and opposite at others. There is no clear indication of any superior energy or calculation algorithm based on the gamma analysis. Most tumor pixels appear to pass the gamma analysis for energy 6x on irradiation day 1 while many of them fail on irradiation day 2. Increasing the gamma criterion up to $\Delta D = 5\%$ and $\Delta d = 5$ mm did not increase the gamma passing rate significantly.

The dose difference measured in the center of the tumor and percentage of approved gamma results are shown in table 4.2. Half of the investigated dose differences in isocenter passed the gamma criterion (no more than 2% dose difference between the calculated and measured plan). The tumor appears to have more gamma approved pixels compared to the lung tissue. The penumbra region also show areas of approved pixels even if the rest of the plan fails.

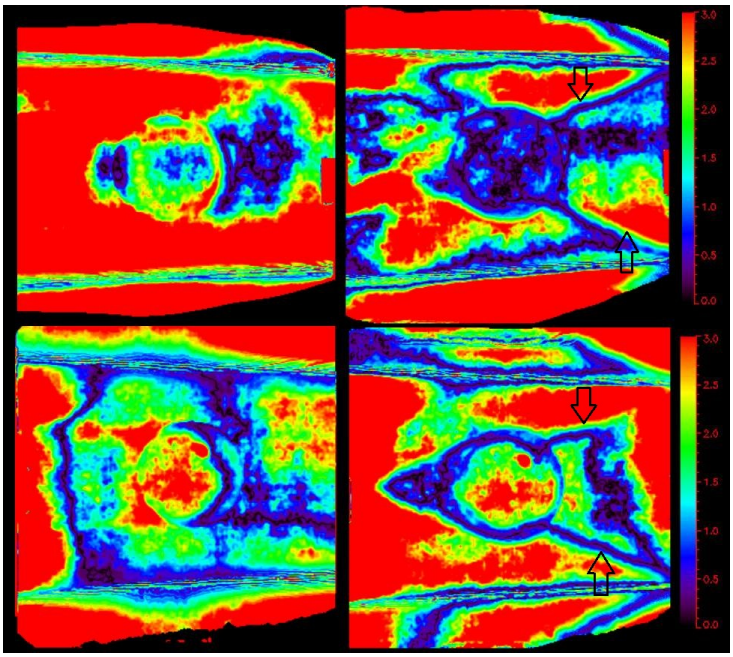

Figure 4.5: Gamma analysis results for film dosimetry in a lung phantom done at energy 6x. Top row shows day 1 results and bottom row shows day 2 results from AAA-film analysis (left) and Acuros-film analysis (left). The color scale runs from $\gamma = 0$ (black) to $\gamma \geq 3$ (red). Plans are approved for $\gamma \leq 1$. The radiation beam enters the phantom from the right to the left. The arrows point out a visual effect found in the Acuros analyses for all energies.

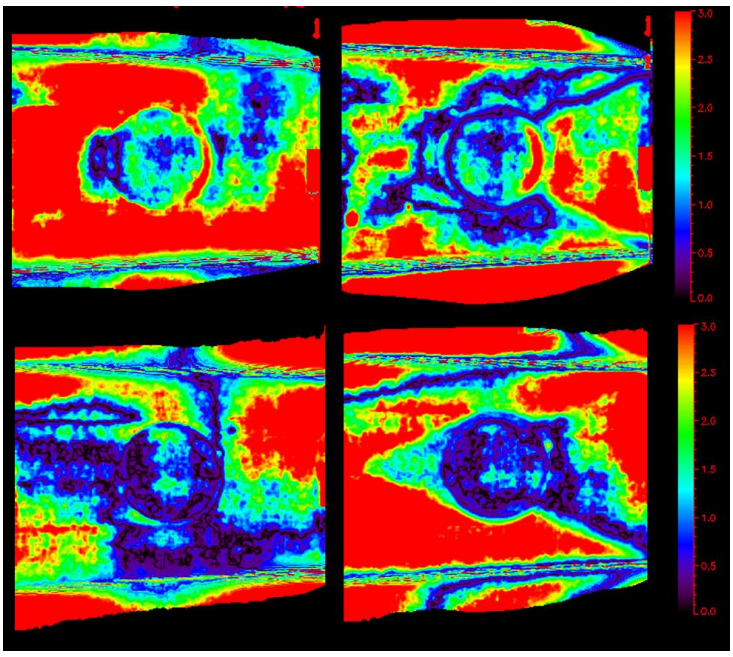

Figure 4.6: Gamma analysis results for film dosimetry in a lung phantom done at energy 6xFFF. Top row shows day 1 results and bottom row shows day 2 results from AAA-film analysis (left) and Acuros-film analysis (left). The color scale runs from $\gamma = 0$ (black) to $\gamma \geq 3$ (red). Plans are approved for $\gamma \leq 1$. The radiation beam enters the phantom from the right to the left.

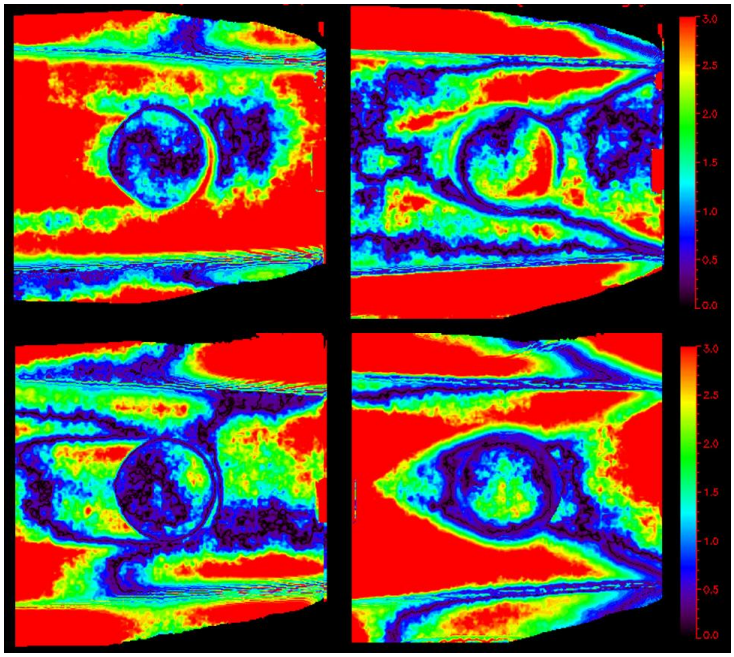

Figure 4.7: Gamma analysis results for film dosimetry in a lung phantom done at energy 10x. Top row shows day 1 results and bottom row shows day 2 results from AAA-film analysis (left) and Acuros-film analysis (left). The color scale runs from $\gamma = 0$ (black) to $\gamma \geq 3$ (red). Plans are approved for $\gamma \leq 1$. The radiation beam enters the phantom from the right to the left.

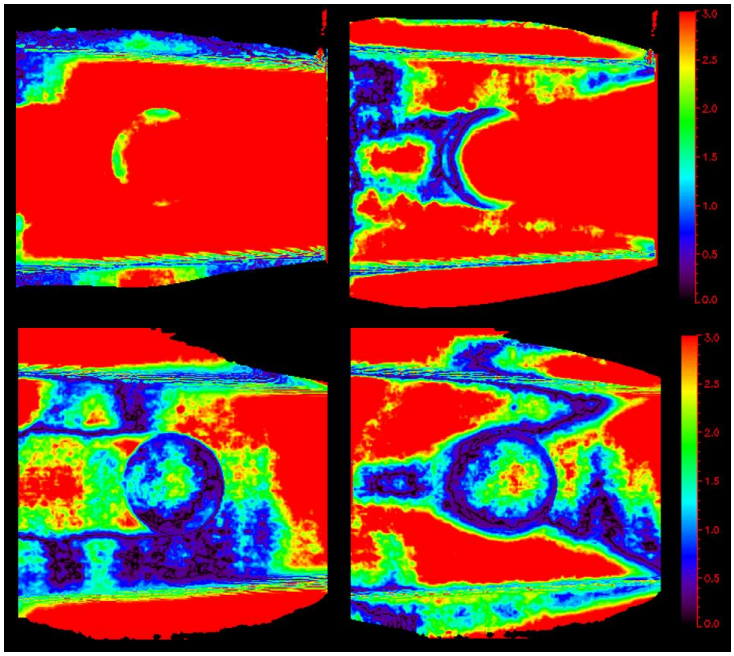

Figure 4.8: Gamma analysis results for film dosimetry in a lung phantom done at energy 10xFFF. Top row shows day 1 results and bottom row shows day 2 results from AAA-film analysis (left) and Acuros-film analysis (left). The color scale runs from $\gamma = 0$ (black) to $\gamma \geq 3$ (red). Plans are approved for $\gamma \leq 1$. The radiation beam enters the phantom from the right to the left.

Table 4.2: Dose difference in the tumor center and the total number of gamma approved pixels in the lung phantom measured with radiochromic film. AAA and Acuros are compared to the same film. The criterion for passing a given plan is more than 95% of pixels passing the gamma criterion.

Energy	Dose difference tumor center(%)		Number of pixels passing (%)	
and day	AAA	Acuros XB	AAA	Acuros XB
6x day 1	1.7	1.0	31	41
6x day 2	4.7	5.8	29	32
6xFFF day 1	1.7	1.6	38	42
6xFFF day 2	1.6	1.6	49	37
10x day 1	0.1	3.5	36	41
10x day 2	0.1	3.8	40	31
10xFFF day 1	10	10	36	32
10xFFF day 2	3.6	4.4	37	34

In the Acuros to film gamma maps here is a diagonal line of approved points extending from the penumbra on the beam entrance side to the tumor and beyond it. This line is shown with arrows in figure 4.5. It is not visible in the AAA gamma maps. The effect is also visible as straight isodose curves in the Acuros dose calculations exported from Eclipse, particularly for filter free energies. AAA exhibits a more curved isodose in the dose calculation.

Depth dose profiles through isocenter for 10xFFF irradiated on day 2 are shown in figure 4.9. These depth dose profiles correspond to the distributions in figure 4.4. For this particular film Acuros provides a better fit along the central axis. This can also be observed in the gamma map in figure 4.8. However, the profile across the central axis is not well matched for Acuros leading to the low gamma passing rate of 34%.

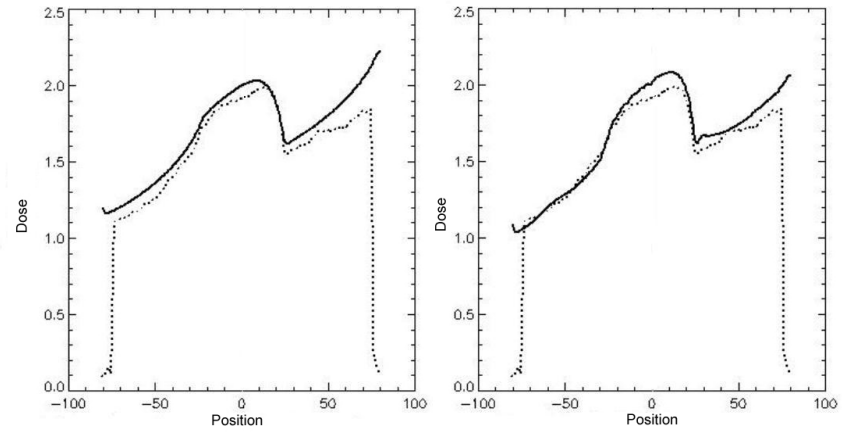

Figure 4.9: Depth dose curve comparisons for AAA and film (left) and AxB and film (right) on irradiation day 2 for energy 10xFFF. The solid line is the calculation and the dotted line shows the film measurement. The figure shows absorbed dose along the central axis through the tumor for a beam entering from the right.

4.1.4 Film analysis in FilmQA Pro

The FilmQA software was used to compare the gamma passing rates from the films to the gamma passing rates found by VerA. This could indicate whether the unexpected low passing rates in VerA were due to the film or the processing software. A set of calibration curves were constructed using the steps outlined in the software user guide (31). Five MU values were chosen for the calibration: 30, 50, 130, 210 and 330 MU for day 1, and 10, 50, 130, 210 and 330 MU for day 2 films. A linear MU-to Gy relationship was assumed. Fitting function was chosen as color rational (linear) vs dose as suggested in the user manual.

Gamma maps from day 1 irradiations can be seen in figures 4.10 and 4.11. Green pixels are approved while red pixels failed the gamma analysis. The maps exhibit the same general appearance as the VerA gamma maps. The diagonal line along the isodose curve is observed for Acuros and is absent for AAA. Comparing the gamma maps to VerA maps, a visual difference in these comparisons is the many small dots which can be observed in the gamma maps for all energies and both algorithm comparisons. They do not appear in the film TIFF image or calculated dose distribution displayed in FilmQA Pro, only in the gamma distribution.

From the FilmQA Pro gamma maps it appears as Acuros performs slightly better in front of the tumor while AAA peforms better behind the tumor. Consistency between these gamma maps and those found in VerA was not found. An example of this is the large areas of failed points behind and on the side of the tumor in the Acuros calculations for 6x and 10x. The are not seen in the VerA gamma maps. Similarly, most of the tumor pixels in the AAA calculation for 10xFFF looks to be approved, or close to approval in the FilmQA Pro gamma map, while they all failed in the VerA gamma test. Fiducial points were not used to mark the maps as there were no matching points on the scanned film images.

Table 4.3 shows the percentage of approved gamma in the FilmQA Pro software using the same dose map position matching as in VerA and 2% / 2mm conditions. Higher passing rates were observed compared to the VerA analysis but none of the plans passed the gamma test in FilmQA Pro. AAA performed better than Acuros in all but one comparison.

Table 4.3: Gamma approved in FilmQA Pro

Energy and day	Approved gamma (%)	
	AAA	Acuros XB
6x day 1	80	66
6x day 2	59	42
6xFFF day 1	86	67
6xFFF day 2	80	50
10x day 1	81	40
10x day 2	65	36
10xFFF day 1	58	74
10xFFF day 2	87	50

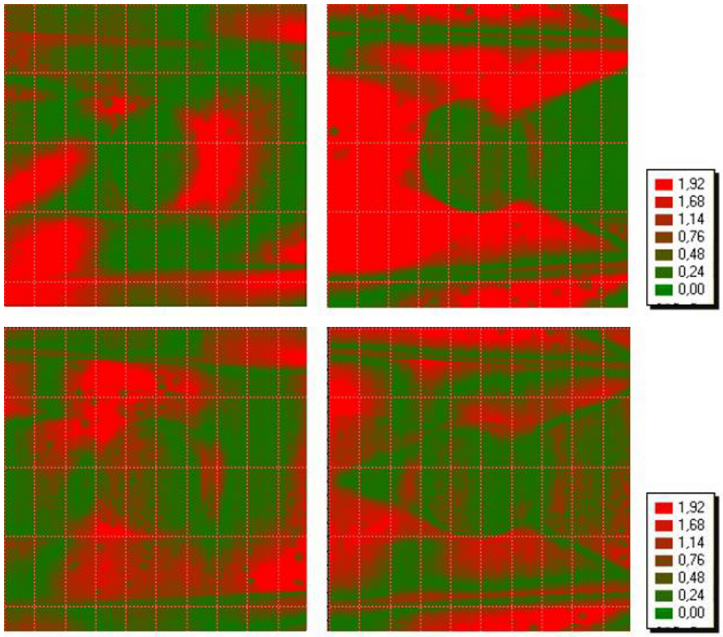

Figure 4.10: Gamma analysis results from FilmQA Pro for energy 6x (top row) and 6xFFF (bottom row) for AAA (left) and Accuros (left). Comparisons are for day 1 films. The color scale is seen to the right and runs from $\gamma = 0$ to $\gamma = 1.92$. A value $\gamma \leq 1$ means the plan pass. In this figure, green pixels passed the gamma analysis and red pixels failed.

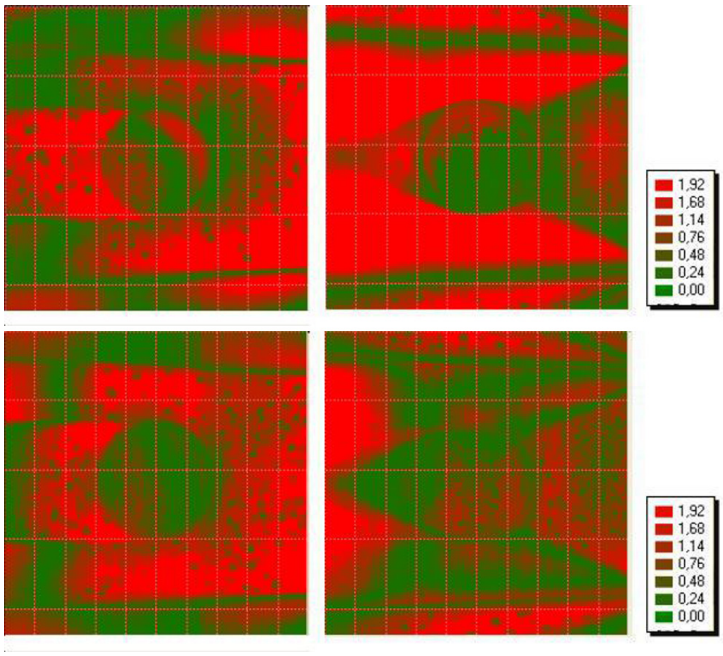

Figure 4.11: Gamma analysis results from FilmQA Pro for energy 10x (top row) and 10xFFF (bottom row) for AAA (left) and Accuros (left). Comparisons are for day 1 films. The color scale is seen to the right and runs from $\gamma = 0$ to $\gamma = 1.92$. A value $\gamma \leq 1$ means the plan pass. In this figure, green pixels passed the gamma analysis and red pixels failed.

4.1.5 Additional measurements in a homogeneous phantom

Figure 4.12 shows the film calibration curves from the film sheets. One curve is calibrated against the irradiated MU values and assuming a linear MU to Gy conversion, while the second is calibrated against measured dose in Gy from the farmer ionization chamber. Chamber dose measurements were on average 2.6% higher than its corresponding MU values (range 2.47-2.91%). This deviation was larger than the day-to-day difference between the three calibration film sets done in the study. Calibration of the films in VerA

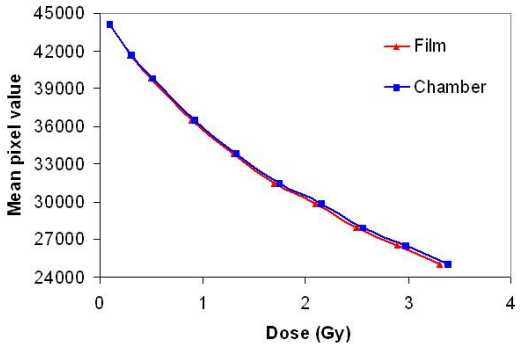

Figure 4.12: Calibration curve for water phantom films.

were done with respect to the ionization chamber measurements instead of MU values. The gamma acceptance at ΔD = 2% and Δd = 2 mm was 70% for energy 6x and 64% for energy 15x. Recalibration using the set MU values did not increase the acceptance rates. Figure 4.13 shows the AAA calculation, film measurement and gamma analysis for energy 6x. The color intensity scale is identical to VerA films in chapter 4.

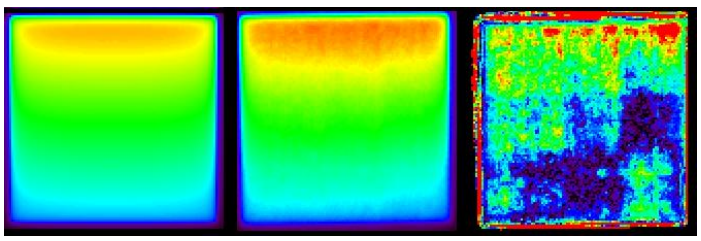

Figure 4.13: Film irradiated in water phantom with energy 6x and a wedge in place. From left: AAA calculation. response in the film, resulting gamma analysis.

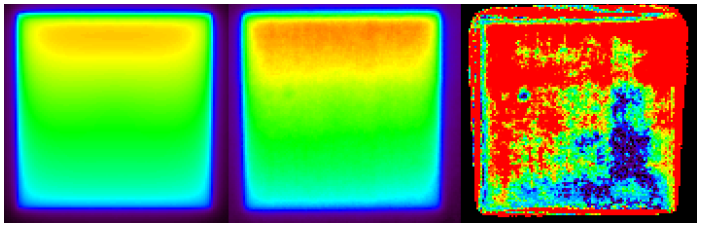

Figure 4.14: Film irradiated in water phantom with energy 15x and a wedge in place. From left: AAA calculation. response in the film, resulting gamma analysis.

4.2 Ionization chamber dosimetry in a lung phantom

For the comparison of calculated depth dose curves by AAA and Acuros in low density media, dose measurements in a lung phantom using a small ionization chamber was done as a comparison reference. The dose calculations were performed for the same lung phantom. The measured absorbed dose in each point in the lung phantom was found from

$$D = M \cdot N \cdot k \tag{4.2}$$

where M is the charge reading from the ionization chamber (in nC), N is the calibration factor for the ionization chamber (in Gy/nC) and k is the chamber specific correction factor for the beam quality found in IAEA TRS-398 table 6.III (42). This equation will produce absorbed dose in water for a calibrated ionization chamber. The equivalent depth dose measurements in the water phantom and the lung phantom was not found to differ by a constant C. The relationship between the two measured doses was found to increase with depth and energy, and was significantly higher for the smaller field size, seen in figure 4.15. In the figure each point represents the value D_{water} / D_{lung}. The relationship between the measured doses ranged from 1.13 for energy 6x, field size 10 x 10 cm at depth 1, to 2.57 for energy 10x, field size 3 x 3 cm in depth 4.

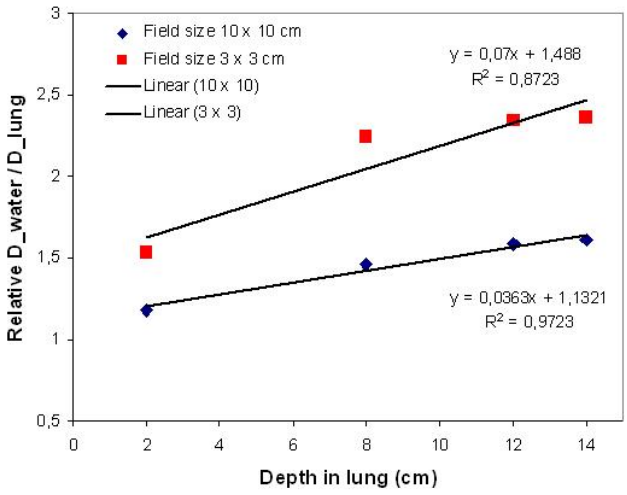

Figure 4.15: Measured dose in water phantom relative to measured dose in lung phantom (D_{water} / D_{lung}). Equivalent depths were used for the water measurements and this should result in constant relative measured doses.

Using equation 4.2 to calculate dose from the measured charge showed that the data from the lung phantom fit better with the calculations compared with measured dose from the water phantom. Due to the uncertainty in absolute dose determination, a relative depth dose comparison between AAA, Acuros and measurements in lung was done by normalizing the doses relative to the dose i measurement point 1. The non-normalized doses are listed in appendix A2. Figure 4.16 show the results as a function of lung depth for each energy and field size. It is seen that the difference between the two algorithms increase with depth in lung, higher energy and smaller field size. Looking at each field sizes separately, the results for field size 10 x 10 cm show a similar shape for all four

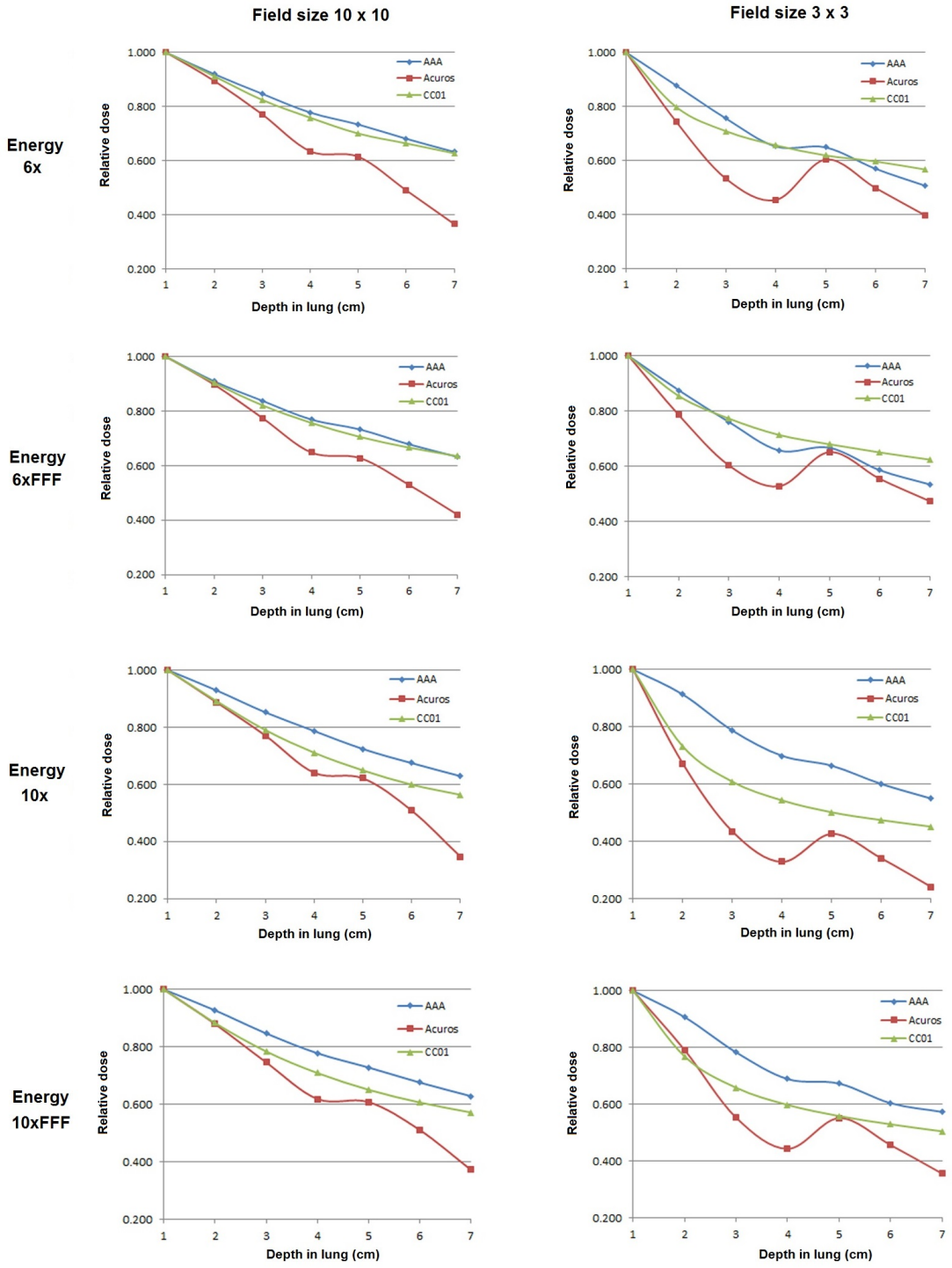

Figure 4.16: Measured and calculated dose in lung phantom for field size 10 x 10 cm (left column) and 3 x 3 cm (right column). Top row: energy 6x. Second row: energy 6xFFF. Third row: energy 10x. Bottom row: energy 10xFFF. In the figures the horizontal axis show the measurement points in the lung (after 5 cm of water), the vertical axis shows dose normalized to measurement point 1.

energies. The dose fall much more rapidly in Acuros calculations compared to AAA. The measured dose appear to agree better with AAA for the 6x and 6xFFF energies. For 10x

and 10xFFF measurements they agree with Acuros in the up to measurement point 3 and 2 before their slopes start decreasing and instead follow the trend of AAA.

For the 3 x 3 cm field the difference between AAA and Acuros calculations appear to increase with higher energy and decrease slightly when removing the flattening filter. Among the four energies tested, 10x shows the largest difference between the two algorithms. Measurements doses fit better with Acuros until measurement point 2 or 3 where their slopes decrease and follow the characteristics of AAA. 10x and 10xFFF show the best fit between measurements and Acuros calculations while 6xFFF fit better with AAA in all measured points. For the two energies 6x and 6xFFF measured doses are higher than both AAA and Acuros calculations from measurement point 4 and 3.

For all eight curves in figure 4.16 there is an increase in absorbed dose at measurement point 5 which changes the characteristics of the depth dose curve. To see how much the ionization chamber influenced the calculations depth dose curves was extracted from Eclipse for AAA and Acuros. Figure 4.17 shows how the calculation algorithms detect the presence of the ionization chamber in the CT series for a chamber in position 1 and 4 for energy 10x and field size 3 x 3 cm.

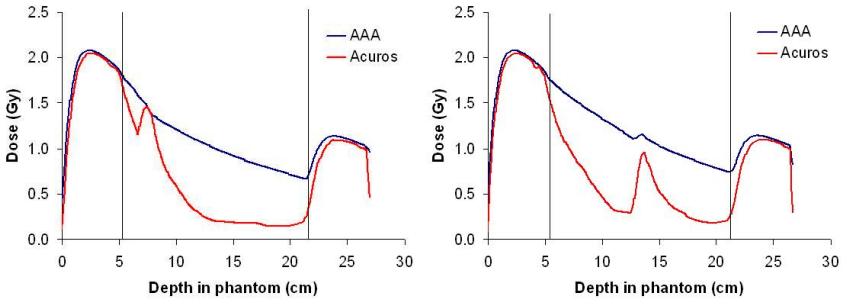

Figure 4.17: Depth dose curves for energy 10x, field size 3 x 3 cm and chamber in position 1 (left) and 4 (right). The blue curve shows AAA and the red curve shows Acuros calculations. The two vertical lines show the water-lung interface positions taken from the CT. Horizontal axis show phantom depth in cm, vertical axis show absolute dose in Gy.

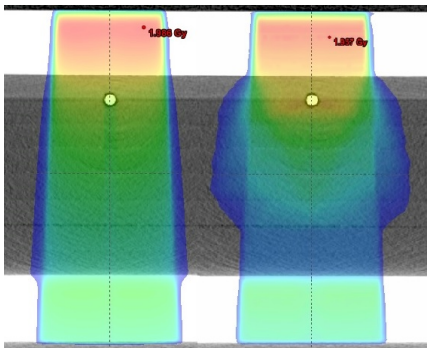

Figure 4.18: Dose calculation difference in light media between AAA (left) and Acuros (right). Calculation is done on the lung phantom for field size 10x10cm and energy 6x with the ionization chamber in position 1. Color scale runs from 0.3 Gy (dark blue) to 1.9 Gy (red).

Another view of the difference in calculated dose with depth is shown in figure 4.18 for a plane along the central axis in the the lung phantom with the ionization chamber in position 1. The sharper drop in absorbed dose with depth is observed for Acuros, along with a much wider lateral scatter contribution compared to AAA calculations. These 'wings' are present for both field sizes and all four energies, while being near absent in all AAA calculations, particularly for small fields.

4.3 Replanning of patients with Acuros

Four of the ten patients investigated received the 18 Gy x 3 regime while the remaining six received the 11 Gy x 5 regime. As the difference in total dose between the regimes was small; 1 Gy corresponding to less than 2%, comparisons were made without accounting for the difference in total dose or fractionation. After all plans were calculated with preset MU values corresponding to the original AAA plan, absolute maximum, minimum and mean doses were extracted for each volume. The plan difference was found by dividing the AAA dose with the Acuros dose. A positive dose difference corresponds to AAA overestimation.

Figure 4.19 shows the difference in percent for the GTV. It is observed that AAA generally estimates higher doses than Acuros. The minimum dose to the GTV exhibits the highest difference between the calculations with AAA estimating up to 17% higher dose. This corresponds to an absolute dose difference of about 9 Gy in patient 8. There is a 10% difference in GTV minimum dose for patient 6 and 10 which corresponds to an absolute dose difference of about 5 Gy.

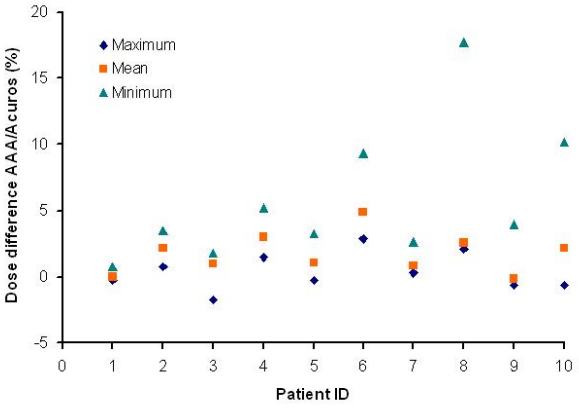

Figure 4.19: Percent difference in doses calculated by AAA and Acuros to the GTV for the ten investigated patients. Positive number refers to AAA overestimation.

Figure 4.20 shows the percentage difference in the PTV. The calculated volume maximum dose is within 3% for all patients where the majority are due to AAA estimating higher dose. Mean dose to PTV is also estimated higher by AAA, and four of the 10 plans show less than 3% mean dose difference. For the minimum dose the situation is similar for the GTV and only two of the ten plans show dose differences within 3%. This was patient 1 and 7. Compared to the other patients these two had the largest PTV volumes (86 and 89 cm^3). The positions of their tumors was in the right and left lung respectively. Two of the plans show a dose difference of 32% for the minimum dose to the PTV. These two

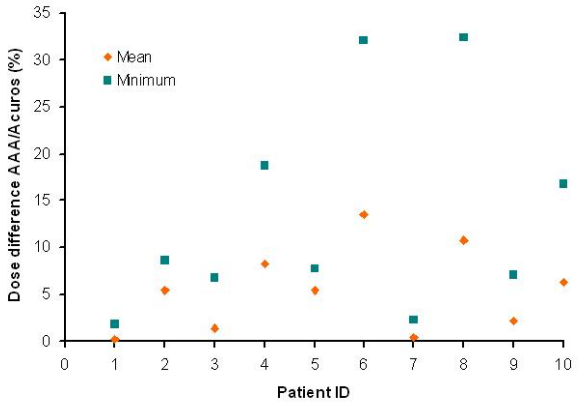

Figure 4.20: Percent difference in doses calculated by AAA and Acuros to the PTV for the ten investigated patients. Positive number refers to AAA overestimation.

patients (6 and 8) both had left side tumors. Their PTV volumes were small (12 and 16 cm^3). They also exhibited the largest difference in minimum dose to the GTV. The remaining six patients had minimum PTV dose differences of 7-19% .

The difference in calculated minimum dose to the PTV can be compared relative to different properties of the PTV. As the largest difference in calculated dose was observed for the smallest PTVs, the difference in calculated minimum dose to the PTV was compared to absolute PTV size (in cubic centimeters). This is shown in figure 4.21. As the size of the PTV is reduced the patients display a high AAA overestimation of minimum dose relative to Acuros.

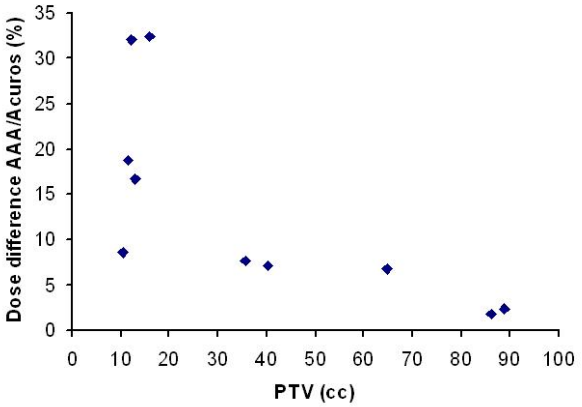

Figure 4.21: Difference in calculated minimum dose to the PTV for AAA and Acuros for the ten investigated patients relative to PTV size.

The PTV can be thought of as the sum of two parts; the GTV and PTV_{lung} which surrounds the GTV/tumor. The dose difference for minimum PTV dose was plotted against the size of PTV_{lung} relative to the PTV and this can be seen in figure 4.22. A relative PTV_{lung} close to 1 means that the tumor (GTV) constitutes only a small fraction of the PTV. For these patients the AAA overestimation of minimum dose relative to Acuros was much greater.

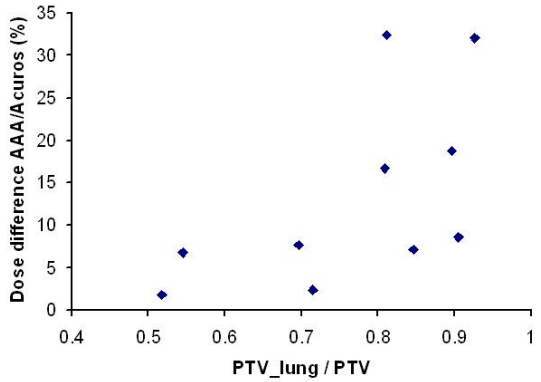

Figure 4.22: Difference in calculated minimum dose to the PTV as a function of PTV_{lung} relative to PTV.

Figure 4.23 shows the difference in calculated maximum dose to the medulla PRV. AAA calculates higher dose than Acuros to the medulla for all patients. Among those patients with differences above 3% only one (patient 1) had a calculated dose near the upper limit for the medulla. The plans calculated 18 Gy and the limit for this plan was 24 Gy as it was an 11 Gy x 5 fractionation. The other four patients all had maximum medulla doses of 6-8 Gy, well within the dose constraint of 18 Gy / 24 Gy.

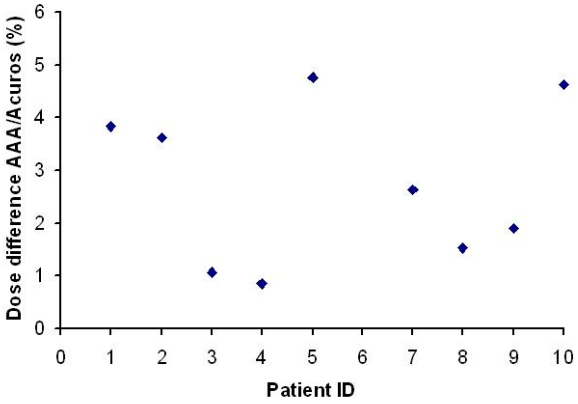

Figure 4.23: Percent difference in maximum dose to medulla PRV for the ten investigated patients calculated by AAA and Acuros. A positive dose difference refers to AAA overestimation.

Figure 4.24 shows the difference in mean dose to the lung containing the tumor (ipsilateral lung) and to the total lung volume (both lungs). AAA estimates higher mean dose in all but one plan (patient 2). All plans exhibits less than ± 2% mean dose differences in lung except for patient 8 who shows a mean dose difference of 3%.

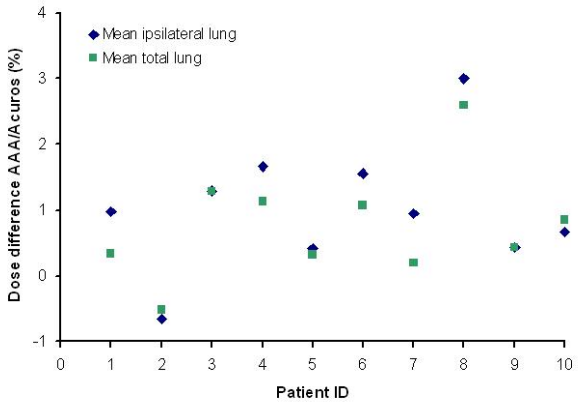

Figure 4.24: Percent difference in mean dose to ipsilateral and total lung calculated by AAA and Acuros for the ten investigated patients. A positive dose difference refers to AAA overestimation.

Figure 4.25 shows the results for maximum and mean doses to the thoracic wall. In this volume overestimation by Acuros is seen in many patients for the first time. This is observed for the maximum dose to the thoracic wall in seven of the ten patients, although most differences are less than 2%. For the mean dose AAA estimates slightly higher than Acuros for all patients, up to 2.5 %. As patient 8 exhibited large differences in calculated

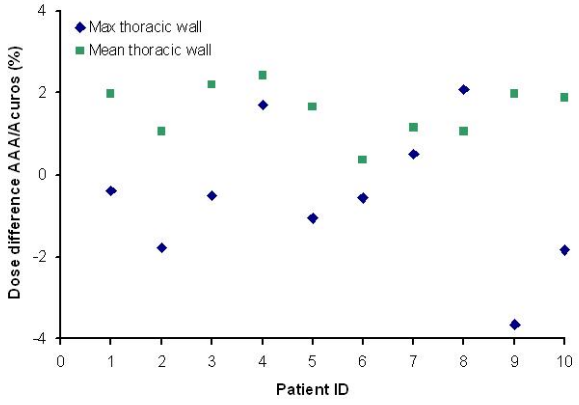

Figure 4.25: Percent difference in maximum and mean dose to the thoracic wall calculated by AAA and Acuros for the ten investigated patients. A positive dose difference refers to AAA overestimation.

dose for the PTV_{lung} for AAA and Acuros, a plan sum was created to view the absolute difference in dose in a plane through the PTV_{lung}. Dose calculated by Acuros was subtracted from AAA and the resulting plan sum for an area close to the tumor can be seen in figure 4.26. The sagittal plane chosen for the figure is in the area having the highest absolute dose difference and is located 6 mm medial to the periphery of the tumor. In the figure it is seen that in addition to AAA overestimation of dose to PTV_{lung} and areas surrounding it, Acuros reports a higher dose relative to AAA by about 6 Gy in areas 2 cm superior and inferior to the tumor (measured from the tumor center to the center of the blue area). Inspection of the plan sums for all ten patients showed that Acuros reports

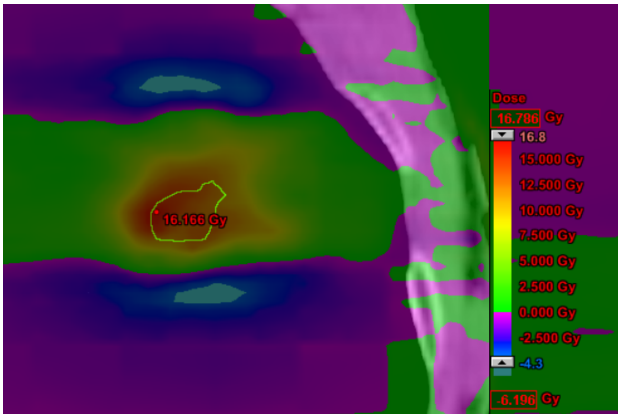

Figure 4.26: Acuros dose distribution subtracted from the AAA dose distribution resulting in the absolute dose difference in a plane through the PTV for patient 8. The patient is viewed in the sagittal plane. The margin for the PTV is drawn in green and part of the thoracic wall is seen to the right of the PTV. The color scale to the right is in absolute dose. A negative dose (blue) means that Acuros estimates a higher dose compared to AAA.

higher dose in this area for all patients.

A profile through the PTV_{lung} and the two areas of higher Acuros dose estimation for patient 8 is seen in figure 4.27. In this figure, the lower dose to PTV_{lung} is seen as well as the sharper fall in dose compared to AAA near the central axis. As the field edge is approached (around position 1.5 cm) the AAA estimated dose falls much faster than the Acuros estimated dose. This is similar to what was observed for the lung phantom in figure 4.18.

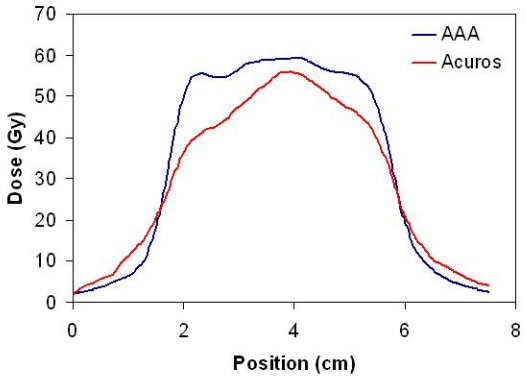

Figure 4.27: Profile through PTV_{lung} for patient 8. Position 4 cm corresponds with the center of the tumor. A sharper fall of the Acuros estimated dose is seen inside the PTV area (position 2-5 cm) while a sharper fall of the AAA estimated dose outside the PTV in the field penumbra.

VMAT plans require much more time to calculate compared to static fields. To reduce time spent many centers end up splitting the field calculations between several computer units. The average time required to calculate the stereotactic plans were noted for comparisons. The calculation time did not differ significantly between each patient plan. The ten AAA plans calculated using a 2.5mm grid size required 11-12 minutes of calculation

time when done by a single computer. This time was reduced to about 2-3 minutes when splitting the workload between many computer units. The corresponding Acuros calculations required 3-4 minutes per plan when calculated on a single computer as a plan sum. If the resolution of the dose map was changed to 1.0 mm grid size AAA calculations required approximately 80 minutes of calculation when done on one computer unit. Identical Acuros calculations still required just 3-4 minutes for the plan sum.

When evaluating a VMAT plan for clinical use, it is investigated as to whether it fulfills the required dose constraints on target volumes and risk volumes. The volume doses from the Acuros plans were extracted and compared to the clinically approved AAA plans. Four dose constraints were investigated: Thoracic wall, contralateral lung, total lung and PTV coverage. The first three are important risk organs and PTV coverage is related to the treatment prescription.

For the risk organs both algorithms produced almost identical results and failure to conform happened simultaneously in both algorithms. Patient 1, 5 and 9 failed the criterion $V_{30Gy} \leq 30$ cm^3 for thoracic wall. All plans passed the criterion $V_{5Gy} \leq 26\%$ for contralateral lung with minimal algorithm differences. For the total lung volume, patient 1, 3 and 9 failed the criterion $V_{20Gy} \leq 5\%$. However, patient 1 was close to passing (6% in both algorithms) and patient 3 and 9 had undergone lobectomies of the contralateral lung which affects the volume for the total lung and therefore the volume dose.

The target dose prescription for the stereotactic plans is defined such that 95% of the PTV should receive at least 100% of the prescribed dose. All ten patient plans failed this criterion in the Acuros plans, while the AAA plans all fulfilled this criterion. Patient 1 and 7, whose plans performed best with respect to minimum dose to the PTV, were within 1,2% of fulfilling this criterion for the Acuros plans. The other eight patient plans had 95% volume doses of 79-97% of prescribed dose as seen in figure 4.28.

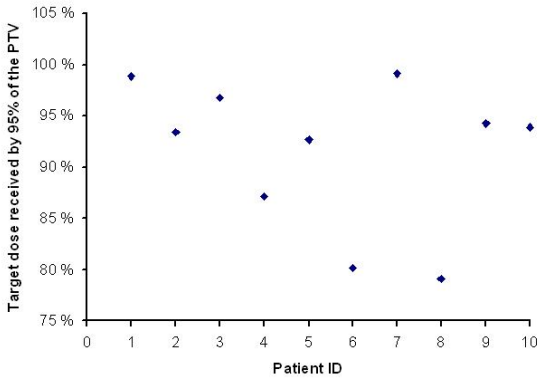

Figure 4.28: Dose which covers 95% of the PTV for the Acuros plans. Horizontal axis shows patient ID, vertical axis shows dose in percent relative to the prescribed dose. Prescribed dose was 54 or 55 Gy for the patient plans.

A visual display of the difference in PTV coverage is shown in figure 4.29 for patient 6, who has a PTV where 100% of the dose covers 80.1 % of the volume.

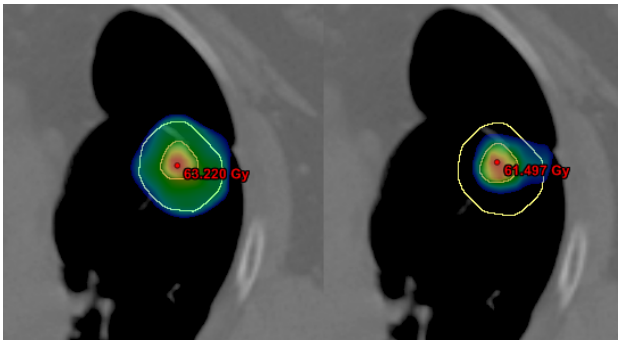

Figure 4.29: A visual display of the high dose cover to the PTV for patient 6 who displayed a 32% difference in minimum PTV dose. The left image shows the AAA dose distribution and the right image shows the Acuros dose distribution. The color scale starts at 54 Gy = 100% of prescribed dose (blue) and go to maximum PTV dose (red). The contour of the GTV and PTV is shown in the figure. It is observed that large parts of the PTV is not covered by the prescribed dose based on the Acuros calculation.

4.3.1 Delta4 verification

The results from the Delta4 verification is shown in table 4.4. All investigated plans passed the gamma analysis. Those points which did not pass the gamma analysis were all located in the low dose area and all investigated plans would have been approved for clinical use.

Table 4.4: Results from Delta4 verification of AAA and Acuros plans for three patients. Each plan had two fields (partial arcs) which were investigated separately. Approval is based on gamma analysis where the requirement for the plan to pass is 95%.

Patient	Percentage of points passing the gamma analysis			
	AAA field 1	AAA field 2	Acuros field 1	Acuros field 2
4	100	99.0	100	98.5
6	100	98.1	99.2	98.2
9	99.6	99.6	98.2	99.6

Chapter 5

Discussion

5.1 Film dosimetry in a lung phantom

5.1.1 Angular and energy dependency in the film

Angular independency is important as calibration and phantom measurements are done for beams with different incident angles. Inspection of film response for the same dose delivered from various directions indicate no angular dependency which need to be accounted for. The film's independence of energy was also confirmed.

The range of the mean pixel values for the different measurement points was inspected and were found to generally be within ±200 (of about 35 000) from the reference for all measured films. Perpendicular angles had the closest fit to the reference. This is consistent with the standard deviation being half relative to the parallel angles when extracting the mean pixel value in VerA. The first data set for parallel angles showed some mean pixel values deviating ±1500 from the reference. Every other point measured high and low and and no symmetry was observed. For this reason a new set of films were irradiated.

The second data set showed a fit with the reference within ±200 for all points and this data set was used in place of the first data set. The reference angle however produced a lower mean pixel value which affected the calculations of adjusted pixel values. They ended up having a larger deviation between each other than the mean pixel values. Comparing all the adjusted pixel values for angles irradiated parallel and perpendicular to the film plane, whose pixel values after adjustment should be the same, also showed that most points were within ± 200 of the other points. There were three outliers; the low parallel reference angle and and both measurement point laying furthest away from the reference.

The low response in the parallel reference angle could be due to a variation in output from the linac, a variation of the response in the scanner or error in the measurement setup. As the three points located next to this show almost identical response, the deviation in the parallel reference angle can safely be ignored in the comparison. The two other outlier points are thought to be affected by the low response in the reference angle and they are also ignored. The absolute difference between the remaining points; 300 of about 35 000, is considered to have little effect on the measured dose. The test of energy dependence show smaller deviations in pixel value than angular dependence, all mean pixel

values and adjusted pixel values were within ±100. The difference in response for each energy was much less than for the angular response. This is reasonable as there was an actual change in geometry for the angular measurements which introduces uncertainties. The linac is carefully calibrated to give 1 Gy for 100 MU independent of energy and this is validated continuously.

As VerA provides a standard deviation for the pixel value collected in the film, the procedure for IMRT film verification suggested a maximum standard deviation of 200 (pixel value) for a calibration film point dose. The maximum observed in this study for the collected mean pixel values was 173, which is well within the suggested limit. The response in the film appears to be independent of the angle of the beam. This is in agreement with previous versions of GafChromic films and manufacturer specifications. The calibration curve based on irradiation in the RW3 phantom can therefore be applied to the lung phantom film analysis.

5.1.2 Film analysis in VerA

The measurements of absolute dose in a lung phantom using radiochromic film did not produce results usable for comparing the algorithms AAA and Acuros, nor did it pass a gamma analysis for the calculated plans. This is despite the fact that radiochromic film has been used successfully by others to compare the algorithms in a heterogeneous phantom (23) (24).

Construction of the calibration curve was successful. Using the fourth degree polynomial function resulted in a very good fit to the measured points. The different sets of calibration films produced almost identical mean pixel values when collected in VerA. As the curve displayed similar properties as calibration curves used successfully by Kuttner (22) and Saur and Frengen (43) there was no reason to reject its validity.

The first inspection of the gamma maps for the film to dose map comparisons shows a larger number of rejected pixels compared to approved pixels. This was later confirmed by the percentage of gamma approved pixels, which was less than 50% for all maps. It was not possible to reproduce the results obtained from the first set of irradiations. Adjusting the gamma criteria beyond 5% / 5 mm did not result in significantly more approved points, meaning that response in the film is nowhere near the accuracy that is required in a clinical setting. Based on these results conclusions cannot be drawn for validating either AAA or Acuros here. Few clear trends or patterns were observed between the different energies, algorithms and irradiation days. For many of the comparisons it appears as the tumor and surrounding area has the most approved pixels for both algorithms. As the tumor is water equivalent, the two algorithms are expected to perform similarly. This is not observed as different areas of the tumor fails the gamma criterion for AAA and Acuros calculations when they are compared to the same film.

Many comparisons seem to favor AAA in what could be described as the PTV region (lung material close to the tumor). The opposite has been found in both measurements and Monte Carlo simulations (26), (32), (35), (36).

The sharp diagonal line of approved points present in the gamma maps from Acuros-to-film comparisons is an interesting visual effect. It is visible in gamma maps for all four energies, both irradiation days and also in the Acuros dose distributions exported from Eclipse. By inspecting the raw Acuros dose distribution it is clear that this line is due to the sharp drop in absorbed dose as the beam travels through the lung medium. This results in a large dose gradient which easier fulfills the distance to agreement criterion in the gamma analysis leading to more approved points relative to other parts of the phantom. The dose falls off much slower for AAA and the dose gradient is not seen.

Film dosimetry in a heterogeneous phantom has been successfully done in the past. Hoffman et al (32) investigated Acuros and AAA in a thorax phantom using film and found Acuros to be superior based on a 95% or better gamma acceptance in the majority of investigated plans. Although they used a higher gamma passing criterion and an older type film their study show that film measurements in heterogeneous phantoms can be done. The application of EBT3 film using the same protocol as EBT2 and EBT film has also be validated ((37), (38)). The department protocol for film IMRT verification has been validated from six years of successful use with EBT and EBT2 films for field sizes up to 16 x 16 cm^2.

Possible reasons for conflicting results using film includes the irradiation environment (phantom), the film itself, and the processing of the film post irraditation. The phantom had to be disassembled for the insertion of each film. It proved difficult to control the position of the film in the phantom on the millimeter level which may be necessary to observe a difference between the algorithms. This is also critical for placing the measured and calculated dose map correctly relative to each other for the gamma analysis. The lung material surrounding the film in the phantom is has a density very different from the film (0.04 vs 1.35 g/cm^3). To try and account for this the planning CT was done with a film sheet in place. The CT value for the lung was -960 HU while the film sheet measured at -710 HU. Water is defined as 0 HU and the film was then regarded as having minimal influence. Only one batch of film was tested, and batch-to-batch variations may occur. Testing a different film batch could have eliminated the film as a possible cause of inconsistent measurements.

The factor thought to affect the results the most was the equipment used and method for processing the response in the film. Aging of the detection components in the scanner was a real possibility. This would theoretically affect the periphery pixels in the film more due to a gradual change in the lateral response of the scanner. Mathot et al (33) reports lower gamma passing rates using EBT3 film but it is not specified the range of these. They also report a changing lateral response in the scanner. A test of the lateral response in this scanner (presented in appendix A3) revealed a non-symmetric and longitudinal-dependent effect on measured pixel value. The consistent results achieved from the calibration films supports the suspicion that this scanner is not reliable to accurately digitalize larger fields, which is also suggested by Ashland (19). A 10 x 10 cm^2 field in a water equivalent phantom showed somewhat better but from acceptable results. Any upper limit for the size of the field used for film irradiations in this scanner will have to be investigated further.

5.1.3 Film analysis in FilmQA Pro

After validation of plans in both a heterogeneous and homogeneous phantom using VerA failed, an alternative software was tested. Overall higher gamma passing rates were found but they were not high enough to approve any plans.

Gamma maps produced by FilmQA Pro are in many ways different than gamma maps from VerA. More tumor pixels are approved in FilmQA Pro included energy 10xFFF where VerA rejected all tumor pixels. The opposite is true for the two flattened energies where Acuros comparisons fail behind the tumor but are passed in VerA. The reason for this is thought to be problems with the overlay of the Eclipse dose map on top of the film dose distribution. FilmQA Pro relies heavily on fiducial marks for accurate placement which was found to be difficult to use for the lung phantom films. Regardless of this, an overall higher gamma passing rate was observed for the same film scans analyzed in FilmQA Pro. The reason could be due to the calibration method removing scanner artifacts as suggested by Micke et al (45).

As seen for VerA gamma maps the diagonal lines from the dose gradient is visible in FilmQA Pro gamma maps. An additional visual effect is the appearance of a number of small circles. Since the same TIFF images are used here as was used in VerA, the dots are thought to appear due to processing of the gamma map in FilmQA Pro. The higher gamma passing rate in FilmQA Pro suggests that VerA may not be appropriate for analysis of radiochromic film using the current procedure and equipment. Based on the data FilmQA Pro cannot be used without further validation where one must address the topic of accurate overlay as well as the reason for the circles appearing. When the uncertainty from the overlay is reduced, results can more accurately determine whether FilmQA Pro is appropriate to analyze film measurements against calculated dose plans.

5.1.4 Additional measurements in a homogeneous phantom

Irradiation of large films in the RW3 phantom was done to find out of the lung phantom itself was the reason for the low gamma passing rates. The gamma acceptance rates found in a homogeneous phantom are higher compared to those acquired from the lung phantom, but are not high enough to pass in the clinic. The results suggest that using a homogeneous phantom might increase the gamma acceptance rate, but there are factors affecting the film measurements which are independent of phantom and processing software used.

5.2 Ionization chamber dosimetry in a lung phantom

An attempt at accurate measurements of absolute doses in a lung phantom using an ionization chamber was not successful. An absolute comparison of measurements to calculations was therefore dropped in favor of a relative comparison.

The measured dose in the lung phantom was lower than the equivalent measurement in the water phantom for all comparable measurement points. From the setup outlined in section 3.3.2 the relationship between them were expected to be constant and closer to unity. The validity of the absolute dose measured in the lung phantom was therefore

questioned. It was decided to normalized the data relative to the first measurement point to avoid having to refer to the uncertain absolute dose. The non-normalized depth dose curves followed the same trends and as the normalized curves for the measurements, AAA and Acuros calculations. Measured and calculated doses can be found in appendix A2.

The calculated and measured relative depth dose curves for the 10 x 10 cm field size has a similar shape independent of energy or flattening filter presence. For the 3 x 3 cm field size the curve shapes are different relative to each other for the different energies. In general for all curves there is an energy dependence in which absorbed dose is slightly lower at a given depth for an increase in beam energy. Comparing this to the depth dose curves in water the opposite happens as the absorbed dose is higher for an increase in beam energy at a given depth beyond D_{max}. The absorbed dose is also lower for the flattened energy relative to the corresponding unflattened (FFF) energy. This is expected as the fluence of photons is higher for filter free beams at a given depth along the central axis, and the energy spectrum of the FFF beam is softer resulting in higher attenuation. All these energy dependences were seen for both AAA, Acuros and measurements. The shapes of the depth dose curves for the two calculations and the measurements relative to each other show that the differences increase with energy. Comparing the ionization measurements with the calculations, they overall agree better with AAA for the 10 x 10 cm field size and with Acuros for the 3 x 3 field size.

The local maximum observed in all calculated depth dose curves at measurement point 5 in the lung is most likely due to the presence of the ionization chamber. As the dose calculation is done on CT images with the ionization chamber present, the density difference between the ionization chamber and lung media will result in local dose buildup. At depth positions 1-4 this contribution is small compared to the dose deposition resulting from the upstream photon fluence and is therefore not visible in the figure. At depth position 6 and 7 the effect is also small due to the backscatter contribution from the bottom RW3 plates. The dose buildup due to the chamber is especially prominent in the Acuros calculations as the algorithm handle density variations differently, but is also observed in AAA calculations.

There are uncertainties in both calculated and measured doses. For the calculated doses one influencing factor is how the ionization chamber is presented in the CT series. As parts of the chamber contained steel electrodes which needed manual material assignment for Acuros calculations, the entire chamber volume was contoured and set equal to PMMA material. The choice of PMMA was based on a material having similar properties of the majority of the ionization chamber. The extent of the chamber was drawn for each CT series separately and the volumes could differ for each measurement point due to CT artifacts or free hand drawing uncertainties. A larger chamber volume in one CT would increase the calculated absorbed dose in that measurement point. This issue was further complicated by hidden high density pixels throughout the CT which required adjustment of margins.

It is suspected that the lower measured dose in the lung are due to a lack of build up cap used for the ionization chamber. The measurements are then performed in the buildup region where charged particle equilibrium is not established and the Bragg-Gray criterion

of no particle ending its path is not fulfilled.. A suitable buildup cap for this particular chamber was not available to attempt a new set of measurements.

The uncertainty in the measured dose arises from the question of whether the measurement setup can be used to determine absorbed dose in the heterogeneous phantom. No published results from a similar measurement protocol were found. As the stopping power of the medium was not known, equivalent measurements to water was done assuming a relatively constant ratio of scattering properties between lung and water for all measured depths. This would have resulted in a constant relationship between dose in water and dose in lung, which was later found to increase with depth, energy and for the smaller field size. Further investigations of dose calculation for inhomogeneous media revealed that the scattering properties cannot be assumed to have this constant relationship. The ionization chamber measurements in the lung phantom can therefore not be used to determine absolute dose with the accuracy required to make algorithm comparisons. For this particular phantom the scattering properties or the stopping power have to be found for the styrofoam, or a different type of detector will have to be utilized.

Investigating the phantom depth dose curve from calculations alone can be done independent of the measurements. The characteristics of the calculated depth dose curves shown in figure 4.17 support previous findings that AAA and Acuros show few differences in water but deviate in low density media. The calculated depth dose curves for AAA and Acuros correspond to calculated depth dose curves in low density media for the two algorithms found by Bush et al (26) where Acuros showed a much sharper fall in low density media, and a higher energy and a lower field size increased the calculation differences. Bush presents calculated depth dose curves for densities slightly higher (0.1 g/cc) and lower (0.01 g/cc) than the material investigated here (0.04 g/cc). As would be expected the calculation differences found here fall between those found by Bush for light lung and air.

Similarly, Fogliata et al (29) found that in low density media AAA and Monte Carlo calculations differed. As Acuros has shown to perform close to Monte Carlo simulations in low density media (11) (27), the trend in Fogliata's findings can be compared to those found here when Acuros and Monte Carlo are connected.

5.3 Replanning of patients with Acuros

Comparisons of stereotactic treatment plans for lung cancer patients calculated using AAA and Acuros show that the largest calculated dose differences occur in heterogeneous areas, particularly in the lung near the tumor and in the medulla. For the majority of plans and volumes investigated AAA overestimates the dose relative to Acuros.

Among the investigated volumes the target volumes GTV and PTV show the largest overall dose differences, and this is mainly in the minimum dose to the volume. Calculated maximum and mean doses in the GTV differ only by a few percent, and both AAA and Acuros calculate higher volume doses relative to each other at different points in the investigated patients. This suggests that there is no superior algorithm for calculations

of the maximum tumor dose. This is in accordance with Hoffman et al (32) and Fogliata (30) who found no significant differences between the two algorithms in water. The GTV is considered water equivalent as it by definition only includes the soft tissue tumor. The same is seen in the lung phantom used for the ionization measurements earlier where the difference in calculated dose to the bottom RW3 plates was minimal for AAA and Acuros in figure 4.17.

The voxels receiving the minimum dose in the GTV should be located in the periphery of the tumor where there will be a high dose combined with a density gradient (diffuse water-lung interface in the tumor periphery). This situation is one where AAA and Acuros have shown different behaviors in experiments. Assuming the PTV prescription is fulfilled, minimum dose to GTV is of less clinical relevance as the target dose is prescribed to the PTV.

The PTV is a heterogeneous volume as it includes the water equivalent tumor (GTV) and also less dense lung tissue (PTV_{lung}). Higher dose differences are observed here and AAA overestimates the dose relative to Acuros for all patients and in all dose categories (maximum, mininum and mean). The maximum dose in the PTV will not be discussed here as it is identical to the maximum dose for the GTV. The largest calculation dose difference found in the PTV is for calculation of minimum dose. In the most extreme case, Acuros estimates a dose 16 Gy lower than AAA. The difference in calculated dose was found to be dependent on the properties of the investigated volume. A correlation between PTV volume and calculated dose difference was found where a small (¡ 20 cc) PTV volume results in the highest difference in calculated minimum PTV dose. This absolute volume does not take into account the size of the tumor and how much of the PTV that consist of lung tissue. The largest deviations between algorithms were found for a PTV of about 10 cm^3 which is the lower limit used for PTV size in stereotactic plans. For those patients the GTV volume was very small (about 1-2 cm^3) so the PTV consists mostly of lung tissue. This suggests a correlation between PTV_{lung} and calculation deviations. This was found after plotting PTV_{lung}/PTV against the percent dose difference for the minimum PTV dose.

In both PTV volume comparisons there is a large spread in percent dose differences seen for the small PTV or large PTV_{lung}. Patient 2 had a similar tumor and PTV volume as patient 6 and 8 but the difference in calculated dose was much less (8% vs 32%). Distance to the thoracic wall was proposed as a reason but the target volume was located a comparable distance away from the throacic wall for all three patients.

The lower reported doses to the PTV by Acuros fit well with the depth dose characteristics found from calculations on the lung phantom in section 4.2, where a much lower absorbed dose in light density media was seen. Tumors completely surrounded by lung will be more affected than tumors located in the near proximity to soft tissue or bone (for this reason). The ten Acuros plans investigated will underdose the periphery of the PTV when calculated with the MU optimized by AAA. An exception to this was found for tumors located along the thoracic wall. If Acuros is assumed to be the most accurate calculation algorithm in low density media, this means that AAA greatly overestimates the dose to lung tissue. To be used clinically with the same dose constraints as for AAA, the Acuros plans will have to be reoptimized resulting in an increase in planned MUs.

This is in accordance with findings by Fogliata (28) for rapid arc (VMAT) treatment plans.

Results for the maximum dose to the medulla PRV show that AAA overestimate the dose relative to Acuros in all patients. The medulla PRV is also a heterogeneous volume as it consists of the soft tissue medulla spinalis surrounded by the vertebrae bones. The margin added to create the PRV will include small volumes of the higher density bone structures. The bone will absorbed more dose compared to the medulla due to its higher density. Acuros has shown to account for this better than AAA, and AAA will therefore report a higher dose downstream of the high density material (41). The effect is increased as the arc travel around the vertebra in VMAT treatments. In some of the patients the percentage difference between the algorithms is as high as 5%, but as the absolute dose is lower compared to other organs the absolute dose difference is not that much. None of the plans investigated showed medulla doses close to the allowed limit. The medulla differences are therefore not directly related to approval of these plans, but as the volume is surrounded by the vertebra bones this illustrates the calculation difference between the algorithms in areas of density differences. For other tumor groups the dose to the medulla is often the limiting factor when setting up a treatment plan and an accurate calculation of dose in this case is wanted.

As Acuros report that the medulla receive a lower dose than what was thought, one might be tempted to approve a plan calculated by AAA where the medulla dose constraint is exceeded. By arguing that because Acuros has showed high accuracy relative to Monte Carlo simulations, regarded as the closest model of reality, the actual dose received in the medulla will be lower than what AAA reports and the plan will therefore be safe to give to the patient. This is a risky assumption to make. Risk organ tolerance doses used in the clinic today are based on data from a large number of studies analyzing toxicity observed for a reported dose. A 'safe' treatment is one which has a low chance of serious side effects. Many of these studies are based on doses reported by simple planning algorithms such as pencil beam which lack heterogeneity corrections. The doses reported in these studies may be overestimated so that the true tolerance dose of an organ is lower than what is believed today. Assuming that Acuros is closer to the truth than AAA, all that has been found is a more accurate value of the risk organ tolerance dose.

The thoracic wall contain the ribs and supportive soft tissue. As mentioned above Acuros will estimate a higher dose to high density materials relative to AAA, and this is found in the majority of the patients for the maximum dose to this volume. For the mean dose, the difference in calculated dose between AAA and Acuros is low with AAA overestimating for all patients. This can be explained by the same mechanism as for the medulla, where AAA does not account for the high density in bones and will overestimate the dose further into the volume.

Results for mean dose to ipsilateral and total lung follow the general trend seen in this experiment and AAA overestimates the dose in all but one patient. There are no factors relating to the positioning of the tumor suggesting a reason why Acuros estimates higher dose for this case.

Together these findings support previous comparisons of clinical SBRT plans to the lung

calculated by AAA and Acuros. Tsuruta et al found a better match between Acuros and Monte Carlo than of AAA and Monte Carlo in lung SBRT patients (35). The largest PTV dose difference was found for the minimum dose to the PTV which is in accordance with the plans investigated here. The same was found by Kroon et al (40). Huang et al report comparable GTV doses and lower calculated doses to the PTV_{lung}, medulla and chest wall from Acuros compared to AAA (36), in accordance with what has been shown here. They found an overall higher dose to ipsilateral lung with Acuros which has not been shown here. Fogliata et al investigated non-SBRT VMAT plans and found a difference in mean doses to risk organs comparable to those found here.

Based on comparisons to Monte Carlo, it is thought that Acuros calculates a more realistic dose in heterogeneous media than AAA. The results obtained here indicate that for many lung patients, the dose given to heterogeneous volumes is likely different from the dose which the AAA treatment plan say is given to this volume. Treatment plans given to heterogeneous phantoms and measured by film dosimetry support this theory. Patient plans calculated on a heterogeneous phantom has been compared to film measurements by Kan et al (24), Hoffmann et al (32), where they found Acuros to be superior in the heterogeneous areas relative to film measurements.

The plan sum for all ten investigated patients showed the effect seen in figure **??**. They showed disk shaped areas 2 cm above and below the target volume where Acuros estimates a higher dose compared to AAA. 2 cm showed to be about the extent of the field limits for the arc suggesting that the disks are positioned in the penumbra region of the beam. The penumbra exists due to lateral scattering in the media which adds a dose contribution on the field edges. As Acuros model lateral scattering better, the penumbra will be wider in Acuros calculations. This is illustrated in figure 4.18 and again in figure 4.27. For the plan sum this results in a negative contribution in the penumbra area as Acuros reports more dose than AAA. In the figure, the beam travel straight into the page initially, and as the gantry rotates the beam move to enter from right to left before ending the gantry rotation with the beam coming out of the page. Together this creates a disk by superposition of the penumbra contributions from the different gantry angles. The highest difference in reported dose in this area was 6 Gy. The effect of the penumbra has to be taken into consideration when a field is given close to a risk organ. The results show that the dose to a risk organ positioned in the penumbra region of a beam traversing through low density media, may be underestimated by AAA. The heart, bronchi and brachial nerve are examples of such risk organs.

Performing a plan DVH comparison between AAA and Acuros for the patients supports the general findings in this study where the largest differences are in the minimum dose to the PTV, and the cumulative DVH is generally identical for risk organs except the medulla PRV. The low dose PTV region will require an increase in plan MUs to conform with the current dose prescription criterion. The time saved on the Acuros dose calculation is an advantage in the clinic and will provide benefits for VMAT if Acuros is calculated as a plan sum.

5.3.1 Delta4 verification

Verification of patient plans calculated by the Acuros algorithm was successful. Gamma analysis using the Delta4 phantom is possible for Acuros plans using the same passing criteria as used for AAA plan verifications.

The three plans chosen for verification were chosen randomly among the ten patients in this study. Verification of all ten patients was deemed unnecessary for the purpose of testing Acuros against Delta4 patient verifications. All of the investigated plans passed the gamma analysis and all fields were well within the criteria for passing. The AAA plans showed slightly different gamma passing rates compared to the original verification. The number of passed points in the original verification was between 97.4% and 99.6%. Patient 4 had the highest passing rates in the original and current AAA verification.

As a note, comparing the gamma passing rates for AAA and Acuros should not be done. The AAA plan and the Acuros plan are different as they have different dose distributions based on the same number of MUs. This test only validates the use of the Delta4 phantom for verification of a plan calculated by Acuros. This is necessary if Acuros were to be used clinically for calculating VMAT plans.

5.4 Suggestions for future work

As Acuros has been clinically validated it can be used as a general algorithm for radiotherapy, not just in lung cancers. Due to its superiority in high density media as well as low density media, there are situations where it would be beneficial to use Acuros over AAA. One example is for pelvic irradiations of a patient with a hip implant. The implant is made of high density metal and the dose may not be modeled well by AAA. Another example is for head and neck cancers. This area of the body contains both air volumes, in the form of the trachea, oropharyngeal area and the sinuses, and many small risk organs such as the parotid glands. Amalgam tooth fillings may also complicate dose planning. Investigating the behavior of Acuros for these situations should be done as the effect of high density materials has not been accounted for in this study.

Performing measurements of absolute dose in a low density media did not yield acceptable results. If measurements in phantom proving Acuros superiority over AAA is wanted, adjustments to the protocol described here is necessary. For measurements in a heterogeneous phantom thermo-luminescent diodes (TLDs) could be used. For the phantom described in section 3.2.2 TLDs could be inserted near the tumor-lung interface and a set of point doses could be obtained. The small size of the TLDs could result in useful measurements.

Full phantom film measurements were not successful but the calibration films provided useful results. Assuming the scanner uniformity is to blame, a smaller film sheet could be used. In this case one have to choose a region for the film. A suggestion based on the results found here is to place an 8 x 8 cm film sheet in the center of the phantom as before. Taping the film corners to the styrofoam block would help with knowing the center position of the film and would not interfere with measurements. This film would then

measure the dose received by areas corresponding to the GTV and PTV which are areas of interest. For the phantom described in section 3.3.1, instead of using the ionization chamber to measure point doses small film sheets like those used for calibration could be inserted between the styrofoam plates to measure the depth dose curve. The film would likely interfere less with measurements. In the CT study of the first lung phantom used the film was visible in the images but the CT number changed only by 250 HU relative to the lung material. For comparisons the CT number for the ionization chamber phantom changed was more than 3000 HU more than the surrounding lung for large parts of the chamber. Establishing a working film protocol is necessary before this is attempted. Due to time constraints none of these ideas were attempted in this study.

Before full clinical use of Acuros there are two points which need to be addressed. As described in section 2.4.2 Acuros uses material assignment based on HU conversion to density. CT numbers above ca 2800 HU require manual contouring of the pixels before material assignment. For all ten investigated patients there were a number of pixels in their CT scans which exceeded this limit. Some of them proved very difficult to locate as the CT ranger tool in the TPS could not detect them. A solution could be to plan the whole patient using high density segments, as suggested in the TPS manual. This is not the normal procedure at the time of this study and may require changes to work flow and department procedures. The second point is a further investigation of the behavior of the different energies. Although not looked at in this study, the calculated Acuros output factors for the energy 10xFFF deviated from measurements and AAA calculations. As this energy is preferred for stereotactic lung treatments this deviation and its effect on dose planning should be looked at.

Chapter 6

Conclusion

The use of the Acuros dose calculation algorithm in place of AAA is expected to improve the accuracy of radiotherapy treatment planning of lung tumors. In this study, a dosimetric evaluation of the properties of the calculation algorithms AAA and Acuros has been done. For simple, heterogeneous phantom geometries, absolute dose measurements were done using radiochromic film and ionization chambers. Results could not be produced with a high enough accuracy to perform plan gamma analyses. Relative comparisons of the depth dose curves calculated by the two algorithms show differences in low density media, in accordance with published findings.

For lung cancer patients treated with stereotactic radiotherapy using flattening filter free beams, AAA and Acuros plans calculated with fixed MUs result in different dose distributions. The largest calculation differences occur in the periphery of the PTV where, in the most extreme case, AAA will overestimate the dose by 16 Gy relative to calculations by Acuros. This overestimation increases for a small PTV, and for a PTV consisting mostly of lung tissue. Smaller differences in calculated doses were found for the heterogeneous risk organs, where AAA generally overestimates the volume dose. An exception is found for the maximum dose to the thoracic wall. The results obtained here support published dosimetric comparisons and clinical validations of AAA and Acuros for use in stereotactic radiotherapy of lung tumors.

Verification of Acuros calculated plans using the Delta4 phantom is possible. After the practical issue with high density CT pixels is resolved, it is recommended to implement Acuros in the routine treatment planning of lung tumors.

Bibliography

[1] Cancer in Norway 2013 - Cancer incidence, mortality, survival and prevalence in Norway. Oslo: Cancer Registry of Norway, 2015.

[2] Faglige anbefalinger ved ikke-småcellet lungecancer. Østerås: Norwegian Lung Cancer Group & the Quality Assurance in Radiation Therapy group; 2015.

[3] International Commision on Radiation Units and Meausurements. Fundamental Quantities and Units for Ionizing Radiation. Bethesda: International Commision on Radiation Units and Meausurements; 1998. ICRU Report 60.

[4] Ahnesjö A & Aspradakis MM. Dose calculations for external photon beams in radiotherapy. Phys. Med. Biol. 1999; 44(11): R99-R155. DOI: 10.1088/0031-9155/44/11/201.

[5] Mijnheer B, Bridier A, Garibaldi C, Torzsok K & Venselaar J. Monitor unit calculation for high energy photon beams - practical examples. ESTRO booklet #6. 1st ed. Brussels: European Society of Theraputic Radiotherapy and Oncology; 2001.

[6] International Commision on Radiation Units and Meausurements. Prescribing, Recording and Reporting Photon Beam Therapy. Bethesda: International Commision on Radiation Units and Meausurements; 1999. ICRU Report 62.

[7] Hurkmans CW, Cuijpers JP, Lagerwaard FJ, Widder J, van der Heide UA, Schuring D et al. Recommendations for implementing stereotactic radiotherapy in peripheral stage IA non-small cell lung cancer: report from the Quality Assurance Working Party of the randomised phase III ROSEL study. Radiation Oncology. 2009;4(1). DOI: 10.1186/1748-717X-4-1.

[8] Navarria P, Ascolese AM, Mancosu P, Alongi F, Clerici E, Tozzi A et al. Volumetric modulated arc therapy with flattening filter free (FFF) beams for stereotactic body radiation therapy (SBRT) in patients with medically inoperable early stage non small cell lung cancer (NSCLC). Radiotherapy and Oncology. 2013;107: 414-418. DOI: 10.1016/j.radonc.2013.04.016.

[9] Lagerwaard FJ, Verstegen NE, Haasbeek CJ, Slotman BJ, Paul MA, Smit EF et al. Outcomes of Stereotactic Ablative Radiotherapy in Patients With Potentially Operable Stage I Non-Small Cell Lung Cancer. Int J Radiation Oncol Biol Phys. 2012;83(1): 348-353. DOI: 10.1016/j.ijrobp.2011.06.2003.

[10] Sievienen J, Ulmer W & Kaissl W. AAA Photon Dose Calculation Model in Eclipse. Palo Alto: Varian Medical Systems; 2005. Report No: RAD 7170B.

[11] Failla GA, Wareing T, Archambault Y &Thompson S. Acuros XB advanced dose calculation for the Eclipse treatment planning system. Palo Alto: Varian Medical Systems; 2011. Report No: RAD 10156.

[12] Attix FH. Introduction to radiological physics and radiation dosimetry. New York: Wiley Interscience; 1986.

[13] Khan FM. The Physics of Radiation Therapy. 4.th ed. Baltimore: Lippincott Williams & Wilkins; 2010.

[14] Low DA, Harms WB, Mutic S & Purdy JA. A technique for the quantitative evaluation of dose distributions. Med Phys. 1998;25(5):656-61. DOI: 10.1118/1.598248

[15] Low DA & Dempsey JF. Evaluation of the gamma distribution comparison method. Med Phys. 2003;30(9): 2455-64. DOI: 10.1118/1.1598711

[16] Delta^{4PT} Getting Started. Uppsala: ScandiDos.

[17] Gafchromic EBT3 (brochure). Wayne: International Specialty Products; 2011.

[18] GafChromic EBT3 Scan Handling Guide. Wayne: Advanced Materials; 2012.

[19] Lewis DF. Using Radiochromic Film, Tips and Techniques (Power Point presentation). Wayne: International Specialty Products; 2010.

[20] Niroomand-Rad A, Blackwell CR, Cousey BM, Gall KP, Galvin JM, McLaughin WL et al. AAPM Report No. 63 Radiochromic Film Dosimetry Recommendations of AAPM Radiation Therapy Committee Task Group No. 55. Med Phys. 1998;25(11). DOI: 10.1118/1.598407.

[21] Mauring A. Radiochromic film for characterization of the radiation field: A protocol for the practical use of GafChromic EBT for dosimetric purposes in radiotherapy. Østerås: Norwegian Radiation Protection Authority; 2009. StrålevernRapport 2009:9.

[22] Kuttner, S. Evaluation of clinical procedures required before implementation of IMRT treatments delivered by dynamic MLC (master thesis). Umeå: UmeåUniversity; 2008.

[23] Paelinck L, Reynaert N, Thierens H, De Neve W & De Wagter W. Experimental verification of lung dose with radiochromic film: comparison with Monte Carlo simulations and commercially available treatment planning systems. Phys. Med. Biol. 2005;50(9): 2055-2069. DOI: 10.1088/0031-9155/50/9/009.

[24] Kan MW, Leung LH, So RW &Yu PK. Experimental verification of the Acuros XB and AAA dose calculation adjacent to heterogeneous media for IMRT and RapidArc of nasopharygeal carcinoma. Med Phys. 2013;40(3): 031714. DOI: 10.1118/1.479230.

[25] Poppinga D, Schoenfeldt AA, Doemer KJ, Blanck O, Harder D & Poppe B. A new correction method serving to eliminate the parabola effect of flatbed scanners used in radiochromic film dosimetry. Med Phys. 2014;41(2). 021707. DOI: 10.1118/1.4861098.

[26] Bush K, Gagne IM, Zavgorodni S, Ansbacher W & Beckham W. Dosimetric validation of Acuros XB with Monte Carlo methods for photon dose calculations. Med Phys. 2011;38(4): 2208-2221. DOI: 10.1118/1.3567146.

[27] Vassiliev ON, Warening TA, McGhee J, Failla G, Salehpour MR & Mourtada F. Validation of a new grid-based Boltzmann equation solver for dose calculation in radiotherapy with photon beams. Phys. Med. Biol. 2010;55(3): 581-598. DOI: 10.1088/0031-9155/55/3/002.

[28] Fogliata A, Nicolini G, Clivio A, Vanetti E % Cozzi L. Critical Appraisal of Acuros XB and Anisotropic Analytic Algorithm Dose Calculation in Advanced Non-Small-Cell Lung Cancer Treatments. Int J Radiation Oncol Biol Phys. 2012;85(5): 1587-1595. DOI: 10.1016/j.ijrobp.2011.10.078.

[29] Fogliata A, Vanetti E, Albers D, Brink C, Clivio A& Knöös T et al. On the dosimetric behaviour of dose calculation algorithms in the presence of simple geometric heterogeneities: comparison with Monte Carlo calculations. Phys. Med. Biol. 2007;52(5): 1363. DOI: 10.1088/0031-9155/52/5/011.

[30] Fogliata A, Nicolini G, Clivio A, Vanetti E, Pietro Mancosu& Cozzi L. Dosimetric validation of the Acuros XB Advanced Dose Calculation algorithm: fundamental characterization in water. Phys. Med. Biol. 2011;56(6): 1879. DOI:10.1088/0031-9155/56/6/022.

[31] User Manual Film QA Pro version 3.0.4864.35322 (2013). Wayne: Ashland. 2013.

[32] Hoffmann L, Jrgensen MK, Muren LP & Petersen JB. Clinical validation of the Acuros XB photon dose calculation algorithm, a grid-based Boltzmann equation solver. Acta Oncologica. 2012; 51(3): 376-385. DOI: 10.3109/0284186X.2011.629209.

[33] Mathot M, Sobczak S & Hoornaert M. Gafchromic film dosimetry: Four years experience using FilmQA Pro software and Epson flatbed scanners. Physica Medica. 2014;30(8): 871-877. DOI: 10.1016/j.ejmp.2014.06.043.

[34] Sorriaux J, Kacperek A, Rossomme S, Lee JA, Berrand D, Vynckier S et al. Evaluation of Gafchromic EBT3 films characteristics in therapy photon, electron and proton beams. Physica Medica. 2013;29(6): 599-606. DOI: 10.1016/j.ejmp.2012.10.001.

[35] Tsuruta Y, Nakata M, Nakamura M, Matsuo Y, Higashimura K, Monzen H et al. Dosimetric comparison of Acuros XB, AAA, and XVMC in stereotactic body radiotherapy for lung cancer. Med Phys. 2014;41(8): 081715.

[36] Huang B, Wu L, Lin P & Chen C. Dose calculation of Acuros XB and Anisotropic Analytical Algorithm in lung stereotactic body radiation therapy treatment with flattening filter free beams and the potential role of calculation grid size. Radiat. Oncol. 2013;10(1): 357. DOI: 10.1186/s13014-015-0357-0.

[37] Reinhardt S, Hillbrand M, Wilkens JJ & Assman W. Comparison of GafChromic EBT2 and EBT3 filems for clinical photon and proton beams. Med Phys. 2012;39(8): 5257-5262. DOI: 10.1118/4737890.

[38] Andrès C, Castillo A, Tortosa R, Alonso D & Barquero R. A comprehensive study of Gafchromic EBT2 radiochromic film, A comparison with EBT. Med Phys. 2010;37(12): 6271-6278. DOI: 10.1118/1.3512792.

[39] Benedict SH, Yenice KY, Followill D, Galvin JM, Hinson W, Kavanagh B et al. Stereotactic body radiation therapy: The report of AAPM Task Group 101. Med Phys. 2010;37(8): 4078-4101. DOI: 10.1118/1.3438081

[40] Kroon PS, Hol S & Essers M. Dosimetric accuracy and clinical quality of Acuros XB and AAA dose calculation algorithm for stereotactic and conventional lung volumetric modulated arc therapy plans. Radiat Oncol. 2013;8(1): 149. DOI: 10.1186/1748-717X-8-149.

[41] Lloyd SA & Ansbacher W. Evaluation of an analytical linear Boltzmann transport equation solver for high density inhomogeneities. Med Phys. 2013;40(1): 011707-1. DOI: 10.1118/1.4769419.

[42] Andreo P, Burns DT, Hohfield K, Kanai T, Laitano F et al. Absorbed dose determination in external beam radiotherapy: An international code of practice for dosimetry based on standards of absorbed dose to water. Vienna: International Atomic Energy Agency; 2000. IAEA Technical Report Series 398.

[43] Saur S & Frengen J. GafChromic EBT film dosimetry with flatbed CCD scanner: a novel background correction method and full dose uncertainty analysis. Medical physics. 2008; 35(7): 3094-3101. DOI: 10.1118/1.2938522.

[44] Mayles P & Williams P. Megavoltage Photom Beams. In: Mayles P, Nahum A, Rosenwald JC, editors. Handbook of Radiotherapy Physics: theory and practice. Boca Raton: CRC Press; 2007. p. 451-481.

[45] Micke A, Lewis DF & Yu X. Multichannel film dosimetry with nonuniformity correction. Med Phys. 2011;38(5): 2523-34. DOI: 10.1181/1.3576105.

Appendix A1

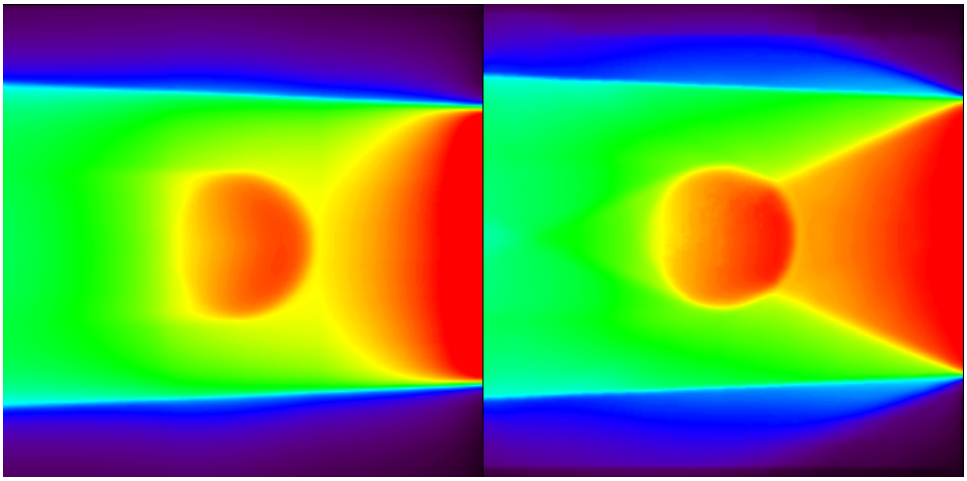

Figure A-1: Calculated dose maps for the lung phantom in section 3.2.2 for energy 6x. The left image shows AAA and the right image shows Acuros calculations. The color scale runs from 0 Gy (black) to 2.20 Gy (red).

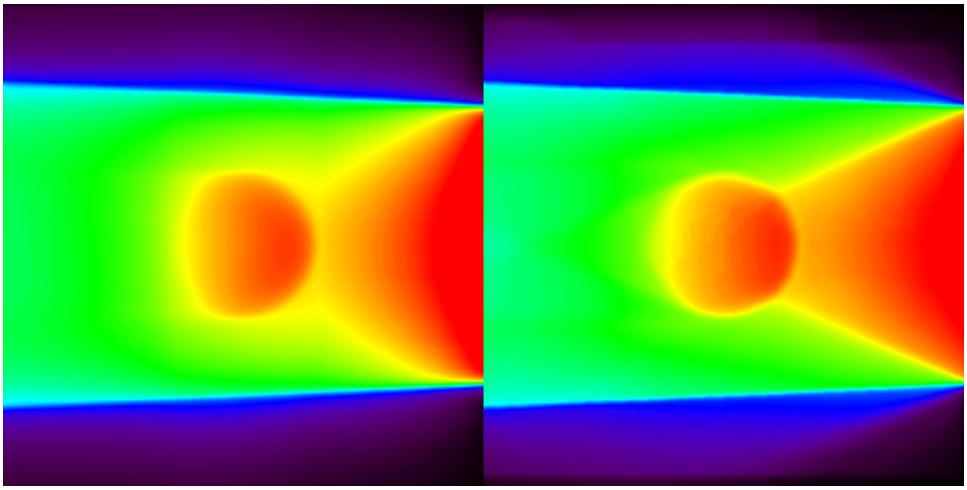

Figure A-2: Calculated dose maps for the lung phantom in section 3.2.2 for energy 6xFFF. The left image shows AAA and the right image shows Acuros calculations. The color scale runs from 0 Gy (black) to 2.20 Gy (red).

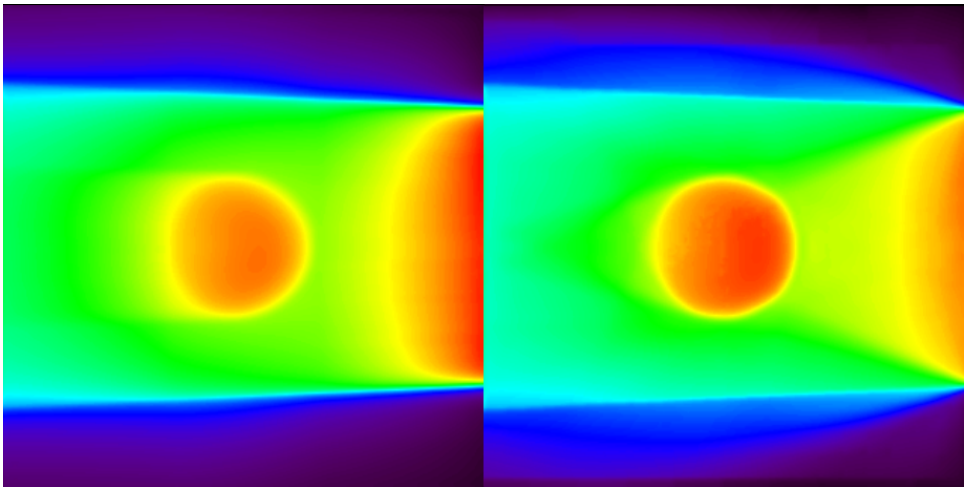

Figure A-3: Calculated dose maps for the lung phantom in section 3.2.2 for energy 10x. The left image shows AAA and the right image shows Acuros calculations. The color scale runs from 0 Gy (black) to 2.20 Gy (red).

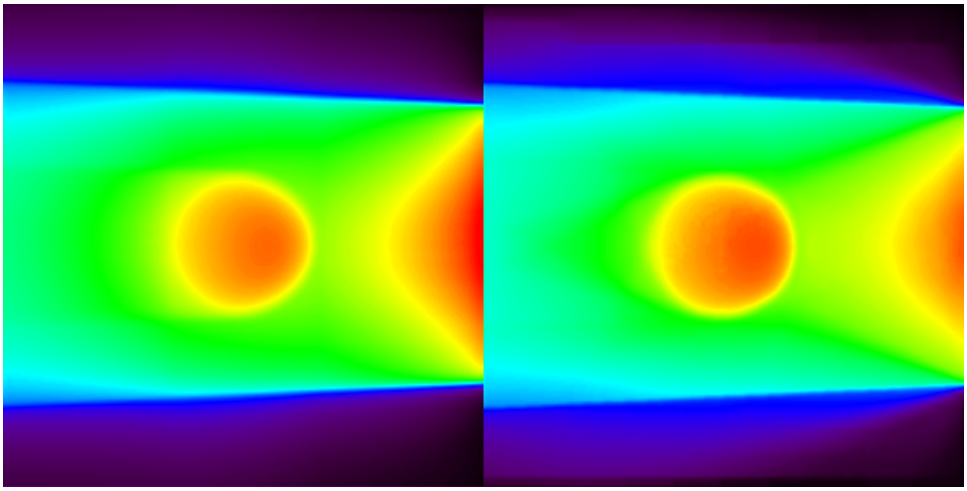

Figure A-4: Calculated dose maps for the lung phantom in section 3.2.2 for energy 10xFFF. The left image shows AAA and the right image shows Acuros calculations. The color scale runs from 0 Gy (black) to 2.20 Gy (red).

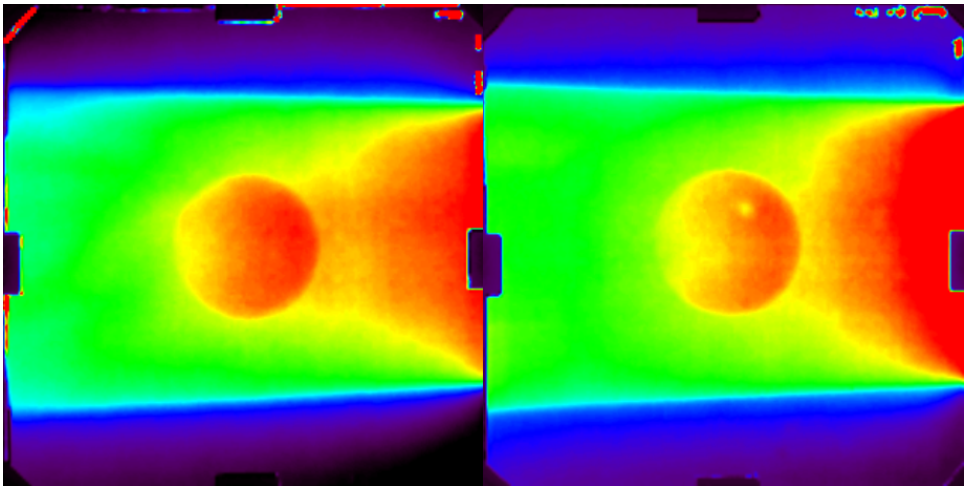

Figure A-5: Response in irradiated radiochromic films for energy 6x. The left image shows response from day 1 and the left image shows response from day 2. The color scale runs from 0 Gy (black) to 2.20 Gy (red).

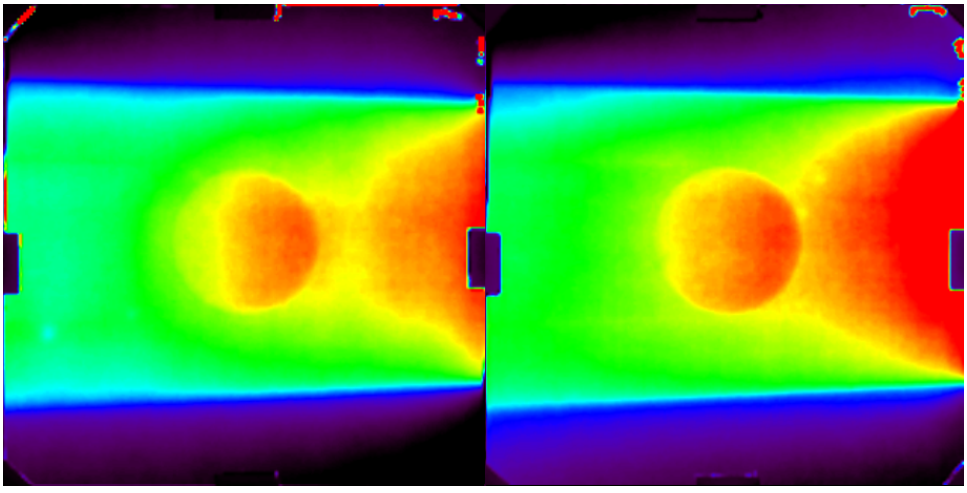

Figure A-6: Response in irradiated radiochromic films for energy 6xFFF. The left image shows response from day 1 and the left image shows response from day 2. The color scale runs from 0 Gy (black) to 2.20 Gy (red).

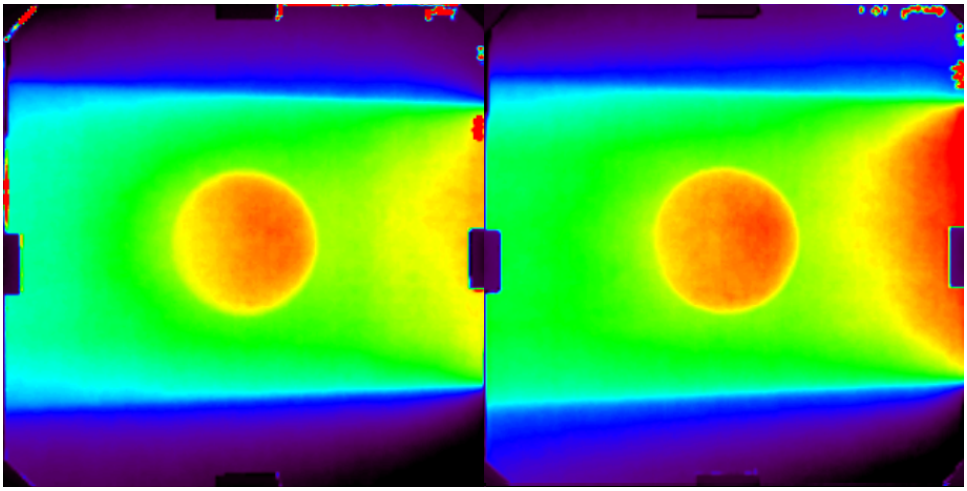

Figure A-7: Response in irradiated radiochromic films for energy 10x. The left image shows response from day 1 and the left image shows response from day 2. The color scale runs from 0 Gy (black) to 2.20 Gy (red).

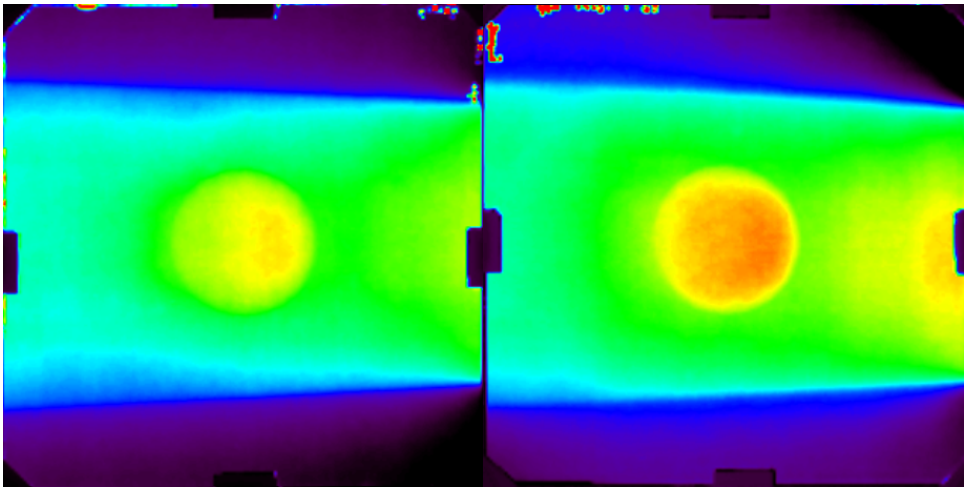

Figure A-8: Response in irradiated radiochromic films for energy 10xFFF. The left image shows response from day 1 and the left image shows response from day 2. The color scale runs from 0 Gy (black) to 2.20 Gy (red).

Appendix A2

Table A-1: Results from CC01 measurements in the lung phantom for field size 10 cm x 10 cm. Values listed are absolute doses as calculated from equation 4.2.

Measurement point	Dose (Gy) at energy 6x and field size 10 x 10		
	AAA	Acuros	CC01
1	1.402	1.449	1.370
2	1.290	1.297	1.250
3	1.188	1.118	1.130
4	1.091	0.920	1.040
5	1.029	0.891	0.960
6	0.955	0.711	0.910
7	0.887	0.530	0.860
Measurement point	Dose (Gy) at energy 6xFFF and field size 10 x 10		
	AAA	Acuros	CC01
1	1.406	1.426	1.367
2	1.278	1.279	1.235
3	1.177	1.103	1.122
4	1.081	0.924	1.034
5	1.030	0.895	0.964
6	0.954	0.756	0.911
7	0.889	0.600	0.868
Measurement point	Dose (Gy) at energy and 10x field size 10 x 10		
	AAA	Acuros	CC01
1	1.380	1.384	1.325
2	1.282	1.228	1.181
3	1.176	1.067	1.047
4	1.086	0.887	0.942
5	0.999	0.860	0.860
6	0.931	0.704	0.794
7	0.868	0.481	0.747
Measurement point	Dose (Gy) at energy 10xFFF and field size 10 x 10		
	AAA	Acuros	CC01
1	1.393	1.391	1.335
2	1.292	1.224	1.179
3	1.180	1.038	1.047
4	1.084	0.861	0.947
5	1.015	0.846	0.869
6	0.942	0.711	0.810
7	0.876	0.518	0.764

Table A-2: Results from CC01 measurements in the lung phantom for field size 3 cm x 3 cm. Values listed are absolute doses as calculated from equation 4.2.

Measurement point	Dose (Gy) at energy 6x and field size 3 x 3		
	AAA	Acuros	CC01
1	1.542	1.377	1.340
2	1.354	1.025	1.070
3	1.166	0.734	0.950
4	1.006	0.626	0.880
5	1.001	0.832	0.830
6	0.879	0.687	0.800
7	0.782	0.547	0.760
Measurement point	Dose (Gy) at energy 6xFFF and field size 3 x 3		
	AAA	Acuros	CC01
1	1.538	1.407	1.345
2	1.347	1.106	1.150
3	1.170	0.849	1.040
4	1.011	0.743	0.960
5	1.027	0.917	0.915
6	0.902	0.781	0.875
7	0.822	0.667	0.840
Measurement point	Dose (Gy) at energy 10x and field size 3 x 3		
	AAA	Acuros	CC01
1	1.442	1.317	1.104
2	1.317	0.885	0.808
3	1.135	0.573	0.672
4	1.008	0.433	0.600
5	0.958	0.562	0.554
6	0.866	0.449	0.524
7	0.793	0.318	0.499
Measurement point	Dose (Gy) at energy 10xFFF and field size 3 x 3		
	AAA	Acuros	CC01
1	1.39	1.184	1.172
2	1.261	0.937	0.901
3	1.089	0.655	0.772
4	0.958	0.525	0.701
5	0.936	0.653	0.655
6	0.840	0.541	0.621
7	0.797	0.422	0.592

Appendix A3

Scanner characterization

A characterization test of the scanner was done to investigate whether it was the cause of the bad results from the radiochromic film. In addition, some of the films were scanned using a second scanner and the resulting images were compared to the original scans.

Poppinga (25) analyzed their scanner to characterize the parabola effect by scanning a small film at multiple positions on the scanner glass. Characterizing the parabola effect for this scanner was attempted as a starting point, although inspection of the film images suggested the scanner response might not be symmetrical and likely contained a scan axis dependent component as well. If this test showed a clear parabola effect this could be accounted for in VerA using Poppinga's solution and might improve the recorded responses in the irradiated films.

A grid of five lateral and six scan axis positions covering the entire scanner glass surface was marked on the scanner. Two 4 x 4 cm calibration film were scanned in each of the thirty positions following the same scan protocol as before. The film sheets had been exposed to 50 MU and 330 MU allowing a test of dose dependence in the parabola. The scanner glass surrounding the film sheet was covered with thick paper sheets serving the same purpose as the cardboard frame used for phantom films (positioning and reduction of scattered light).

Background correction and median filtering was done in VerA and the mean pixel value was obtained from the center of the film in each position. Mean pixel values were plotted as a surface. Figure A-9 shows this plot for 50 MU. The results indicate a dose dependent parabolic effect across the scan surface, but it appears more extreme on one side and seem to depend on longitudinal position as well. The area of the scan surface used for the calibration films appear to have more homogeneous response. Poppinga showed the

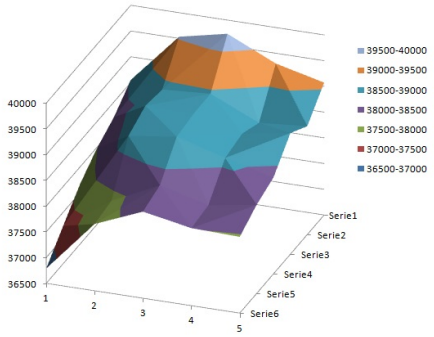

Figure A-9: Surface function showing mean pixel value as function of position on the scanner glass.

scanner response independent of longitudinal position. Taking the average mean pixel value along the longitudinal direction for each lateral position and converting this average pixel value to optical density using equation 3.1 produced one lateral response data set for 50 MU and one for 330 MU. A quadratic function fit to the data can be seen in figure A-10. As seen in the figure, the R^2 value the data points did not yield a perfect

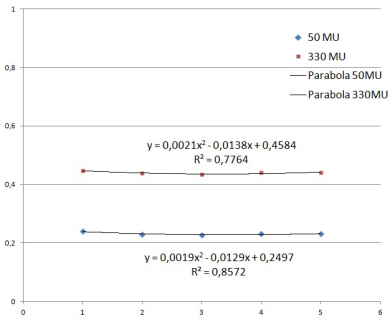

Figure A-10: Fitted quadratic function for lateral response in the scanner.

parabolic fit. The stronger response on the left side of the scanner visible in figure A-9 is visible in the function fit as the right side appears flatter. The scanner surface data suggests that the scanner has non-uniformities beyond the lateral effect and the correction term suggested by Poppinga would be difficult to implement. Further tests of the scanner response was therefore halted in favor of using multi channel correction for calibration.

A second Epson V750 Pro scanner was tested to compare the response between two Epson V750 Pro scanners. The second scanner was identical in model and year of purchase but had seen much less use compared to the previously investigated scanner. All phantom films from day 1 and 2 were scanned using the previous scan protocol. As these scans were taken one and two months after irradiation, a new calibration curve was constructed for each of the two film sets. The films were compared to AAA calculations via gamma analysis in VerA and FilmQA Pro. Results from the gamma analysis are found in table A-3.

Table A-3: Gamma approved after using different scanner for digitalization

Energy and day	Approved gamma (%) VerA	FilmQA Pro
6x day 1	54	62
6x day 2	45	51
6xFFF day 1	39	30
6xFFF day 2	54	57
10x day 1	40	50
10x day 2	42	45
10xFFF day 1	36	30
10xFFF day 2	39	36

Gamma passing rates appear to be similar to previous analyses but no consistency was found between identical films and how they performed in the two scanners. Figure A-11

shows comparisons between AAA and film for 10xFFF with the corresponding gamma map. The general characteristics in images from this scanner appear the same as images from the previous scanner. A more in depth characterization of this scanner was not done due to the low gamma passing rates.

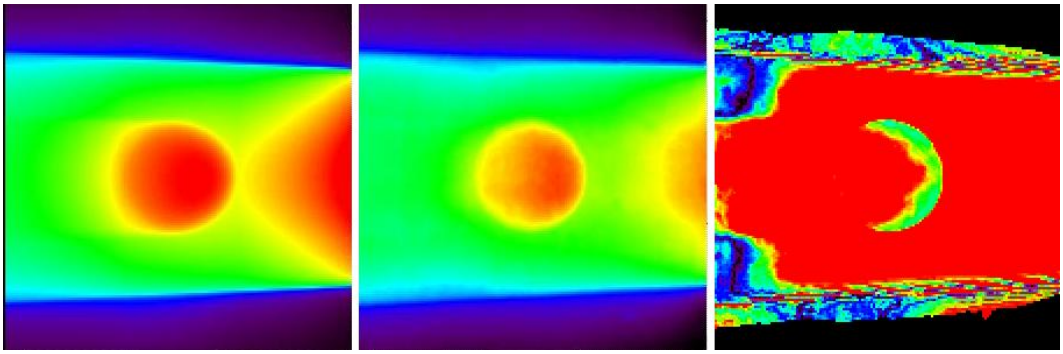

Figure A-11: AAA calculation, film response and gamma analysis for energy 10xFFF.